공학박사 학위논문

A study on surface oxide layer modification of alloys approached by selective oxidation

선택적 산화 열처리 기술을 바탕으로 접근한 합금의 표면 산화층 개질에 대한 연구

2023년 2월

서울대학교 대학원

재료공학부

박 재 영

A study on surface oxide layer modification of alloys approached by selective oxidation

지도교수 황농문

이 논문을 공학박사 학위논문으로 제출함

2023년 2월

서울대학교 대학원

재료공학부

박 재 영

박재영의 공학박사 학위논문을 인준함
2023년 2월

위 원 장	김 영 운	(Seal)
부위원장	황 농 문	(Seal)
위 원	한 흥 남	(Seal)
위 원	박 광 석	(Seal)
위 원	박 형 기	(Seal)

Abstract

A study on surface oxide layer modification of alloys approached by selective oxidation

Jae-Young Park
Department of Materials Science and Engineering
The Graduate School
Seoul National University

Fe-Si-Cr based alloy powder is an alloy system mainly used for soft magnetic composites (SMCs) cores. Since it can be manufactured in a complex shape and has the advantage of having isotropic magnetic properties, it is manufactured as an inductor core, an energy conversion device, through a powder metallurgy process. Considering the operating environment and energy storage of the core, it is essential to form a dense and uniform insulating layer between the powders. However, the method of forming the insulating layer in the conventional inductor core manufacturing process was mainly manufactured by applying a wet chemical process. Therefore, a non-uniform insulating layer is formed on the surface of the powder, and accordingly, a problem in that magnetic properties and insulating properties are continuously deteriorated is occurring. If only elements having excellent insulating properties are selectively oxidized in a vapor phase method rather than wet chemical process, it is possible to form a dense insulating layer having excellent insulating properties on the powder surface. This

heat treatment technique is referred to as a selective oxidation annealing.

Selective oxidation heat annealing is a heat treatment technology that makes it possible to oxidize only a specific element by controlling the oxidation potential during heat treatment by using the different oxidation driving forces of the elements constituting the alloy.

In this study, a selective oxidation annealing process was designed through thermodynamic calculations in redox reactions. And, by applying this to the Fe-Si-Cr soft magnetic powder alloy system and the Co-Cr-Mo alloy system, the oxide layer on the alloy surface was modified and the properties were improved.

First, heat treatment was performed on the Fe-Si-Cr powder in an atmosphere having various oxidation potentials, and it was confirmed that an oxide layer mainly of Si and Cr was selectively oxidized and formed on the powder surface under the condition of $p_{H_2(g)}/p_{H_2O(g)}$ =41.8. As a result of measuring the magnetic properties and insulating properties of the powder, it was confirmed that the magnetic properties were improved under condition $p_{H_2(g)}/p_{H_2O(g)}$=41.8 compared to the initial powder. As a result of analyzing the insulation property through the withstand voltage test, it was confirmed that the withstanding voltage value was more than twice as high as that of the initial powder.

When applying the selective oxidation annealing designed through thermodynamic calculation at the powder level, it was confirmed that the powder surface was selectively oxidized. Therefore, an additional experiment was conducted to confirm the oxide layer formation behavior by increasing the selective oxidation annealing time.

In addition, by applying the powder metallurgy process, soft magnetic powder discs and toroid cores were manufactured and magnetic and insulating properties were evaluated at the component level. The cores manufactured from the powders subjected to the selective oxidation annealing were compared and analyzed with the cores manufactured by applying the conventional wet chemical process through the withstand voltage test and the inductance measurement test. It was confirmed that the quality factor value, which comprehensively evaluates the quality of the core, was improved by about 16% in the core manufactured from the selectively oxidized powder compared to the inductor core manufactured by the wet chemical process.

And considering the operating environment of the actual inductor, a high-temperature load characteristic test in which a high-temperature load is applied for 1000 hrs and an additional electrochemical experiment were conducted to figure out the corrosion characteristics. Since a uniform and dense insulating layer was formed, it was confirmed that the quality factor did not decrease in the inductor core manufactured by applying the selective oxidation heat treatment even after the high-temperature load characteristics test.

As a result of the electrochemical experiment, it was confirmed that the insulating layer formed on the surface of the Fe-Si-Cr alloy had corrosion resistance through selective oxidation heat treatment. It was analyzed through XPS analysis and TEM that SiO_2 was formed inside the insulating layer and Cr_2O_3 insulating layer was formed outside, and the thickness of the insulating layer tended to increase as the selective oxidation annealing time increased. The insulating layer formed by the selective oxidation annealing caused

an improvement in the corrosion potential as a result of the polarization test, and it could be assumed that the corrosion characteristics were improved. In addition, through the EIS experiment in 3.5wt% NaCl solution, it was confirmed that the impedance semicircle tended to increase as the selective oxidation annealing time increased, and the insulation layer deterioration time was delayed. Through this, as the selective oxidation annealing time increased, the corrosion properties improved.

Even in the Co-Cr-Mo bio-alloy system, it is essential to improve the corrosion properties to prevent the elution of cobalt ions when inserted into the body. Under the condition of $p_{H_2(g)}/p_{H_2O(g)}$=41.8, during annealing, Co and Mo are not oxidized and only Cr elements with excellent corrosion properties are selectively oxidized. Through this, selective oxidation annealing was applied to the Co-Cr-Mo alloy system to evaluate the corrosion properties.

As such, the selective oxidation annealing technology is applicable to various alloy systems and is a next-generation insulation technology that is expected to be applicable to submicron-sized powders because it forms an insulation layer in a vapor phase method.

Keyword : Selective oxidation; Soft magnetic composites; Modification of insulation layer; Magnetic and insulation properties; Corrosion property

Student Number : 2018-27359

List of Figures

temperature in the thermostat bath. The $G^{o}_{H_2O(l)}$ and $G^{o}_{H_2O(g)}$ values were obtained from the Thermo-Calc software, and $p_{H_2O(g)}$ and $p_{H_2(g)}$ were calculated from the Eq. (12) and (13)

Figure 3.1. (a) A schematic of the annealing equipment, (b) the morphology of the initial Fe-Si-Cr powders.

Figure 3.2. The Ellingham diagram of the Fe, Si, and Cr oxides. The $P_{H_2(g)}/P_{H_2O(g)}$ ratio values according to the temperature is represented by a dotted line in the Ellingham diagram: selective oxidation annealing condition ($p_{H_2(g)}/p_{H_2O(g)}$ = 41.8), $p_{H_2(g)}/p_{H_2O(g)}$ = 2.5 condition and air oxidation condition are represented by red, blue and black diamond respectively.

Figure 3.3. (a) The XPS results of the initial powder and the annealed Fe-Si-Cr powders and (b) the chemical composition of the oxide layers calculated based on the XPS results.

Figure 3.4. An Ellingham diagram showing an enlarged region of the oxidation reaction equilibrium line of Fe element.

Figure 3.5. The Fe element peak region in XPS.

Figure 3.6. Oxygen concentration and withstanding voltage of samples

Figure 3.7. (a) The hysteresis loops of the initial and the annealed Fe-Si-Cr powders and (b) their magnified view ranging from 10k to 15 k Oe.

Figure 4.1. Schematic of the heat treatment furnace used in this study. H_2-H_2O mixed gas is supplied to the furnace by bubbling H_2

compound database of SSUB5. The $p_{H_2(g)}/p_{H_2O(g)}$ values according to temperature were represented by the dotted lines.

Figure 6.2. X-ray photoelectron spectroscopy (XPS) spectra of the as-built, SOA10, SOA20, and SOA30 samples.

Figure 6.3. Morphology of oxide layer on the (a) as-built, (b) SOA10, (c) SOA20, and (d) SOA30 samples analyzed by TEM.

Figure 6.4. Composition mapping results of the (a) as-built, (b) SOA10, (c) SOA20, and (d) SOA30 samples analyzed by TEM. The yellow rectangles indicate the region where the composition analysis of the oxide layer was performed.

Figure 6.5. (a) OCP variations with time and (b) polarization curves of the as-built, SOA10, SOA20, and SOA30 samples in 3.5 wt% sodium chloride (NaCl) solution.

Figure 6.6. Results of corrosion potential (E_{corr}) and corrosion current density (I_{corr}) were derived from the polarization curves of the as-built, SOA10, SOA20, and SOA30 samples

Figure 6.7. Nyquist plots of the as-built, SOA10, SOA20, and SOA30 samples were measured in 3.5 wt% sodium chloride (NaCl) solutions. The inlet is the equivalent circuit used to interpret the data.

Figure 6.8. Results of impedance parameters of the as-built, SOA10, SOA20, and SOA30 samples derived from the equivalent circuit analysis.

Table of Contents

Chapter 1. Introduction

1.1. SMCs(soft magnetic composites)

Soft magnetic composites (SMCs), which are composed of soft magnetic powders coated with electrically insulating materials, have high magnetic flux density, low core loss, and three dimensional isotropic magnetic properties [1-3]. Figure 1.1 shows the structure of SMC powder and has a structure in which an insulating layer is formed on the surface of the Fe-based powder. Because of these properties, SMCs are widely used in devices such as coils, motors, transformers, and inductors [4]. When SMC powder is used to manufacture a core by applying a powder metallurgy process, it is possible to have the advantage of being able to manufacture a complex shape without alloy composition limitations.

Among many soft magnetic powders, Fe-Si-Cr powders are used for inductors needed in high power, high frequency, and small-scale applications because of their high insulation impedance, high resistance to saturation, and low core loss at high frequencies [5, 6]. In SMCs, the insulation coating as well as the chemical composition of the powders is important to achieve low energy loss. If the insulating property between the powders is low, the electric resistivity is lowered, thus increasing the eddy current loss [7]. Many studies have been conducted on insulation coating technologies for SMCs to address the issue of energy loss in high-frequency regions largely caused by the eddy current loss [8].

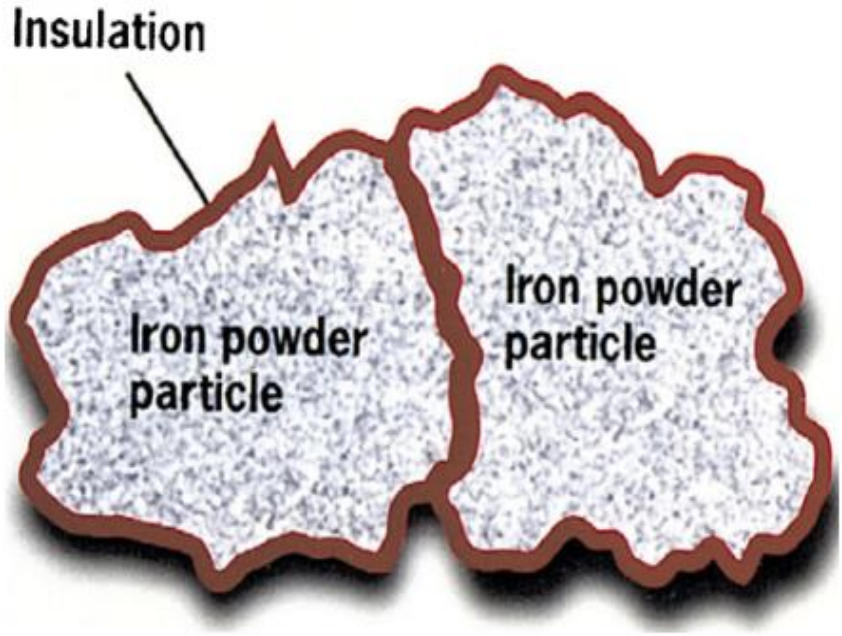

Figure 1.1. Soft magnetic composites (SMCs), which are composed of soft magnetic powders coated with electrically insulating materials [1].

1.2. Energy loss mechanism of SMC core under alternating magnetic field

There are many compositions of the powders used for SMCs. An Fe-Si alloy is the base alloy system because Si addition on Fe is effectively increasing the resistivity [9]. Among various Fe-based soft magnetic powders, the Fe-Si-Cr system has high insulating impedance and specific resistivity as well as an excellent stability at high temperatures [10]. In addition, since the Fe-Si-Cr alloy has a low core loss in the high frequency region, it is widely used in high-power inductors [11].

As shown in Figure 1.2, a magnetic loss in the SMC is composed of hysteresis, eddy current and anomalous losses [12]. Recently, the frequency of applications such as inductors has gradually increased due to the miniaturization and high performance of the SMC components [13]. In the high frequency region, the eddy current loss occupies the highest proportion in the entire magnetic loss [14]. To increase the energy efficiency of the inductor, therefore, it is important to reduce the eddy current loss. The eddy current loss of the SMC decreases with increasing the resistivity and decreasing the effective powder size [15, 16]. Thus, to reduce the eddy current loss, the effective powder size should be lowered by forming an insulation layer on the powder surface [17, 18].

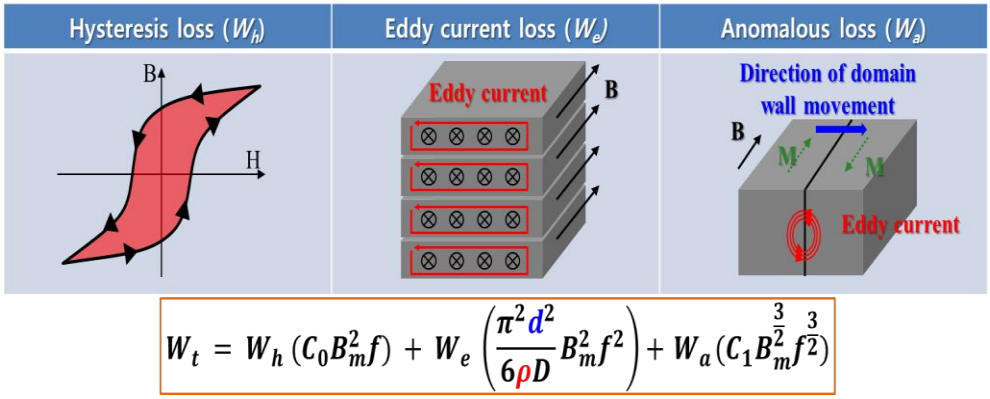

Figure 1.2. Energy loss mechanism of SMC core: hysteresis loss, eddy current loss, anomalous loss

1.3. Powder coating method to reduce eddy current loss

Insulation coating can be divided into two types: organic coating and inorganic coating [19]. It can be classified as in Figure 1.3. Organic insulation coating has good insulating properties, formability, and green body strength [20]. Molding SMC inductor is fabricated by uniaxial compacting of SMC powders, and the magnetic properties are degraded by the residual stress generated by the compaction. Therefore, removing residual stress through stress relief annealing is a necessary step, but the low thermal stability of organic insulation coatings limits the annealing temperature [21]. For the second type, given how inorganic coatings mainly use oxides for the insulating materials, not only do they have excellent insulating properties, they also have high thermal stability [22]. However, most inorganic coatings use a sol–gel process, known for its complexity and uneven coating layer formation [23].

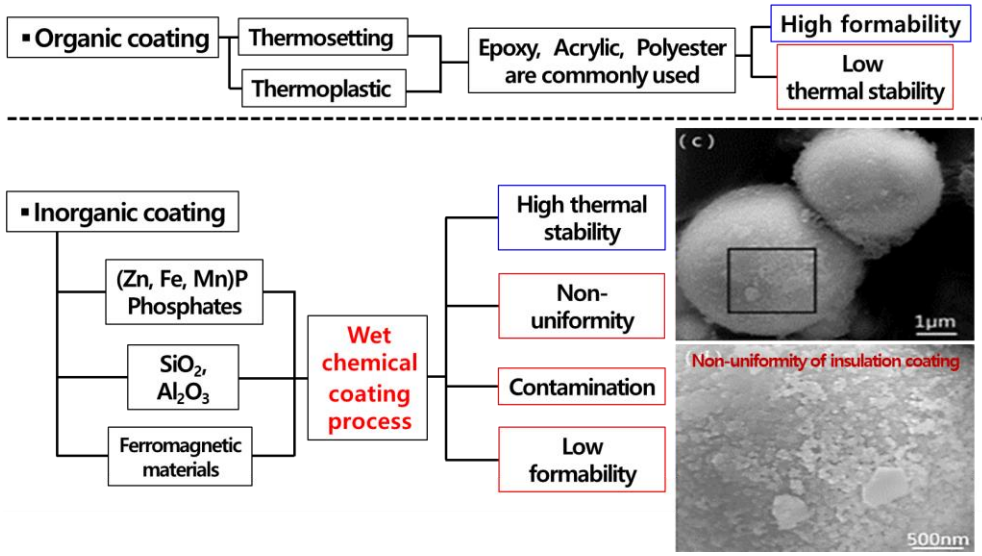

Figure 1.3. Insulation layer formation method on SMC powder surface: organic and inorganic coating method

In actual industrial lines, an insulating layer is formed on the surface by granulating the powder using a wet chemical process using phosphate and SiO_2 insulating material. However, when wet process is applied, the problem of the non-uniform insulating layer on the surface of the powder constantly occurs. As shown in Figure 1.4, insulation defects of about 3.4% occur in actual industrial sites.

[EA]	TIC Ref.
Inspection samples	59
Defective samples	2
Defective rate	**3.4%**

Figure 1.4. Insulation coating defect rate caused by the application of wet chemical process in the industrial field

Chapter 2. Thermodynamics of selective oxidation annealing

2.1. Selective oxidation heat treatment

The selective oxidation heat treatment is a method that selectively oxidizes certain elements by controlling the oxidation potential [24-26]. When the oxidation driving force of the elements constituting the alloy is different, it is possible to form a dense oxide layer on the surface by selectively oxidizing specific elements [27-29]. This annealing process is advantageous because it regulates the formation of an oxide layer by only modulating the oxidation potential during the annealing process. Selective oxidation heat treatment technology is a generally used heat treatment that can be applied to any alloy system made of elements with different oxidation driving forces because selective oxidation heat treatment uses the difference in the oxidation driving force of the elements constituting the alloy.

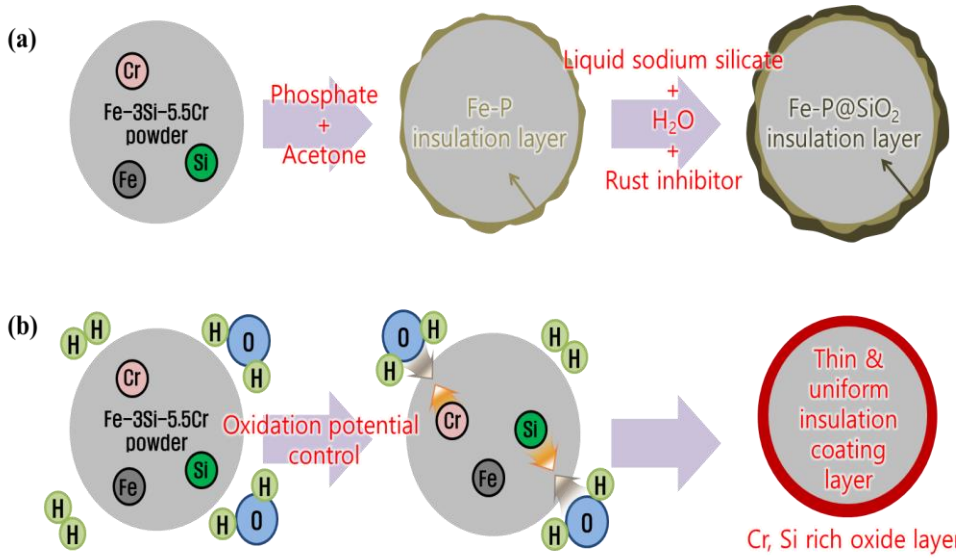

Figure 2.1.(a) Insulation coating for Fe-Si-Cr powder surface by wet chemical coating process and (b) evolution of insulation layer in Fe-Si-Cr powder by selective oxidation heat treatment

Figure 2.1(a) is a schematic showing the commonly used process of forming an insulating layer on the powder surface through a wet chemical process in the FeSiCr system, which is a representative soft magnetic alloy composition system mainly used for inductor cores. In the conventional wet process, an insulating material such as phosphate and liquid sodium silicate is mixed with a solvent and the powder is immersed and granulated to form an insulating layer on the surface of the powder. However, when an insulating layer is formed on the surface of the powder through this wet chemical process, not only an non-uniform insulating layer is formed, but also a drying process and a sieving process are added for each insulation processes. Therefore, the wet chemical insulation coating process as in Figure 2.1(a) is a very inefficient process.

In the case of Figure 2.1(b), it is a schematic diagram of a selective oxidation heat treatment process that selectively oxidizes only Si and Cr with excellent insulating properties by appropriately controlling the heat treatment atmosphere through thermodynamic calculations for each element of Fe, Si, and Cr. Since the oxidation potential of each element of Fe, Si, and Cr is different, it is possible to oxidize only a specific element. Fe element is in charge of magnetic properties in Fe-Si-Cr soft magnetic alloy system, and when selective oxidation heat treatment is applied, it is possible to form a uniform insulating layer on the surface without deteriorating the magnetic properties of the powder. And since the insulating layer is formed in a gas phase method, a uniform and dense insulating layer can be formed on the surface of the powder.

Since the selective oxidation heat treatment technology uses the difference in the oxidation driving force of the elements constituting the alloy, it can be applied to various alloy systems. For example, it is considered that it can be universally applied to surface modification of CoCrMo alloy, which is a representative composition of biomaterials, CoCrTiMo superalloy system and TiFe alloy, which is a representative composition of hydrogen storage alloys.

2.2. Thermodynamic calculations in metal oxidation reaction

The oxidation reaction of metal can be expressed by the following reaction equation.

$$M_{(s)} + O_{2(g)} \rightarrow MO_{2_{(s)}} \quad (1)$$

The Gibbs free energy change for the oxidation reaction of metal can be expressed as Eq. (2).

$$\Delta G = G_{MO_{2(s)}} - G_{M_{(s)}} - G_{O_{2(g)}} \quad (2)$$

The Gibbs free energy of the gas phase is given by:

$$G = G^0 + RTlnp \quad (3)$$

By substituting, Eq. (3) into Eq. (2), it is rearranged as follow:

$$\Delta G = \Delta G^0 - RTlnp_{O_{2(g)}} \quad (4)$$

ΔG^0 is the standard Gibbs free energy change ($\Delta G^0 = G^0_{MO_{2(s)}} - G^0_{M_{(s)}} - G^0_{O_{2(g)}}$). The G^0 values were obtained from Thermo-calc software. When the oxidation and reduction is in the equilibrium state, the ΔG value is 0. At this time, once ΔG^0 and temperature are determined, the equilibrium oxygen partial pressure ($(p_{O_{2(g)}})_{eq}$) for oxidation and reduction can be calculated by Eq. (4).

2.2.1 Ellingham diagram of Fe–Si–Cr alloy system shown as oxygen partial pressure $(p_{O_2(g)})$

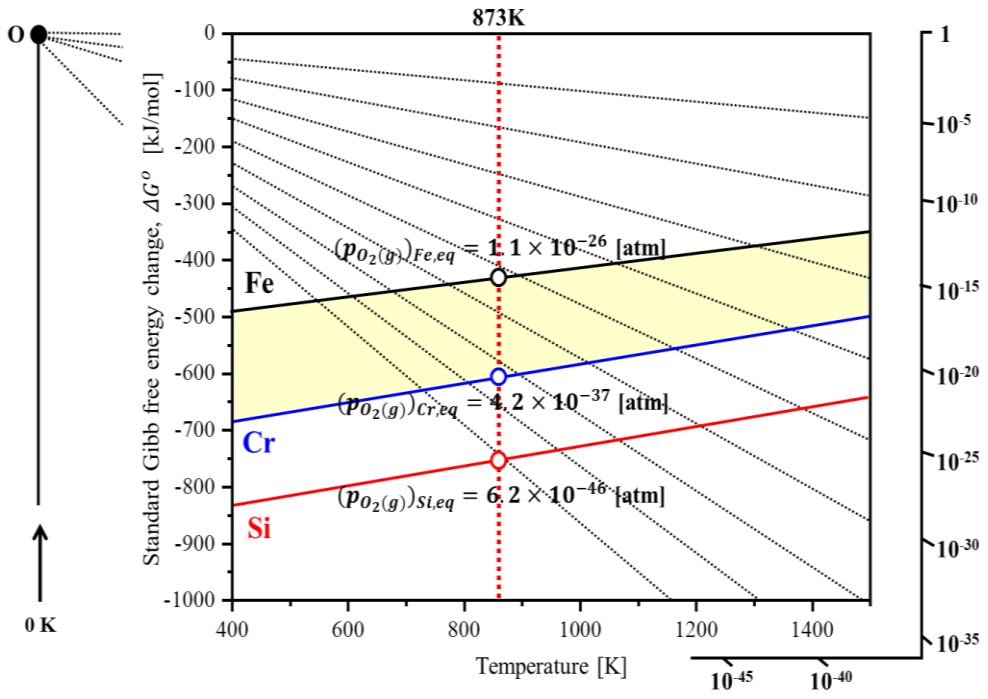

Figure 2.2. The Ellingham diagram of the Fe, Si, and Cr elements. The $p_{O_2(g)}$ values according to the temperature are represented by a dotted line in the Ellingham diagram.

Figure 2.2 shows the Ellingham diagram of the Fe, Si, and Cr oxides, which represents the oxidation driving force of each element. Given how the oxidation driving force of each element is different, it is possible to oxidize specific elements by controlling the oxidation potential. Among the three elements, the absolute value of the oxidation driving force for Fe was the smallest. When the equilibrium oxygen partial pressures $(p_{O_2(g)})_{eq}$ were calculated based on the Eq. (4), the $(p_{O_2(g)})_{eq}$ values of Fe, Cr, and Si at 600 ℃ are 1.1×10^{-26}, 4.2×10^{-37}, and 6.2×10^{-46} atm, respectively. Therefore, in the condition where the oxygen partial pressure ($p_{O_2(g)}$) value is higher than 1.1×10^{-26} atm at 600 ℃, all three elements are oxidized. On the other hand, in the condition where the $p_{O_2(g)}$ value is lower than 1.1×10^{-26} atm and higher than 14.2×10^{-37} atm, Fe is reduced and only Cr and Si are selectively oxidized to form a Cr and Si complex oxide layer on the powder surface.

And this selective oxidation heat treatment process window is indicated by the yellow area in Figure 2.2. Through this $p_{O_2(g)}$ control, the oxidation and reduction behavior of each element and the composition of the oxide layer can be controlled. However, the $p_{O_2(g)}$ values mentioned above are very low and difficult to control. Therefore, the oxidation potential was controlled by the partial pressure ratio of hydrogen and water vapor ($p_{H_2(g)}/p_{H_2O(g)}$), which is much easier to control. The $p_{O_2(g)}$ can be converted into the $p_{H_2(g)}/p_{H_2O(g)}$ ratio by the following equation

2.3. Thermodynamic calculations in hydrogen oxidation reaction

Therefore, we convert the $p_{O_2(g)}$ value to the $p_{H_2(g)}/p_{H_2O(g)}$ ratio to control the selective oxidation atmosphere using hydrogen oxidation reaction:

$$2H_{2(g)} + O_{2(g)} \rightarrow 2H_2O_{(g)} \quad (5)$$

From the Eq. (5), the Gibbs free energy change for the oxidation reaction of hydrogen can be expressed as Eq. (6).

$$\Delta G = 2G_{H_2O(g)} - 2G_{H_2(g)} - G_{O_2(g)} \quad (6)$$

By substituting Eq. (3) into the Eq. (6), it is rearranged as follow:

$$\Delta G = \Delta G^{o}_{H_2,\,oxidation} + 2RT ln p_{H_2O(g)} - 2RT ln p_{H_2(g)} - RT ln p_{O_2(g)} \quad (7)$$

where $\Delta G^{o}_{H_2,\,oxidation}$ is the standard Gibbs free energy change for hydrogen oxidation ($\Delta G^{o}_{H_2,\,oxidation} = 2G^{o}_{H_2O(g)} - 2G^{o}_{H_2(g)} - G^{o}_{O_2(g)}$).

When the oxidation reaction of hydrogen is in the equilibrium state, ΔG becomes 0, and the relationship between the $p_{O_2(g)}$ and $p_{H_2(g)}/p_{H_2O(g)}$ can be represented as Eq. (8).

$$RT ln p_{O_2(g)} = \Delta G^{o}_{H_2,\,oxidation} - 2RT\, ln\left(\frac{p_{H_2(g)}}{p_{H_2O(g)}}\right) \quad (8)$$

By mathematical rearrangement, Eq. (8) can be rearranged as follow.

$$\frac{p_{H_2(g)}}{p_{H_2O(g)}} = exp\left\{\frac{\Delta G^{o}_{H_2,\,oxidation} - RT ln(p_{O_2(g)})}{2RT}\right\} \quad (9)$$

The $p_{H_2(g)}/p_{H_2O(g)}$ value in the equilibrium state for the oxidation and reduction ($(p_{H_2(g)}/p_{H_2O(g)})_{eq}$) can be obtained by substituting the $(p_{O_2(g)})_{eq}$ value in Eq. (9). When the $p_{H_2(g)}/p_{H_2O(g)}$ ratio is lower than the $(p_{H_2(g)}/p_{H_2O(g)})_{eq}$ value, the oxidation occurs, and conversely, when the $p_{H_2(g)}/p_{H_2O(g)}$ ratio is higher than the $(p_{H_2(g)}/p_{H_2O(g)})_{eq}$ value, the reduction occurs.

2.3.1 Ellingham diagram of Fe–Si–Cr alloy system shown as hydrogen and water vapor mixed gas partial pressure ($p_{H_2(g)}/p_{H_2O(g)}$)

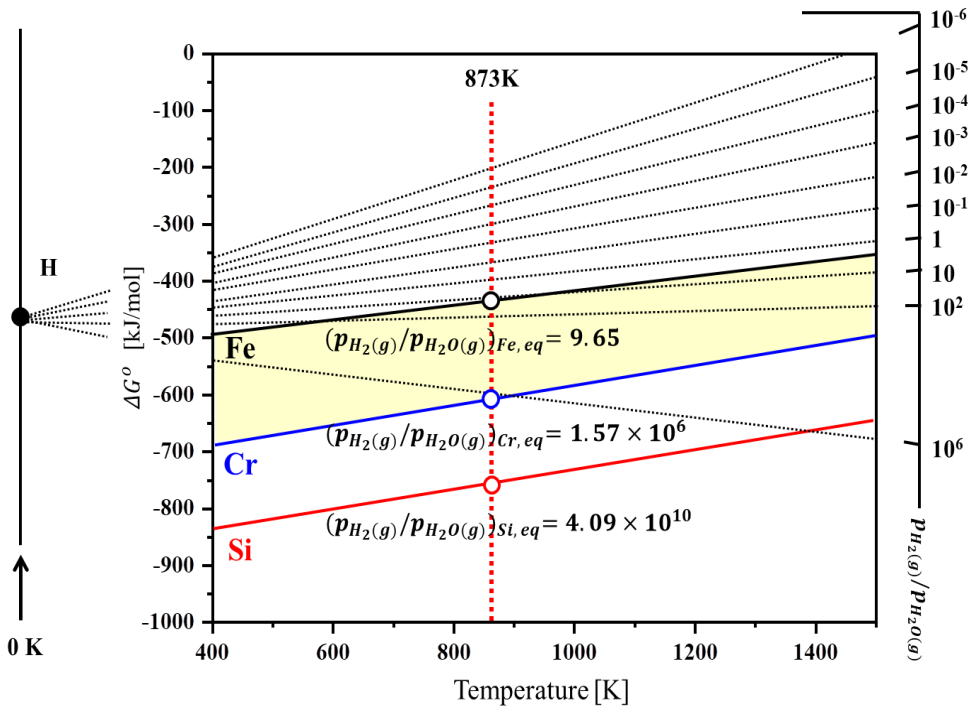

Figure 2.3. The Ellingham diagram of the Fe, Si, and Cr elements. The $p_{H_2(g)}/p_{H_2O(g)}$ values according to the temperature are represented by a dotted line in the Ellingham diagram.

Figure 2.3 shows The Ellingham diagram of the Fe, Si, and Cr elements. The $p_{H_2(g)}/p_{H_2O(g)}$ values according to the temperature are represented by a dotted line in the Ellingham diagram. As the $p_{H_2(g)}/p_{H_2O(g)}$ ratio increases, the condition changes into the reduction atmosphere. When calculating the equilibrium $p_{H_2(g)}/p_{H_2O(g)}$ ratio for the oxidation of three elements at 600 ℃ by Eq. (9), the value of Fe, Cr, and Si are 9.65, 1.57×10^{6}, and 4.09×10^{10}, respectively. Therefore, when the $p_{H_2(g)}/p_{H_2O(g)}$ ratio is lower than 9.65, all three elements are oxidized, and when it is higher than 9.65 and lower than 1.57×10^{6}, only Cr and Si are selectively oxidized. And this selective oxidation heat treatment process window is indicated by the yellow area in Figure 2.3.

2.4 Thermodynamic calculations in a thermostat water bath

The $p_{H_2(g)}/p_{H_2O(g)}$ mentioned above can be calculated and realized through the thermostat water bath equipment. Figure 2.4 shows the thermostat water bath equipment. Distilled water (D.I water) is contained in the thermostat water bath, and the D.I water in the thermostat bath is in equilibrium state between liquid water and gaseous water vapor gas according to the temperature of the thermostat water bath equipment.

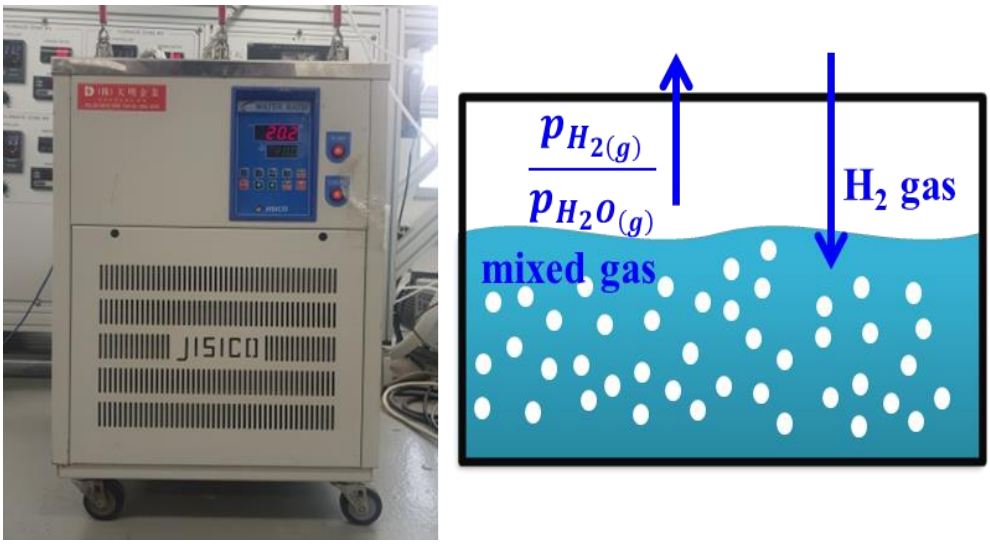

Figure 2.4. Thermostat water bath equipment and Schematic of formation of $p_{H_2(g)}/p_{H_2O(g)}$ through thermostat water bath

The H_2-H_2O mixed gas was supplied to the heat treatment furnace by bubbling H_2 gas into the water as shown in Figure 2.4. At this time, the $p_{H_2(g)}/p_{H_2O(g)}$ ratio can be controlled through the water temperature of the thermostat bath. In the thermostat water bath, liquid water and gaseous water are in the equilibrium state.

$$\Delta G = G_{H_2O(g)} - G_{H_2O(l)} \quad (10)$$

In the equilibrium state, the ΔG in Eq. (10) becomes 0, and by substituting Eq. (3), the equation is expressed as Eq. (11).

$$0 = G^{\circ}_{H_2O(g)} + RT\ln p_{H_2O} - G^{\circ}_{H_2O(l)} \quad (11)$$

By mathematical rearrangement of Eq. (11), the $p_{H_2O(g)}$ value according to the temperature can be obtained from Eq. (12).

$$p_{H_2O(g)} = \exp\left\{-\frac{G^{\circ}_{H_2O(g)} - G^{\circ}_{H_2O(l)}}{RT}\right\} \quad (12)$$

Since the experiment was performed at 1 atm, the $p_{H_2(g)}$ can be calculated by Eq. (13).

$$p_{H_2(g)} = 1 - p_{H_2O(g)} \quad (13)$$

When 100% H_2 gas was injected to the thermostat water bath, the $p_{H_2(g)}/p_{H_2O(g)}$ ratio according to the thermostat temperature was calculated using equations (12) and (13), and the results are summarized in Figure 2.5.

Thermostat water bath temperature [℃]	$G^0_{H_2O_{(l)}}$ [kJ/mol]	$G^0_{H_2O_{(g)}}$ [kJ/mol]	p_{H_2O} [atm]	p_{H_2} ($1-p_{H_2O}$) [atm]	$p_{H_2(g)}/p_{H_2O(g)}$			
					H_2 100%	H_2 50% (N_2 50%)	H_2 20% (N_2 80%)	H_2 10% (N_2 90%)
10	-305.7	-295.3	0.012	0.988	**80.4**	**40.2**	**16.0**	**8.0**
20	-306.3	-297.2	0.023	0.977	**41.8**	**20.9**	**8.3**	**4.2**
30	-307.0	-299.1	0.042	0.938	**22.6**	**11.3**	**4.5**	**2.3**
40	-307.8	-301.0	0.074	0.926	**12.6**	**6.29**	**2.5**	**1.2**

Figure 2.5. The $p_{H_2(g)}/p_{H_2O(g)}$ ratio according to the water temperature in the thermostat bath. The $G^o_{H_2O(l)}$ and $G^o_{H_2O(g)}$ values were obtained from the Thermo-Calc software, and $p_{H_2O(g)}$ and $p_{H_2(g)}$ were calculated from the Eq. (12) and (13)

When the temperature of the thermostat water bath is set at 20 ℃ and 100% hydrogen gas is blown into the thermostat, $\frac{p_{H_2(g)}}{p_{H_2O(g)}}$=41.8 condition can be formed. When the temperature of the thermostat is set at 40 ℃, 20% of hydrogen gas and 80% of the nitrogen gas that does not participate in the reaction are mixed, and then injected into the thermostat water bath; It is possible to form an atmosphere of condition $\frac{p_{H_2(g)}}{p_{H_2O(g)}}$=2.5 inside the heat treatment furnace.

As mentioned earlier, the $(p_{H_2(g)}/p_{H_2O(g)})_{eq}$ value of Fe at 600 ℃ is 9.65. From Eq. (12), the temperature of the thermostat is 44.3 ℃ to control the $p_{H_2(g)}/p_{H_2O(g)}$ ratio to 9.65. Therefore, to form an atmosphere for the selective oxidation of Cr and Si, it is only necessary to bubble 100% H_2 gas into water with the temperature of 44.3 ℃ or less. If the selective oxidation atmosphere is formed by controlling the $p_{O_2(g)}$, the $p_{O_2(g)}$ value must be set to 1.10×10^{-26} atm or less. However, when the oxidation potential is controlled by the $p_{H_2(g)}/p_{H_2O(g)}$, the selective oxidation atmosphere can be formed more easily under realistic conditions.

Chapter 3. Formation of Fe-Si-Cr powder surface insulating layer through selective oxidation heat treatment

3.1. Surface modification under various annealing conditions

In this part, For the Fe-3Si-5.5wt%Cr powder alloy system, a selective oxidation annealing process was designed to oxidize only Si and Cr elements through thermodynamic calculations based on Chapter 2. An additional experiment conditions were conducted to find out how the oxide layer was controlled on the powder surface by forming an atmosphere with various oxidation potentials as well as a selective oxidation annealing atmosphere.

3.2. Experimental procedure

Water-atomized Fe-Si-Cr soft magnetic powders, with a composition of Fe-3Si-5.5Cr (in wt%), were used as an initial material. Selective oxidation annealing was performed to form an insulating oxide layer on the powder surface. For annealing, a tube furnace equipped with load lock chamber and thermostat water bath were used as shown in Figure 3.1(a). The annealing of the powders was carried out by putting it in a load lock chamber, evacuating a vacuum, and inserting powders into the furnace using a delivery path. The morphology of the initial water-atomized Fe-Si-Cr powders is shown in Figure 3.1(b). The powders had an irregular shape and their d_{50} value was 10.3 μm. When measuring the oxygen concentration, the initial powder had an oxygen concentration of 0.188 wt%.

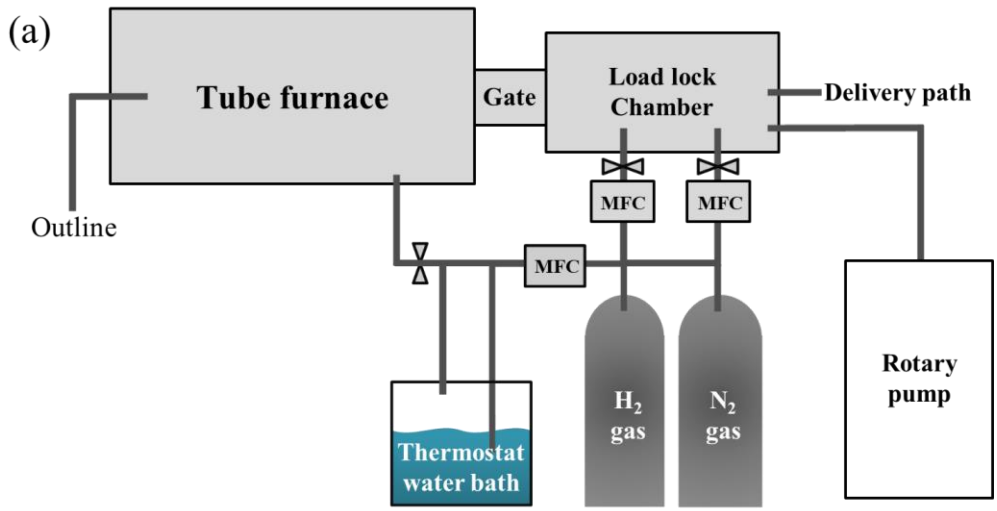

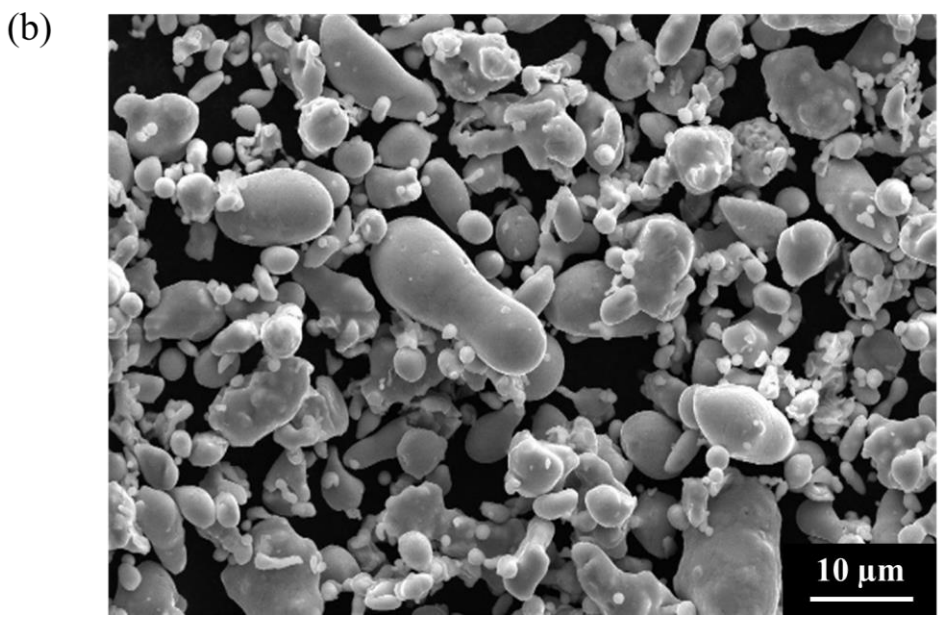

Figure 3.1. (a) A schematic of the annealing equipment, (b) the morphology of the initial Fe-Si-Cr powders.

For the selective oxidation annealing of the Fe−Si−Cr powder, the oxidation potential was controlled by the $p_{H_2(g)}/p_{H_2O(g)}$ ratio. The hydrogen gas was bubbled into the thermostat water bath and then injected into the furnace. The partial pressure of H_2O ($p_{H_2O(g)}$) was calculated through the dew point according to the water temperature in the thermostat bath. The partial pressure of H_2 ($p_{H_2(g)}$) was controlled as the ratio of H_2 gas and N_2 gas, which is not participating in the reaction and the total gas flow rate was 500 sccm.

From the viewpoint of the oxidation thermodynamics of metals, as the reaction temperature increases, it is easier to control the oxidation and reduction reactions through an atmosphere control. However, the higher the reaction temperature, the faster the oxidation reaction kinetics, making it difficult to control the thickness of the oxide layer. According to the previous study on the oxidation of the Fe−13.08Si−4.52Cr powders, the oxidation rapidly progressed during the annealing above 700 ℃ [30]. Therefore, in this study, the annealing temperature was set to 600 ℃ (873K). Powders were injected inside the furnace using alumina crucible to simulate the continuous annealing. Annealing was performed for 30 min, and after that the powders were loaded out of the furnace and cooled in a nitrogen atmosphere.

The oxidation driving force of Fe, Si, and Cr was calculated by Thermo-Calc using SSOL database and the selective oxidation conditions were set based on the calculation result. Annealing was performed under conditions in which 100%H_2 was bubbled in a thermostat at 20 ℃ ($p_{H_2(g)}/p_{H_2O(g)}$ = 41.8) and a mixed gas of 20%H_2-80%N_2 was bubbled in a thermostat at 40 ℃ ($p_{H_2(g)}/p_{H_2O(g)}$ = 2.5). The oxidation behavior under each condition is explained in the 3.3, 3.4 section. In addition, the initial powder was annealed for 30 min in an air atmosphere.

3.2.1. Experimental procedure: selective oxidation annealing process design by thermodynamic calculations

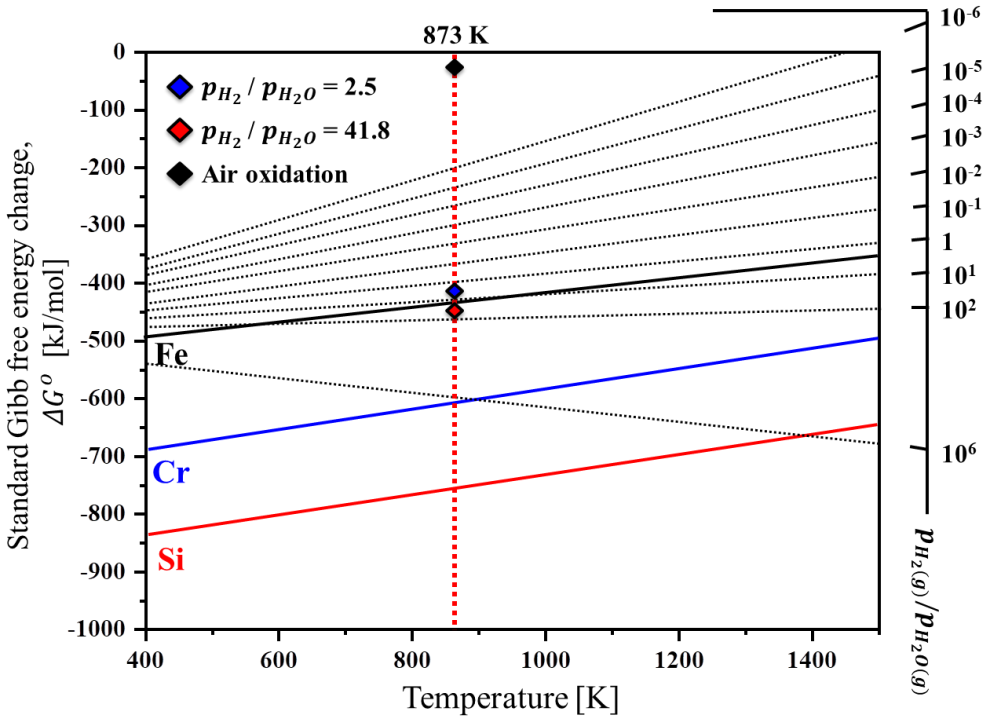

Dew	p_{H_2} / p_{H_2O}		
°C	**100% H_2**	**50% H_2**	**20% H_2**
10	80.4	40.2	16.1
20	◆ **41.8**	20.9	8.4
30	22.6	11.3	4.5
40	12.6	6.29	◆ **2.5**

Figure 3.2. The Ellingham diagram of the Fe, Si, and Cr oxides. The $P_{H_2(g)}/P_{H_2O(g)}$ ratio values according to the temperature is represented by a dotted line in the Ellingham diagram: selective oxidation annealing condition ($p_{H_2(g)}/p_{H_2O(g)}$ = 41.8), $p_{H_2(g)}/p_{H_2O(g)}$ = 2.5 condition and air oxidation condition are represented by red, blue and black diamond respectively.

Figure 3.2 shows the Ellingham diagram of the Fe, Si, and Cr oxides, which represents the oxidation driving force of each element. Given how the oxidation driving force of each element is different, it is possible to oxidize specific elements by controlling the oxidation potential. Among the three elements, the absolute value of the oxidation driving force for Fe was the smallest. When the equilibrium oxygen partial pressures ($p_{O_2(eq)}$) were calculated based on the Eq. (4) in the section 2.2, the $p_{O_2(eq)}$ values of Fe, Cr, and Si at 600 ℃ are 1.1×10^{-26}, 4.2×10^{-37}, and 6.2×10^{-46} atm, respectively. Therefore, in the condition where the oxygen partial pressure ($p_{O_2(g)}$) value is higher than 1.1×10^{-26} atm at 600 ℃, all three elements are oxidized. On the other hand, in the condition where the $p_{O_2(g)}$ value is lower than 1.1×10^{-26} atm and higher than 4.2×10^{-37} atm, Fe is reduced and only Cr and Si are selectively oxidized to form a Cr and Si complex oxide layer on the powder surface. Through this $p_{O_2(g)}$ control, the oxidation and reduction behavior of each element and the composition of the oxide layer can be controlled. However, the $p_{O_2(g)}$values mentioned above are very low and difficult to control.

As the $p_{H_2(g)}/p_{H_2O(g)}$ ratio increases, the condition changes into the reduction atmosphere. When calculating the equilibrium $p_{H_2(g)}/p_{H_2O(g)}$ ratio for the oxidation of three elements at 600 ℃ based on the Eq. (9) in the section 2.3, the value of Fe, Cr, and Si are 9.65, 1.6×10^{6}, and 4.1×10^{10}, respectively. Therefore, when the $p_{H_2(g)}/p_{H_2O(g)}$ ratio is lower than 9.65, all three elements are oxidized, and when it is higher than 9.65 and lower than 1.6×10^{6}, only Cr and Si are selectively oxidized. Based on these calculations, the initial powders were annealed in the atmosphere of the $p_{H_2(g)}/p_{H_2O(g)}$ ratio of 2.5 (20%H_2−80%H_2, dew point 40 ℃) in which all three elements are oxidized. Moreover, they were annealed in the atmosphere of the $p_{H_2(g)}/p_{H_2O(g)}$ ratio of 41.8 (100% H_2, dew point 20 ℃), which is the condition for selective oxidation of Cr and Si except Fe.

3.2.2 Experimental procedure: powder analysis

The morphology of the initial powder was observed by using a field emission-scanning electron microscope (FE-SEM; FEI, QUANTA FEG 250). The oxygen concentrations of the initial powder and the annealed powders were analyzed using a NOH analyzer (Leco, 836 series). The withstanding voltages of the samples were measured using a withstanding voltage tester (TOS5101, KIKUSUI). The magnetic properties of the samples were examined with a vibrating sample magnetometer (VSM; Model 7404, Lake Shore Cryotronics).

3.3. XPS analysis: $p_{H_2(g)}/p_{H_2O(g)}$ =41.8, $p_{H_2(g)}/p_{H_2O(g)}$=2.5 and air oxidation conditions

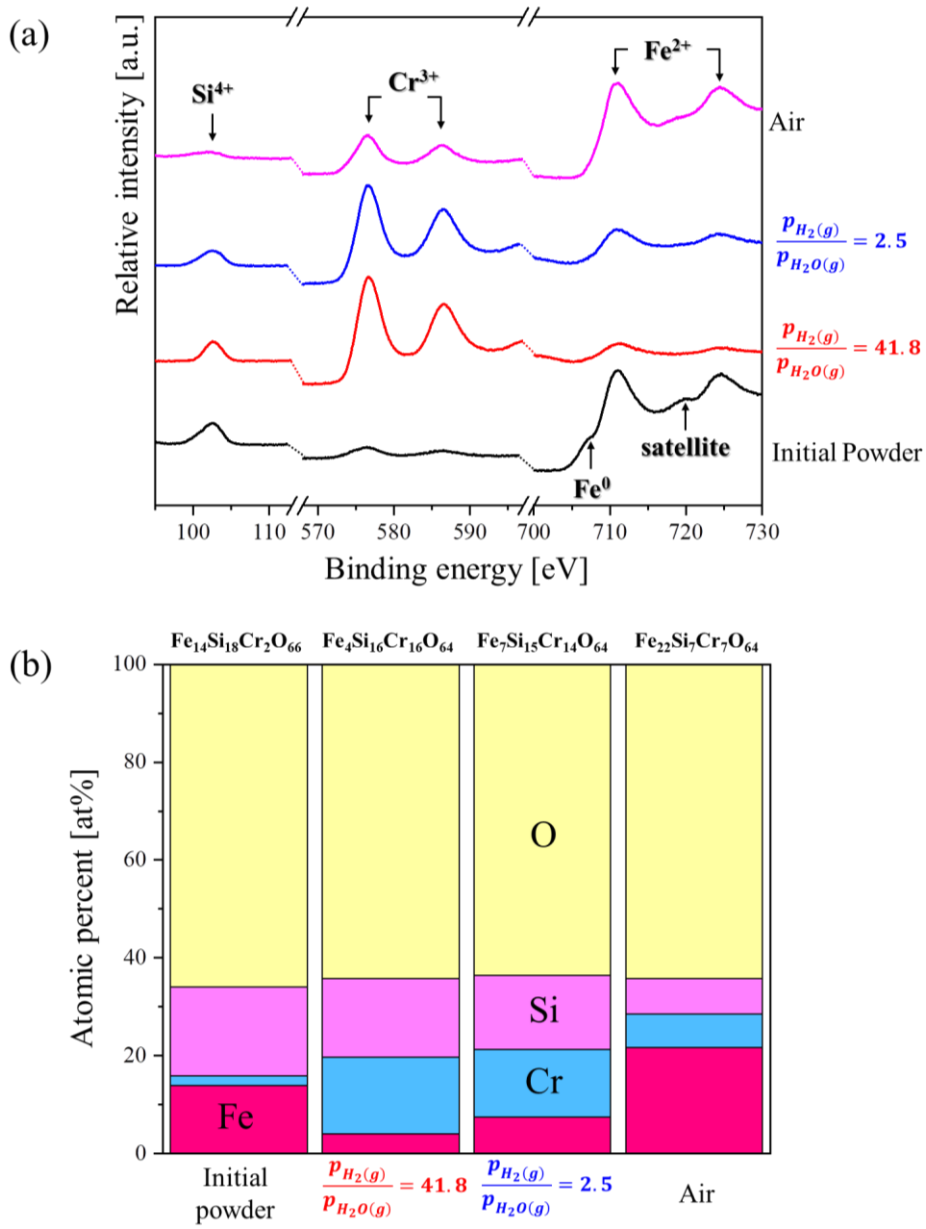

Figure 3.3.(a) The XPS results of the initial powder and the annealed Fe-Si-Cr powders and (b) the chemical composition of the oxide layers calculated based on the XPS results.

The samples were analyzed via XPS to examine the changes in the powders' oxide layer according to the annealing conditions, with results shown in Figure 3.3(a). Figure 3.3(b) represents the chemical composition of the oxide layers, which are calculated based on the XPS results. All samples had similar oxygen concentrations from 63.6 to 66.0 at%. In the initial powder's oxide layer, the concentration of Fe and Si was high at 13.8 and 18.1 at%, respectively, whereas the Cr concentration was very low at 1.9 at%.

While examining the XPS result of the powder applying the selective oxidation annealing ($p_{H_2(g)}/p_{H_2O(g)}$ = 41.8), the intensity of the Cr peaks had drastically increased while the intensity of the Fe peaks decreased sharply. Si concentration was similar to the initial powder at 16.1 at%, but the Fe concentration decreased to 4.0 at% and the Cr concentration increased to 15.7 at%. Since selective oxidation annealing is the condition in which Fe is reduced and Cr and Si are selectively oxidized, the Fe concentration in the oxide layer decreased, while a Cr and Si complex oxide layer formed as the Cr and Si oxidized together.

In the oxide layer of the powder annealed in the air atmosphere, the Fe concentration significantly increased to 21.6 at%, and the Si and Cr concentrations relatively decreased compared to the selective oxidation conditions. The condition in the $p_{H_2(g)}/p_{H_2O(g)}$ ratio of 2.5 is an atmosphere in which all three elements are oxidized as in the air annealing condition. However, given that the oxidation potential of the condition ($p_{H_2(g)}/p_{H_2O(g)}$ = 2.5) is lower than that of the air annealing condition, the intensities of Fe peaks did not significantly increase as oxidation proceeded slowly.

A detailed analysis was performed by combining the XPS results with the Ellingham diagram. Figure 3.4. was an Ellingham diagram showing an enlarged region of the oxidation reaction equilibrium line of Fe element. The oxidation reaction equilibrium line of the Fe element could be divided into the oxidation reaction equilibrium line in which Fe^{2+} and Fe^{3+} ions were oxidized. And this was indicated by black and orange lines, respectively. First, selective oxidation annealing condition ($p_{H_2(g)}/p_{H_2O(g)}$ = 41.8), it could be confirmed in the figure 3.4 that the red circle was located below both the orange and black line. Therefore, both Fe^{3+} and Fe^{2+} ions were reduced.

Figure 3.5 shows only the Fe element peak region in XPS. In the case of the selective oxidation heat treatment condition ($p_{H_2(g)}/p_{H_2O(g)}$ = 41.8), both Fe^{3+} and Fe^{2+} elements were reduced, so as can be seen from XPS analysis, Fe^{3+} peak (719.0 eV) and Fe^{2+} peak (711.0, 727.0 eV) were not observed. However, in the case of the $p_{H_2(g)}/p_{H_2O(g)}$ = 2.5, as can be seen in the figure 3.4, it could be confirmed that the blue circle was located below the orange line but above the black line. Therefore, under $p_{H_2(g)}/p_{H_2O(g)}$ = 2.5 condition, Fe^{3+} was reduced, but only Fe^{2+} ion was oxidized. Therefore, when analyzing the $p_{H_2(g)}/p_{H_2O(g)}$ = 2.5 condition in the figure 3.5, it could be confirmed that Fe^{3+} ion peak was not detected while Fe^{2+} ion peak remained. In the case of atmospheric oxidation, it was indicated by a black circle in the figure 3.4. This was a condition in which both Fe^{2+} and Fe^{3+} ions are oxidized, so both Fe^{2+} and Fe^{3+} peaks were measured in XPS analysis.

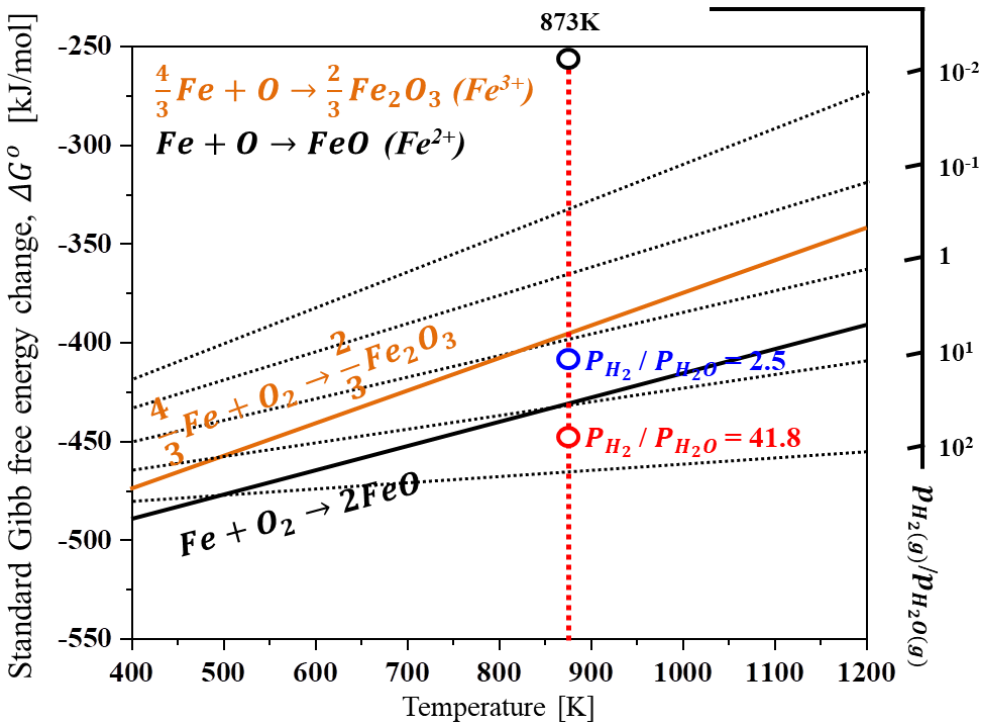

Figure 3.4. An Ellingham diagram showing an enlarged region of the oxidation reaction equilibrium line of Fe element.

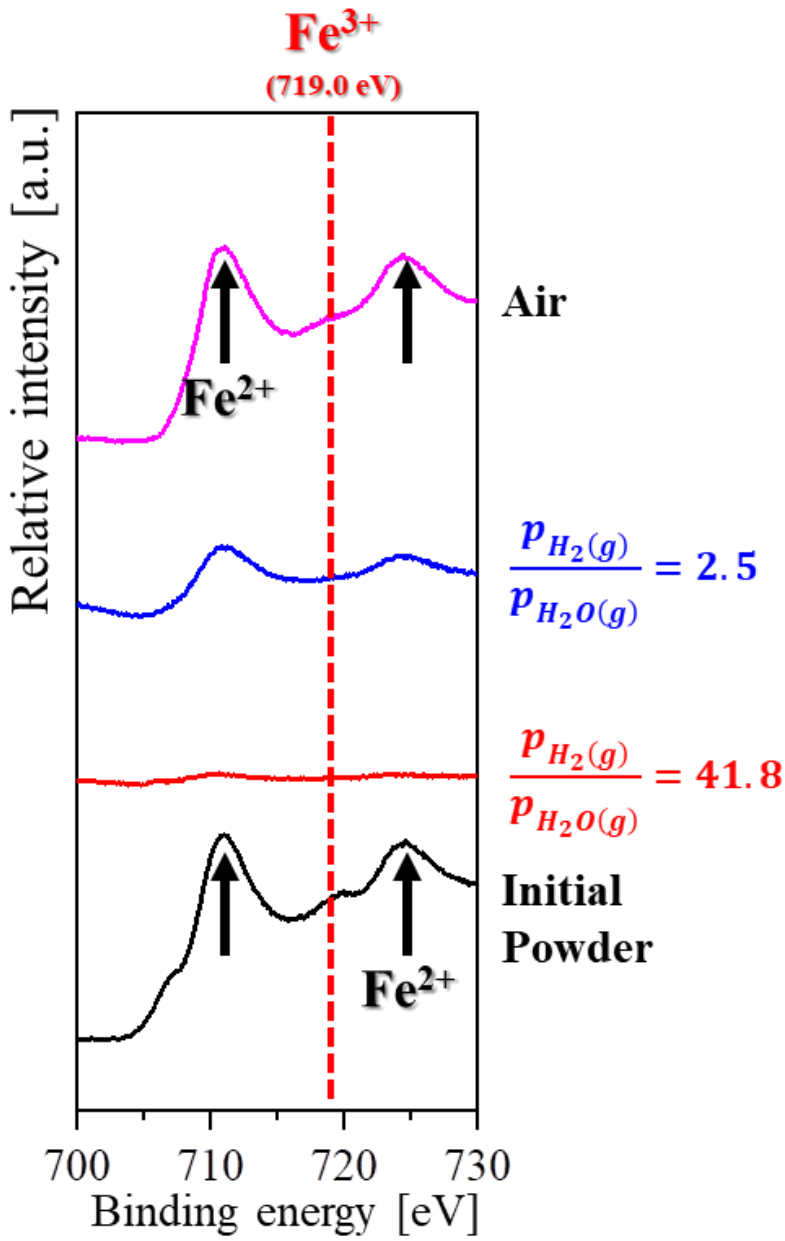

Figure 3.5. The Fe element peak region in XPS.

3.4. Insulation property of Fe−3Si−5.5wt%Cr powder: withstanding voltage test

	Initial powder	Annealed powder		
		$\frac{p_{H_2(g)}}{p_{H_2O(g)}}$ = 41.8	$\frac{p_{H_2(g)}}{p_{H_2O(g)}}$ = 2.5	Air
Oxygen concentration (wt%)	0.188	0.218	0.284	0.368
Withstanding voltage (V)	204	457	558	666

Figure 3.6. Oxygen concentration and withstanding voltage of samples

Figure 3.6 shows the results of changes in oxygen concentration and withstanding voltage according to the annealing conditions. The initial powder's oxygen concentration was 0.188 wt%. In contrast, the powders annealed in the $p_{H_2(g)}/p_{H_2O(g)}$ ratio of 41.8 and 2.5 increased its oxygen concentration to 0.218 and 0.284 wt%, respectively. When the oxidation potential increases by decreasing the $p_{H_2(g)}/p_{H_2O(g)}$ ratio, in the condition where the $p_{H_2(g)}/p_{H_2O(g)}$ ratio is 2.5, the oxygen concentration increased more than the ratio of 41.8. In the powders annealed in the air atmosphere, the oxygen concentration was 0.368 wt%, which is much higher than the above two conditions.

The withstanding voltage is an applied voltage that the insulation can withstand without being destroyed. This means that the higher the withstanding voltage, the better the insulation property. The withstanding voltage of the initial powder was 204 V, and it was much improved to 457 V under the $p_{H_2(g)}/p_{H_2O(g)}$ ratio of 41.8. As the oxidation potential increased during the annealing, the oxygen concentration and the withstanding voltage increased.

3.5 Magnetic property of Fe-3Si-5.5%Cr powder: VSM test

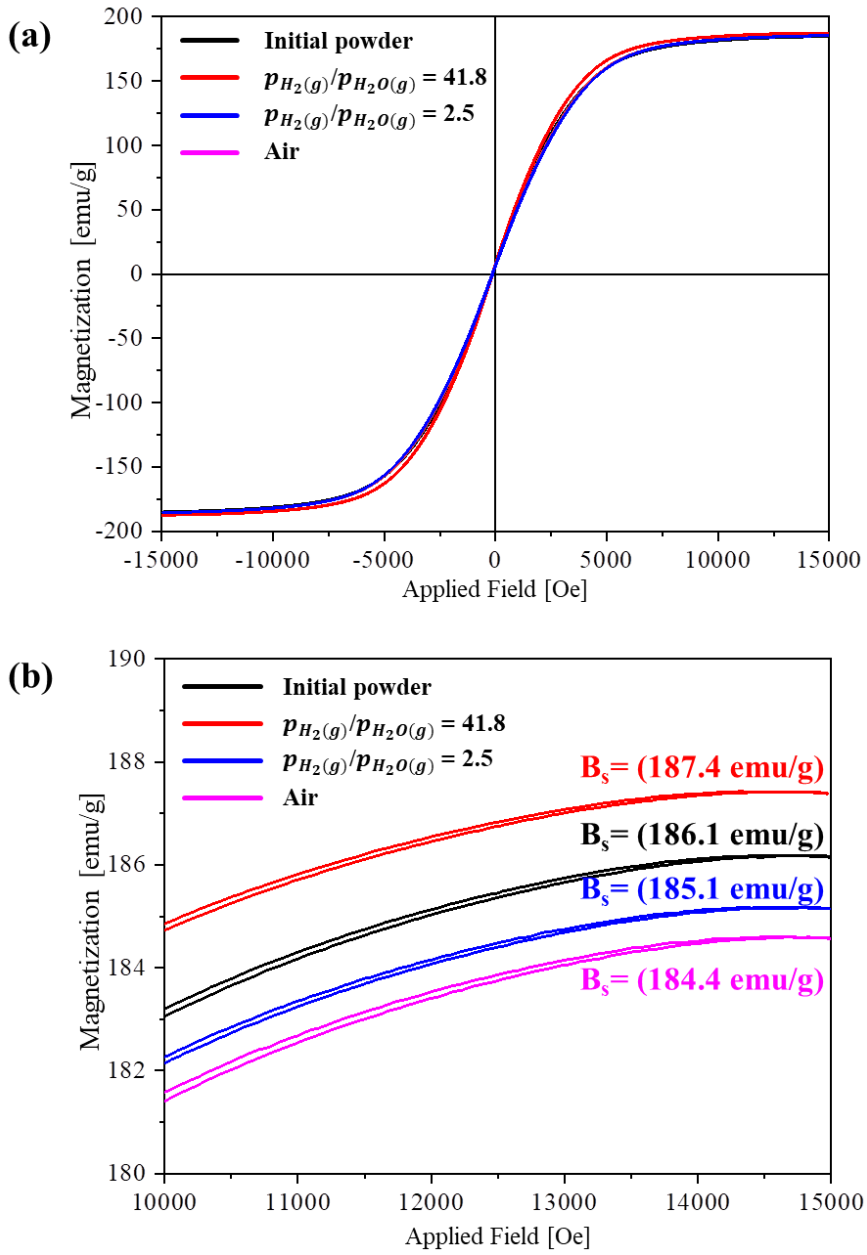

Figure 3.7.(a) The hysteresis loops of the initial and the annealed Fe-Si-Cr powders and (b) their magnified view ranging from 10k to 15 k Oe.

Figure 3.7(a) shows the results of the hysteresis loops of each sample, and Figure 3.7(b) is its magnified view in the region where the magnetic flux density was saturated. The saturation magnetic flux density (B_s) of the initial powder was 186.1 emu/g, which value is similar with the previously reported value (187 emu/g) of the Fe−3.5Si−4.5Cr powders [27]. After the selective oxidation annealing ($p_{H_2(g)}/p_{H_2O(g)}$ = 41.8), B_s slightly decreased to 187.4 emu/g. Meanwhile, in the condition where the $p_{H_2(g)}/p_{H_2O(g)}$ ratio is 2.5, the B_s decreased to 185.1 emu/g, and it was further reduced to 184.4 emu/g after the annealing in the air atmosphere.

When an insulating oxide layer is formed on the powder surface through annealing, the B_s would decrease as elements having magnetic properties are oxidized. Therefore, in the conditions where the powders were annealed in the $p_{H_2(g)}/p_{H_2O(g)}$ ratio of 2.5 and the air atmosphere, the B_s values were further decreased than the selective oxidation condition as the Fe having an excellent magnetic property was oxidized together.

The oxygen concentrations of the powders annealed under the above two conditions were higher than the powders annealed under the selective oxidation condition. This higher increase in the oxygen concentration could affect to the larger decrease in the B_s value. However, the B_s values in Fe-Si based soft magnetic powders are greatly influenced by the Fe concentration. When the concentrations of Si and Cr increase in the powder, resistivity increases, but the B_s value lowers by decreasing the Fe concentration [31]. Therefore, it is thought that the difference in the reduction of the B_s value in this study might be affected by the oxidation of Fe rather than the change of the oxygen concentration.

Comparing the two conditions of the $p_{H_2(g)}/p_{H_2O(g)}$ ratio of 2.5 and the air atmosphere, the oxygen concentration of the powder annealed in the air atmosphere was higher. The larger amount of Fe was oxidized in the air annealing condition due to its high oxidation potential, resulting in a lower B_s value. On the other hand, under the condition where the $p_{H_2(g)}/p_{H_2O(g)}$ ratio is 41.8, the decrease of the B_s value would be relatively low because Fe is not oxidized and only Si and Cr are selectively oxidized.

Chapter 4. Improvement of magnetic & insulation properties of cores fabricated by selectively oxidized Fe-Si-Cr powders compared to wet chemical process

4.1. Selective oxidation by time

In Chapter 3, various annealing conditions (atmospheric oxidation conditions, $p_{H_2(g)}/p_{H_2O(g)}$=2.5, $p_{H_2(g)}/p_{H_2O(g)}$=41.8 conditions) were performed to examine how the powder surface oxide layer was modified through XPS analysis. When selective oxidation annealing condition was applied to the Fe-3Si-5.5wt%Cr powder surface, it was confirmed through XPS composition analysis and VSM analysis that only Si and Cr which have a good insulation property were selectively oxidized on the powder surface uniformly without oxidation of Fe element responsible for magnetic properties of powder.

Therefore, an experiment according to the selective oxidation annealing time was additionally performed to confirm the behavior of forming an oxide layer on the surface of the powder as the selective oxidation annealing time increased under the selective oxidation heat treatment condition ($p_{H_2(g)}/p_{H_2O(g)}$=41.8). Then, a series of powder metallurgy processes were applied to the powders on which the insulating layer was formed by the selective oxidation annealing process and the powder on which the insulating layer was formed by applying the wet chemical process to manufacture a core. Afterwards, the magnetic and insulating properties of the core were compared and analyzed.

4.2. Experimental procedure

The initial powder with a composition of Fe-3Si-5.5Cr (in wt%) was fabricated by a water atomization method. The chemical composition of the water-atomized powder was analyzed by an inductively coupled plasma mass spectrometry (OPTIMA 7300 DV, Perkin-Elmer). The concentrations of Si and Cr in the powder were measured to 3.04 and 5.47 wt%, respectively. Figure 4.1 represents the schematic of the heat treatment furnace used in this study.

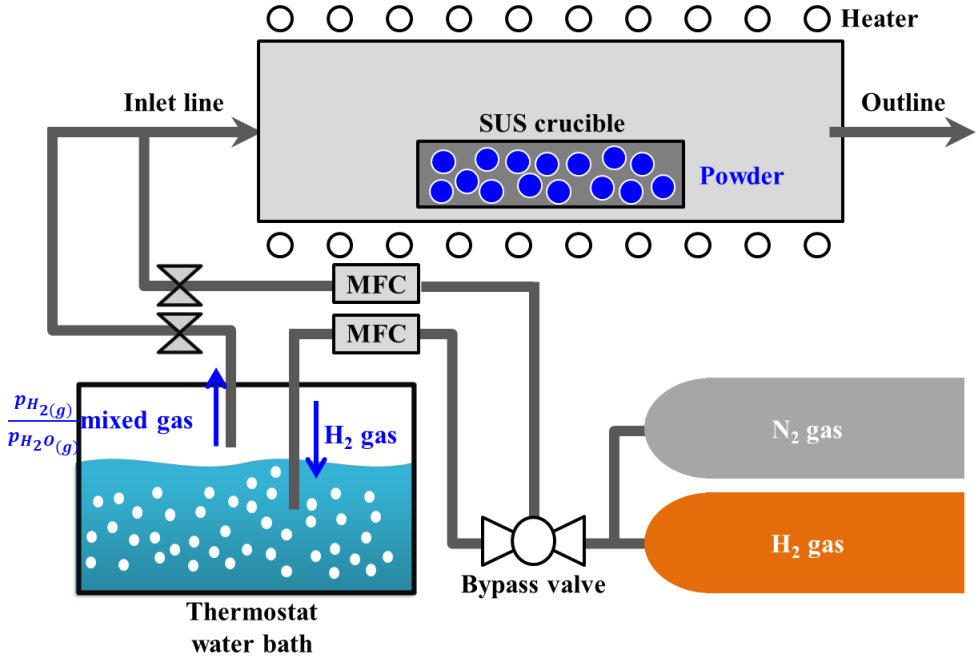

Figure 4.1. Schematic of the heat treatment furnace used in this study. H_2–H_2O mixed gas is supplied to the furnace by bubbling H_2 gas in the thermostat water bath.

The furnace was heated using an electrical resistance heater and sealed to prevent the inflow of outside air. The gas flow rate was controlled by a mass flow controller, and when the pressure inside the furnace was over 780 torr, the gas was exhausted through the check valve to maintain the furnace at a positive pressure.

For the annealing, 250 g of the Fe−3Si−5.5Cr powder was put in a stainless steel crucible. After charging the crucible in the middle of the furnace as shown in Figure 4.1, the selective oxidation annealing was carried out. The heat treatment was performed at 600 ℃ and the holding time was set in three conditions: 30, 60, and 90 min. Hereafter, initial powder and powders after selective oxidation annealing for 30, 60, and 90 min will be designated as NO powder (initial powder), SO30 powder (powder after selective oxidation for 30 min), SO60 powder (powder after selective oxidation for 60 min), and SO90 powder (powder after selective oxidation for 90 min), respectively. To compare the surface and magnetic properties of the selectively oxidized powders, the initial powder was annealed in an air atmosphere for 30 min.

4.2.1 Experimental procedure: Ellingham diagram

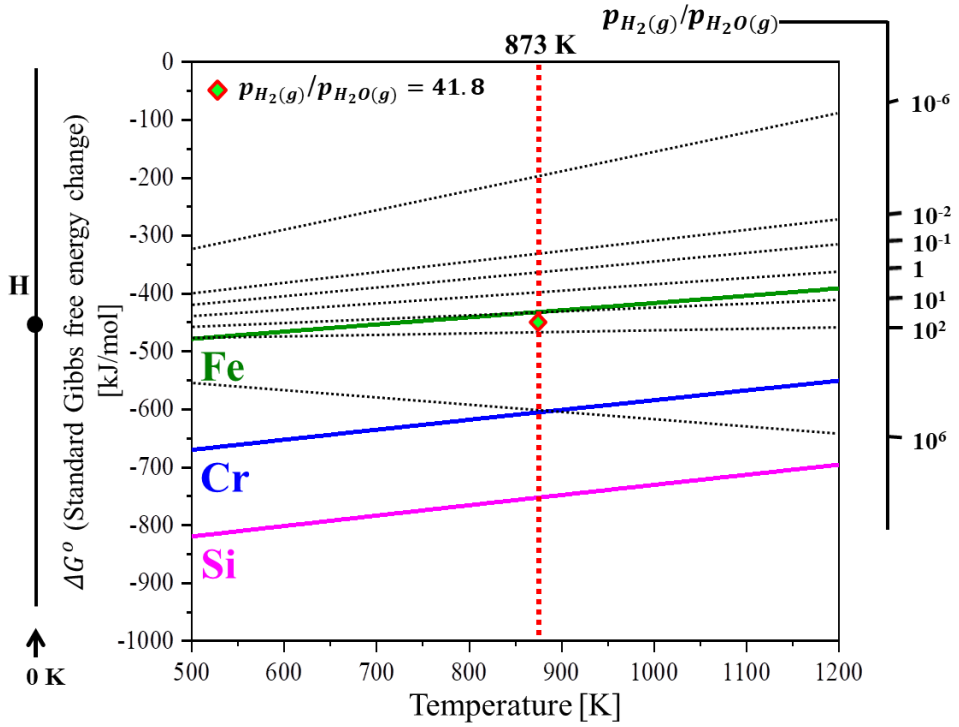

Figure 4.2. Ellingham diagram for selective oxidation condition calculated by Thermo-Calc software

In order to determine the selective oxidation conditions, first, the oxidation driving force for individual Fe, Cr, and Si was calculated using Thermo-Calc software. Figure 4.2 shows the Ellingham diagram for the oxide formation of each elements. Comparing the oxidation driving force for the three elements, Si is the highest, followed by Cr and Fe. Since the oxidation potentials of each element are different, it is possible to from a selective oxidation atmosphere that oxidizes specific elements.

The G^0 values were obtained from Thermo-calc software, and through this, the ΔG^0 values of Fe, Cr, and Si for the oxidation at 600 ℃ were estimated to −432.3, −605.9, and −753.0 kJ/mol, respectively. $(p_{H_2(g)}/p_{H_2O(g)})_{eq}$ at 600 ℃ can be calculated by performing the calculation in Section 2.3. Calculating the $(p_{H_2(g)}/p_{H_2O(g)})_{eq}$ values at 600 ℃ through Eq. (9), the values for Fe, Cr, and Si were 9.65, 1.57×10^6, and 4.09×10^{10}, respectively. Therefore, if the $p_{H_2(g)}/p_{H_2O(g)}$ ratio is controlled in the range of 9.65 and 1.57×10^6 during the heat treatment, only Si and Cr are selectively oxidized.

4.2.2 Experimental procedure: selective oxidation heat treatment

To form an insulation layer on the powder surface by the selective oxidation, the heat treatment was performed while controlling the oxidation potential. In this study, the oxidation potential was controlled by the partial pressure ratio of hydrogen and water vapor ($p_{H_2(g)}/p_{H_2O(g)}$). 100% H_2 gas was firstly injected into the thermostat water bath, and after bubbling in the water, the H_2–H_2O mixed gas was flowed into the furnace with the flow rate of 2 slm. The $p_{H_2(g)}/p_{H_2O(g)}$ ratio was controlled by the temperature of the water in the thermostat bath.

In this study, the water temperature of the thermostat bath was maintained at 20 ℃, and when calculating the $p_{H_2(g)}/p_{H_2O(g)}$ ratio, it was determined to 41.8. A series of thermodynamic calculations were performed through Eq. (12) in section 2.4. When the H_2–H_2O mixed gas is supplied from the thermostat bath to the heat treatment furnace, the $p_{H_2(g)}/p_{H_2O(g)}$ ratio could be changed by the condensation of water vapor. To supply the mixed gas with a constant $p_{H_2(g)}/p_{H_2O(g)}$ ratio, it is necessary to prevent condensation of water vapor in the gas line. Therefore, the gas inlet line was wrapped with a heating band and heated to 50 ℃.

To form a selective oxidation atmosphere only during the holding time at 600 ℃, 100% dry H_2 gas was injected into the furnace using the bypass valve in the heating and cooling process. The powders were heated with a heating rate of 10 ℃ /min. After reaching at 600 ℃, then H_2 gas was bubbled into the thermostat water bath and then the H_2–H_2O mixed gas was injected into the furnace. After finishing holding at 600 ℃, the powders were furnace cooled to room temperature.

4.2.3 Experimental procedure :powder analysis

The morphology of prepared samples was observed by using a field emission-scanning electron microscope (FE-SEM) (QUANTA FEG 250, FEI) and the powder size distribution was analyzed by using a powder size analyzer (Mastersizer 3000, Malvern). The oxygen concentrations of the powders before and after the selective oxidation annealing were analyzed using a NO analyzer (736 series, LECO). The cross-section of the powders was observed by electron probe microanalysis (EPMA) (JXA8530F, JEOL). To examine the changes of chemical compositions in oxide layers of the powders, the samples were analyzed using an X-ray photoelectron spectroscopy (XPS) (K-Alpha, ThermoFisher). The morphologies of the oxide layers were observed by a transmission electron microscope (TEM) (Titan G2 ChemiSTEM Cs Probe, FEI) equipped with energy dispersive X-ray spectroscopy (EDS). The TEM samples were prepared using a focused ion beam (Versa 3D, FEI). The magnetic properties of the powders were investigated with a vibrating sample magnetometer (VSM) (7404-S, Lake Shore).

Figure 4.3(a) shows the morphology of the water-atomized Fe-Si-Cr powder (initial powder) used in this study observed by the FE-SEM. The powder had an irregular shape, which is a common feature of powders fabricated by the water atomization method [32]. The powder size distribution was measured by the powder size analyzer, and the result is represented in Figure 4.3(b). The d_{10}, d_{50}, d_{90} values of the powder were 3.8, 10.5, 21.7 μm, respectively. And the oxygen concentration of the initial Fe-3Si-5.5wt%Cr powder was measured to be 0.199 wt%.

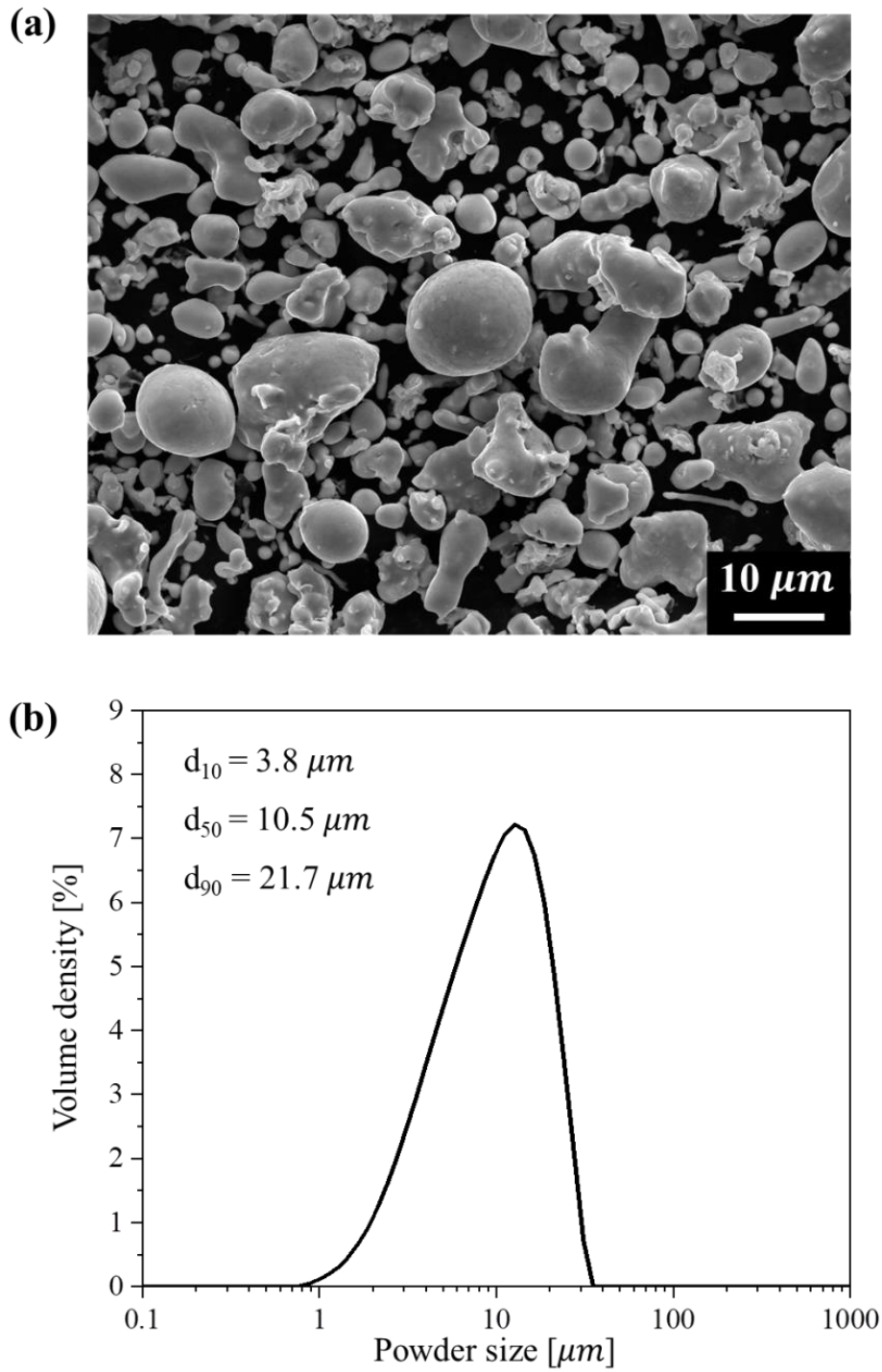

Figure 4.3. (a) Morphology and (b) powder size distribution of the water-atomized Fe-3Si-5.5wt%Cr powder.

4.3. Oxidation layer growth by selective oxidation time

Figure 4.4 shows the oxygen concentrations of the NO powder and the powders after selective oxidation annealing. The oxygen concentration of the NO powder was 0.199 wt%. As the selective oxidation annealing time increased, the oxygen concentration of the powders increased. The oxygen concentrations of the SO30, SO60, and SO90 powders were increased to 0.329, 0.409, and 0.486 wt%, respectively.

Sample	**NO powder**	**SO30 powder**	**SO60 powder**	**SO90 powder**
Oxygen concentration [wt%]	0.199	0.329	0.409	0.486

Figure 4.4. The oxygen concentration of the NO, SO30, SO60, and SO90 powder samples.

Figure 4.5(a) and (b) are the composition mapping results in the cross-section of the NO and SO90 powders observed by EPMA at low magnification, respectively. Regions with high and low concentrations are represented in red and black colors. Looking at the cross-sections of the NO and SO90 powders, Fe, Cr, and Si were uniformly distributed. On the other hand, the oxygen mapping result showed that the oxygen concentration on the surface of the SO90 powder was higher than that of the NO powder. Figure 4.5(c) shows the oxygen concentration mapping results of the NO and SO90 powders at high magnification. Enrichment of oxygen on the surface was clearly observed on the surface of the SO90 powder only.

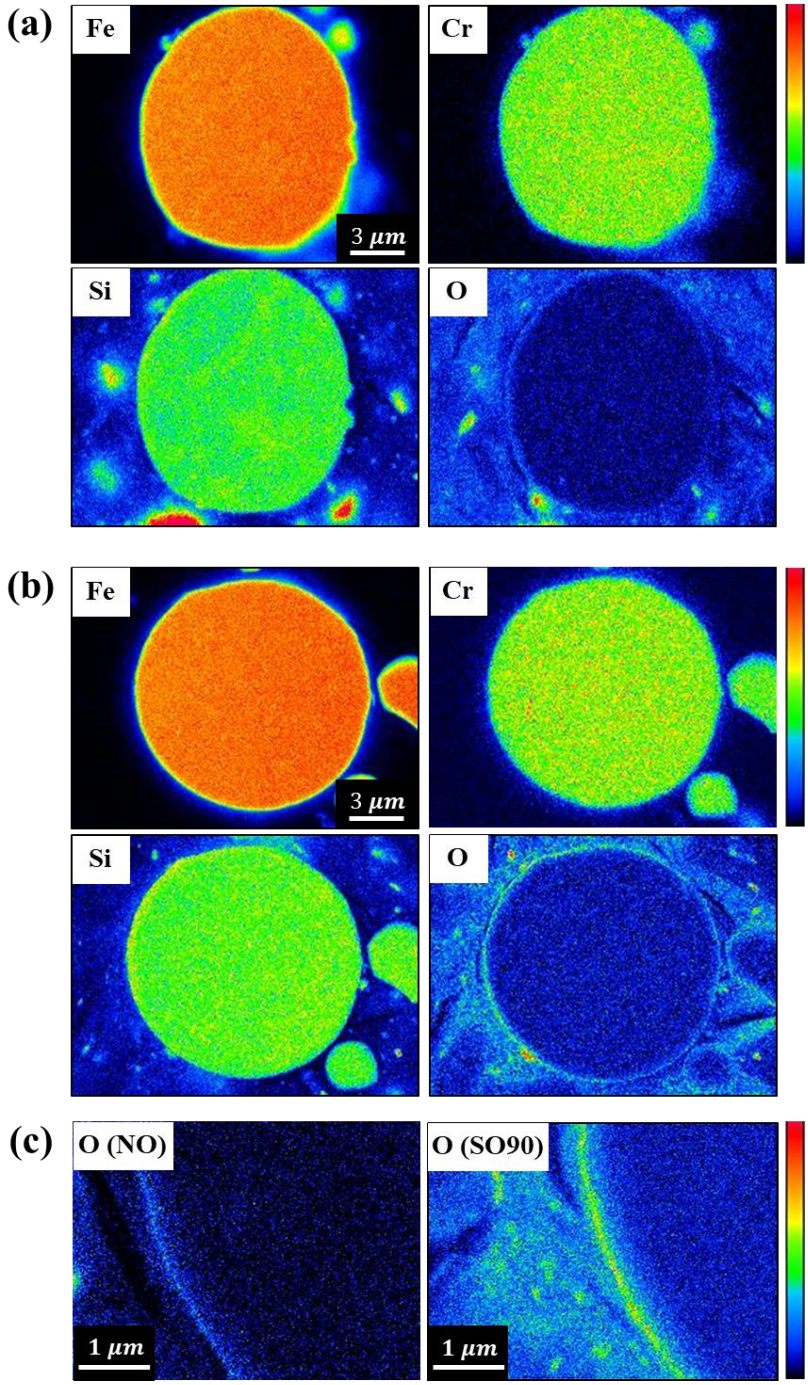

Figure 4.5. Concentration mapping results of the (a) NO power and (b) SO90 powder analyzed by EPMA in the cross-section. (c) The oxygen concertation mapping results for both samples at high magnification.

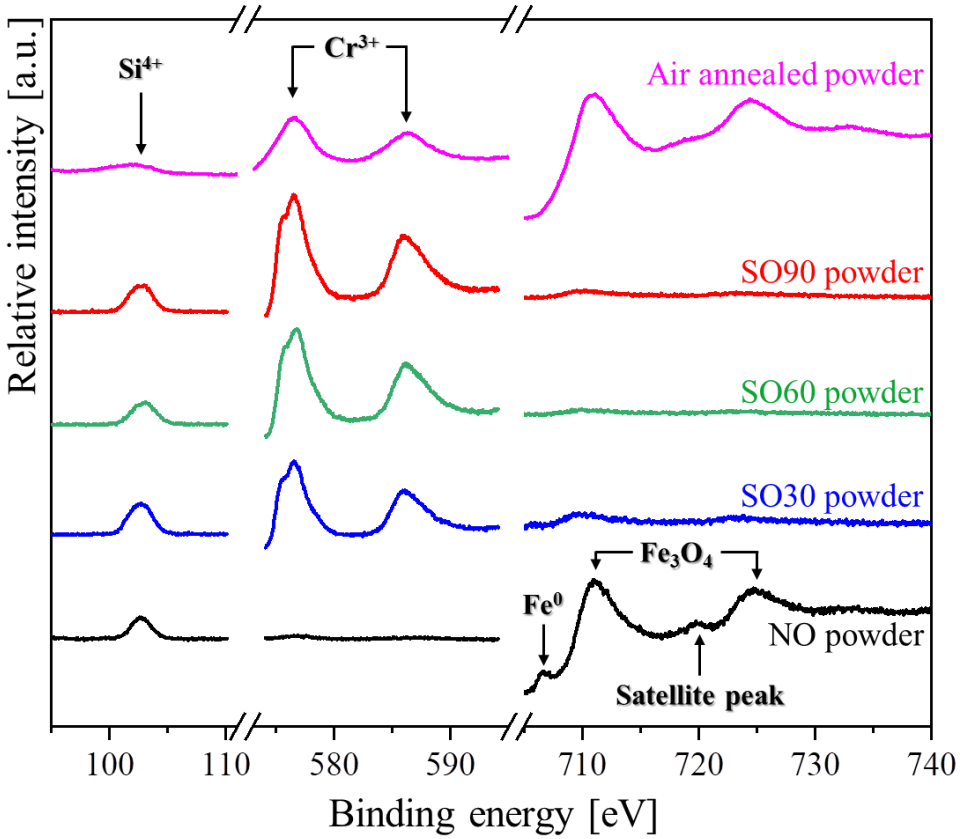

Figure 4.6. XPS spectra of the NO, SO30, SO60, and SO90 powder samples. XPS spectrum of the powder annealed in the air atmosphere was represented to compare with the changes in the oxide layer by the selective oxidation annealing.

To investigate the changes in the oxide composition by the selective oxidation annealing, the surface of the powders was analyzed by XPS, and the results are shown in Figure 4.6. In the XPS spectrum of the NO powder, the strong peaks at 710.9 and 724.2 eV were observed. These peaks are related to ion state of Fe, which are attributed to 724.2 eV for 2p1/2 peak and 710.9 eV for Fe 2p3/2 peak. Also, a satellite peak corresponding to Fe^{3+} was detected at 719.0 eV [33]. In addition, a minor peak was observed at 707.0 eV, which is attributed to the metallic state of Fe (Fe^{0}) [34]. Since the oxide layer of the NO powder would be very thin, the peak from the bulk metal was detected together with peaks from the oxide layer in the XPS spectrum. In the Si spectrum region, a strong peak was observed at 103.6 eV, which peak is the 4+ oxidation state of Si (Si 2p3/2) [35]. In the Cr spectrum region, no definite peak was detected.

In the XPS spectra of the SO30, SO60, and SO90 powder samples, the peak intensity in Fe region was greatly reduced. While the strong peaks at 576.6 and 585.7 eV, which are attributed to Cr^{3+} oxidation state of Cr2p3/2 and Cr 2p1/2 [36, 37], newly appeared. A shoulder peak formed by the multiplet interactions was observed at 575.4 eV, slightly to the left side of the Cr2p3/2 peak (576.6 eV) [38]. As the oxidation time increased, the peak intensity of Si was slightly decreased and that of Cr was slightly increased. In all three samples, the Fe^{0} state peak was not observed, because the oxide layers would be thickened by the selective oxidation annealing.

In the XPS spectrum of the powder annealed in the air atmosphere, the oxide layer was different from that of the selectively oxidized powders. In the air annealing condition, it is not an atmosphere in which only a specific element is selectively oxidized, but an atmosphere in which all elements constituting the Fe-Si-Cr alloy are oxidized. Therefore, although Cr and some Si were present in the oxide layer, Fe-rich oxide layer was formed on the air annealed powder because Fe content is the highest in the Fe-Si-Cr alloy powder.

(a)

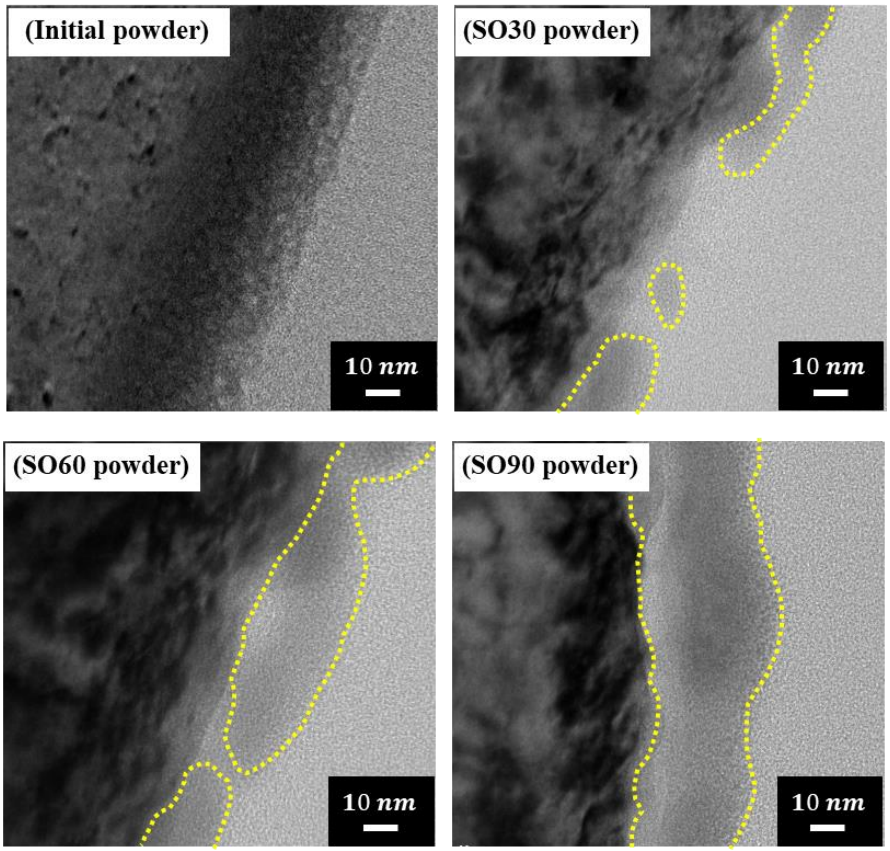

(b)

Sample	Initial powder	SO30 powder	SO60 powder	SO90 powder
Oxide layer thickness [nm]	-	19.7	31.5	51.4

Figure 4.7.(a) TEM morphology of NO, SO30, SO60, SO90 powders (b) oxide layer thickness of each powders

To examine the oxide layer change induced by the selective oxidation annealing, the oxide layers of the NO, SO30, SO60 and SO90 powders were analyzed by TEM and the results are shown in Figure 4.7. In Figure 4.7(a), no oxide layer was observed on the surface because the NO powder did not undergo oxidation heat treatment.

TEM image of the SO90 powder, an oxide layer with a thickness of 51.4 nm, was formed on the powder surface. Additional TEM observations of the SO30 and SO60 powders revealed an oxide layer thickness of 19.7 and 31.5 nm, respectively. The oxide layer thickness is summarized in Figure 4.7(b). The oxide layers are thus confirmed to gradually thicken with increasing the selective oxidation annealing time.

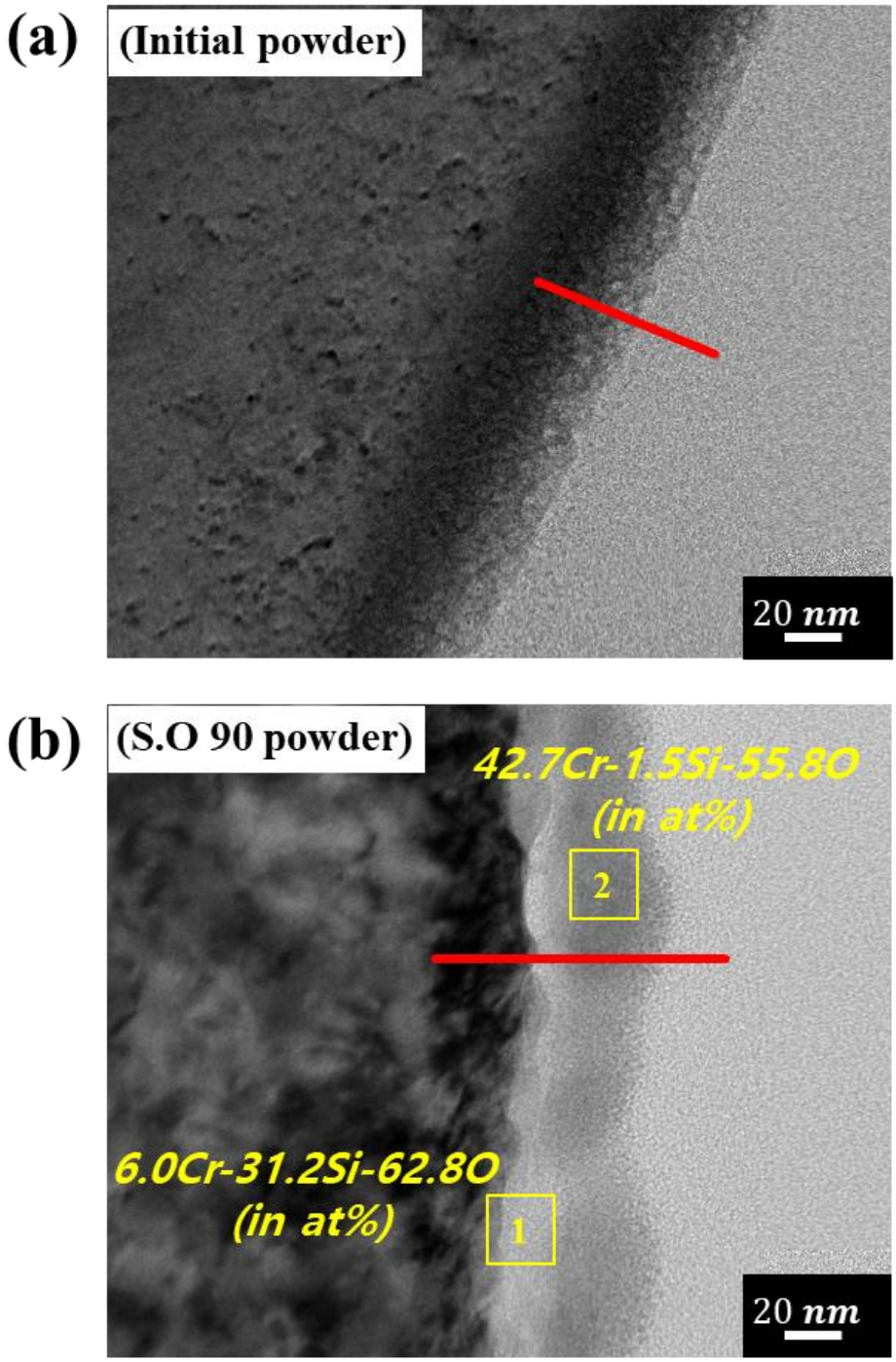

Figure 4.8. TEM-EDS component analysis of surface oxide layer of (a) NO and (b) SO90 powder

Figure 4.8(a), (b) shows the results of component analysis of the surface oxide layer of NO and SO90 powder. As mentioned above, the oxide layer was not measured on the surface of NO powder as it was formed very thin, but in the case of SO 90 powder, the oxide layer was formed as a double layer, and it was observed that Si oxide was formed inside and Cr oxide was formed outside. The compositions of the Cr-rich and Si-rich oxide layers, analyzed by EDS, were 42.7Cr-1.5Si-55.8O and 6.0Cr-31.2Si-62.8O (in at%), respectively. The Cr-rich and Si-rich oxide layers have a similar composition with the Cr_2O_3 and SiO_2, respectively.

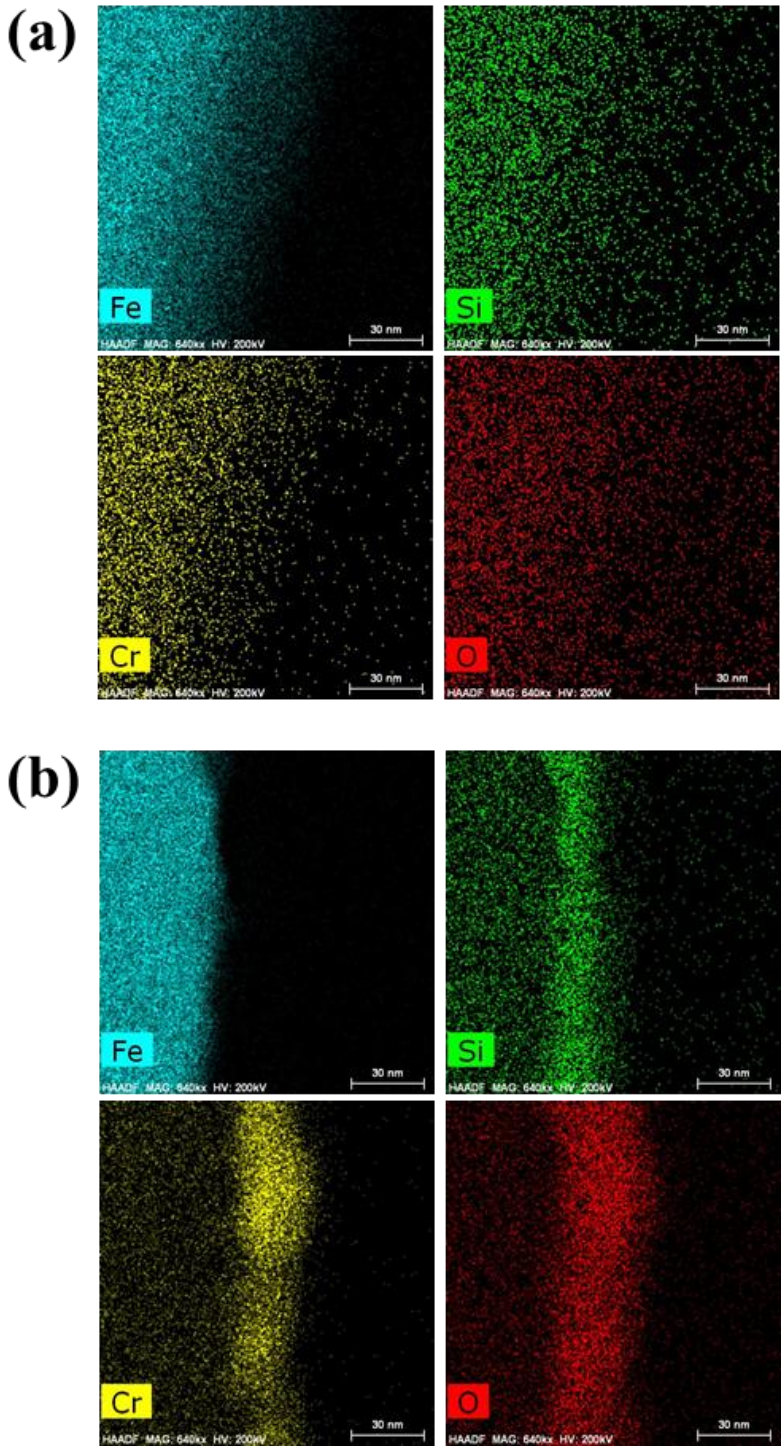

Figure 4.9. The composition mapping results of the initial and SO90 powder surface, respectively.

Figure 4.9(a) and (b) show the composition mapping results of the NO powder and SO90 powder surface, respectively. In the results, a region with higher oxygen concentration was not observed on the initial powder surface, confirming there is no oxide layer or a very thin oxide layer on the powder surface. In the XPS spectrum of the initial powder, therefore, the Fe^0 peak from the bulk metal was detected together with the ion state peaks from the oxide layer (Figure 4.6).

Figure 4.9(b) is the composition mapping results of the area of Figure 4.8(b) and the oxide was found to form as a double layer. A Cr-rich oxide layer was formed on the outermost layer and a Si-rich oxide layer was formed under it. This double oxide layer structure is commonly formed in the oxidation of the Fe-Si-Cr ternary alloy [39, 40]. Indeed, a Si oxide layer is firstly formed, and at this stage the oxidation potential on the powder surface is lowered by the oxidation of Si [41, 42]. As a consequence of this low oxidation potential, the external oxidation of Cr occurs, which results in the double oxide layer structure [43].

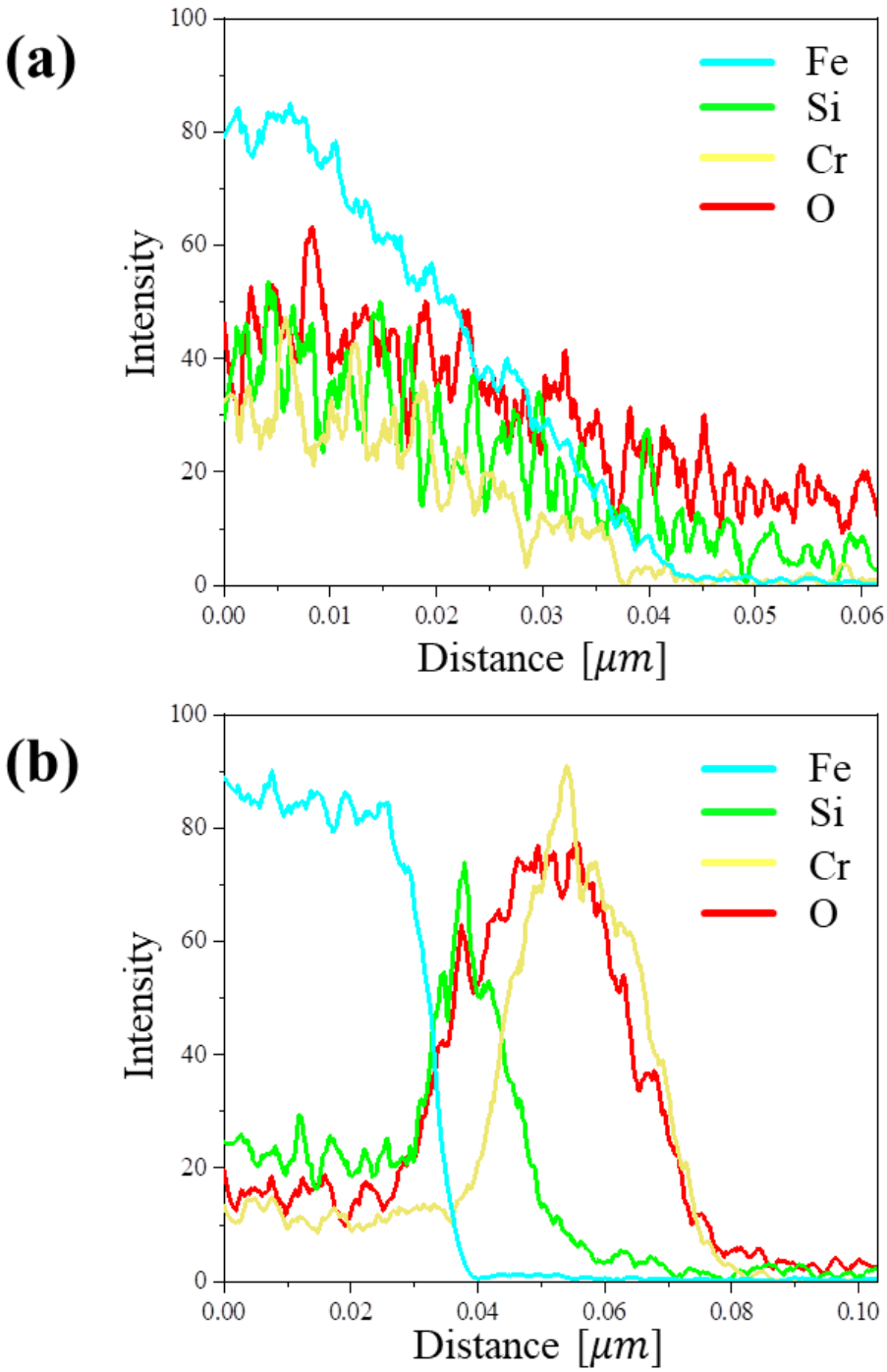

Figure 4.10. The composition mapping results of the initial and SO90 powder surface, respectively

Figure 4.10(a),(b) are the composition line scan results along the red line in Figure 4.8(a),(b). This result also clearly showed that the oxide layer on the SO90 powder was formed as a double layer, and the thickness of the Cr-rich and Si-rich oxide layers were 31.6 and 19.8 nm, respectively.

4.4. Magnetic property of powders : VSM analysis

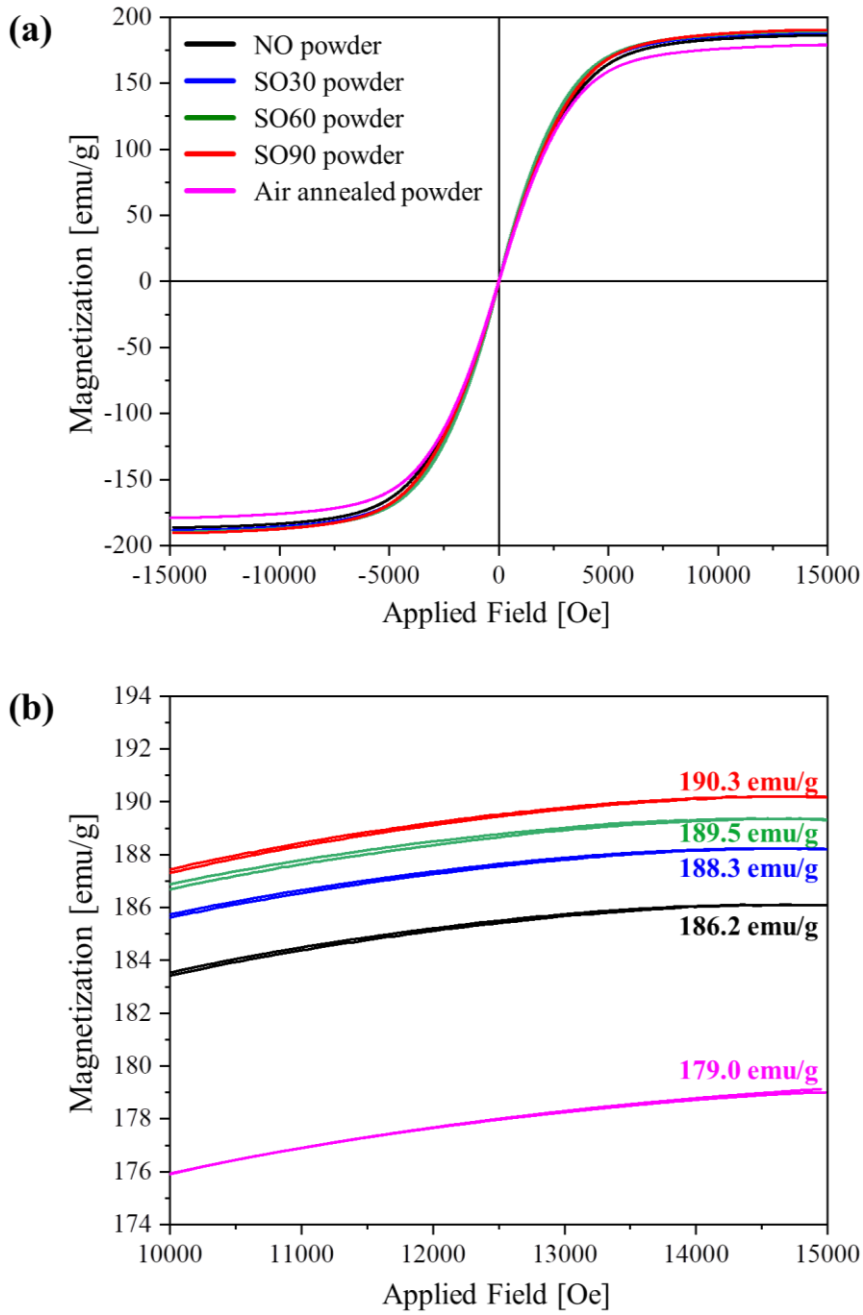

Figure 4.11. (a) VSM results of the NO, SO30, SO60, SO90, and air annealed powders and (b) the result shown in the applied field range from 10,000 to 15,000 Oe.

Figure 4.11(a) shows the magnetic properties of the NO, SO30, SO60, SO90, and air annealed powders analyzed by VSM. Overall, there was no significant change in the shape of the graph. However, the SO powders tended to have an improved permeability (μ) and a saturated magnetic flux density (B_s) compared to the NO powder. To investigate the B_s changes in detail, the applied field only in the range of 10,000 ~ 15,000 Oe is shown in Figure 4.11(b). The B_s values were estimated at 15,000 Oe, and found to be 186.2, 188.3, 189.5, and 190.3 emu/g for NO, SO30, SO60, and SO90 powders, respectively. Mori et al. [44] reported a comparable B_s value of 188 emu/g for Fe-3.5Si-4.5Cr raw powder and observed a decreasing tendency after insulation coating process, consistently with general behavior reported for coated Fe-Si-Cr soft magnetic materials.

However, in this study, as the selective oxidation annealing time increased, the B_s value improved even though the oxygen concentration increased (Figure 4.4). In the XPS results (Figure 4.6), the oxide layer of the NO powder was mainly composed of Fe. After the selective oxidation annealing, the composition of the oxide layer was changed, and SiO_2 and Cr_2O_3 double oxide layer was formed on the powder surface. Therefore, the reason for the increase in the B_s value seems to be that Fe with a high magnetic characteristic was reduced, and only Si and Cr, which are nonmagnetic elements, were oxidized. And it can be seen that as the selective oxidation heat treatment time increases, the coercivity of powders decreases due to stress relief. This was shown in Figure 4.12.

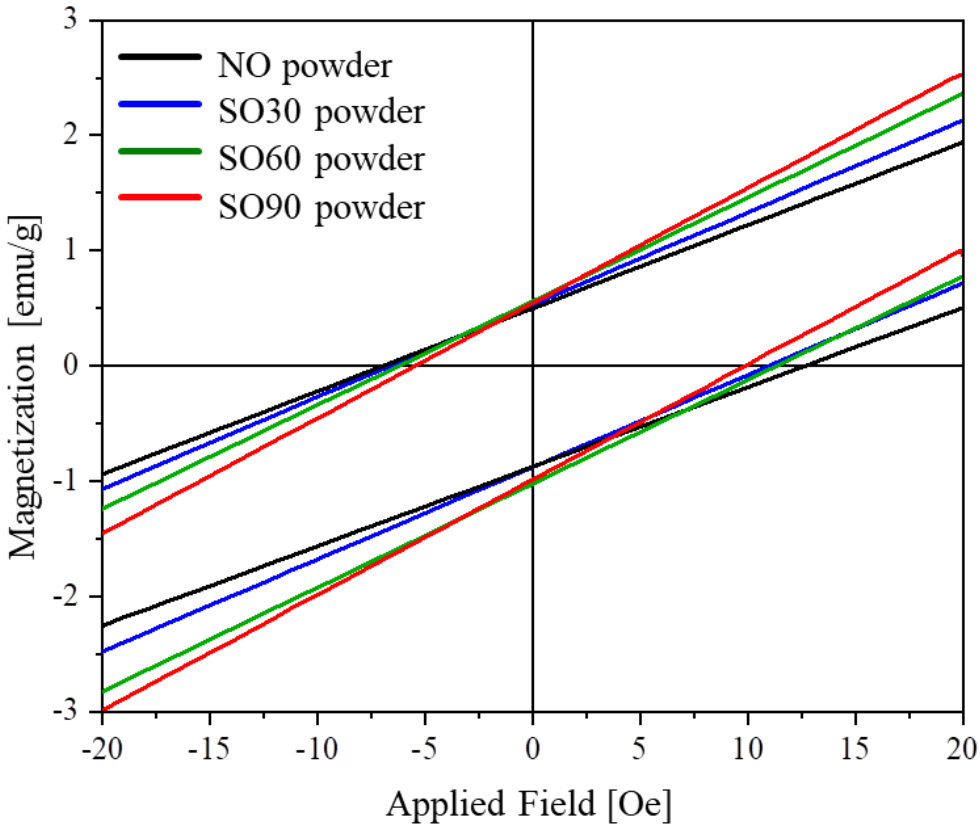

Figure 4.12. Coercivity result of NO, SO30, SO60 and SO90 powder shown in the applied field range from −20 to 20 Oe.

The B_s value estimated at 15,000 Oe of the air annealed powder was 179.0 emu/g, which value is lower than that of the NO powder (186.2 emu/g). As shown in the XPS result, the Fe-rich oxide layer was formed on the powder surface after annealing in the air atmosphere. In the Fe-Si-Cr powder, an insulating oxide layer could be formed on the powder by self-oxidation at high temperatures [30]. However, in the air annealing, Fe with an excellent magnetic properties is also oxidized, so the B_s value would be decreased. Therefore, to simultaneously improve insulation and magnetic properties, it is necessary to selectively oxidize Si and Cr by adopting the selective oxidation annealing.

4.5. Experimental procedure: conventional wet chemical process

The NO powder was insulated through a wet chemical process using a phosphate and liquid sodium silicate to form a phosphate and SiO_2 double insulation layer, which process is generally used for the insulation of the SMC because of the anti-corrosion ability and improvement of adhesion [5, 45]. In the case of wet chemical process, phosphate was first mixed with acetone solvent and then FeSiCr powder was mixed and stirred until the solvent was evaporated. At this time, phosphate is added at a ratio of 0.2 wt% and acetone at a ratio of 1.5 wt% of FeSiCr powder. Then, the double insulating layers were formed using water glass (liquid sodium silicate). At this time, the rust prevention treatment was also performed in parallel. The main component of the rust inhibitor was SiO_2. Water was used as the solvent, and Si in an ionic state was adsorbed on the surface by a wet chemical process. After forming the insulating layer, a drying process was performed at 60 ℃ for 12 hours to evaporate water solvent.

4.5.1 Experimental procedure: fabrication of SMC cores by powder metallurgy process

After that, the NO powder was mixed with 5 wt% of phenolic resin and 0.5wt% of silane and 5 wt% of acetone solvent for the press molding. Here, silane induces adsorption of inorganic and organic substances, and acetone acts as a solvent. The SO30, SO60, and SO90 powders were directly mixed with the phenolic resin since already insulated by the selective oxidation annealing. After volatilizing the acetone, the powder was dispersed through 400 μm sieving to secure fluidity during uni-axial press molding. After that, powder was dried in an oven at 85 ℃ for 2 hours. If the drying process is not performed, cracks may occur in the core during press molding. After the drying process, 400 micrometer sieving was performed once again, followed by the pressing process.

The powders after mixing with the resin were press molded to a disk shape (20 mm in diameter × 7.35 mm in height) and a toroidal shape (20mm in outer diameter × 10mm in inner diameter × 7.35mm in height). To prevent powder from sticking to the press mold during pressing, 0.3 wt% of zinc stearate lubricant was added. The density of the cores was prepared at 5.75 g/cm^3. When the size factor of the toroidal core was fixed, the permeability of toroidal cores could be directly compared because the size factor was fixed when the inductance was measured and converted into permeability.

After press molding, heat treatment was performed at 160 ℃ in air for 2 hr to cure the binder. Insulation and magnetic properties were evaluated from disk and toroidal core samples, respectively. Hereafter, disk and toroidal core samples fabricated by the NO powder will be designated as NO disk and NO toroidal core and that fabricated by the SO powders will be designated as SO disks and SO toroidal cores.

4.6 Analysis : Insulation and magnetic properties of disk and toroidal core

The withstanding voltages were measured from the disk samples using a withstanding voltage tester (AC/DC HIPOT TESTER 19052, Chroma). The bulk resistivity was measured in the disk samples by a super megohmmeter (SM-B215, HIOKI). The specific resistivity of the samples was calculated from the bulk resistivity considering a shape factor. The inductance and quality factor were analyzed from the toroidal core samples. For the analysis, the toroidal cores were wounded by the copper wire for 10 turns. The inductance and quality factor were measured using an impedance analyzer (Agilent E4990A, Keysight) in the frequency range from 0.1 to 100 MHz. The permeability of toroidal cores was calculated from the inductance value. The core loss was analyzed from the toroidal core samples. For the analysis, the toroidal cores were wounded by the copper wire for 18 turns. The core loss was measured using a B-H chamber system (IE-1123, IWATSU) in the frequency range from 10 to 100 KHz at 50mT.

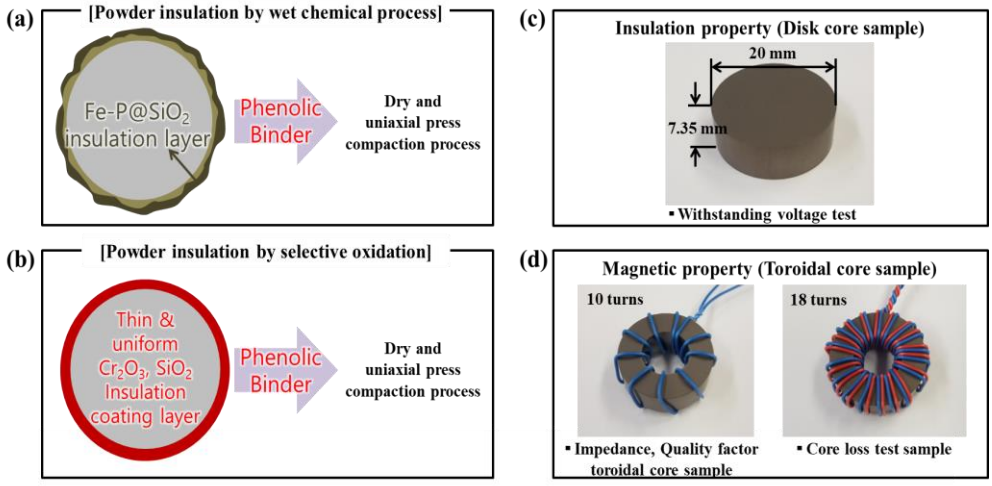

Figure 4.13.(a) Powder with a phosphate−SiO_2 double insulating layer on the surface by applying a wet chemical process (b) powder with an insulating layer on the surface by applying selective oxidation heat treatment (c) a disk core manufactured for the analysis of the insulation property of the core (d) toroidal cores manufactured for the analysis of the magnetic properties of the core Impedance was measured by winding a wire 10 times, and core loss was measured by winding a wire 18 times.

4.7 Insulation property of SMC core: Withstanding voltage test

To confirm whether or not the insulation and magnetic properties can be improved by the selective oxidation annealing, the powders were prepared as disk and toroidal core samples. Figure 4.14(a), (b) show the microstructure of the toroidal cores fabricated from the NO and SO 90 powders.

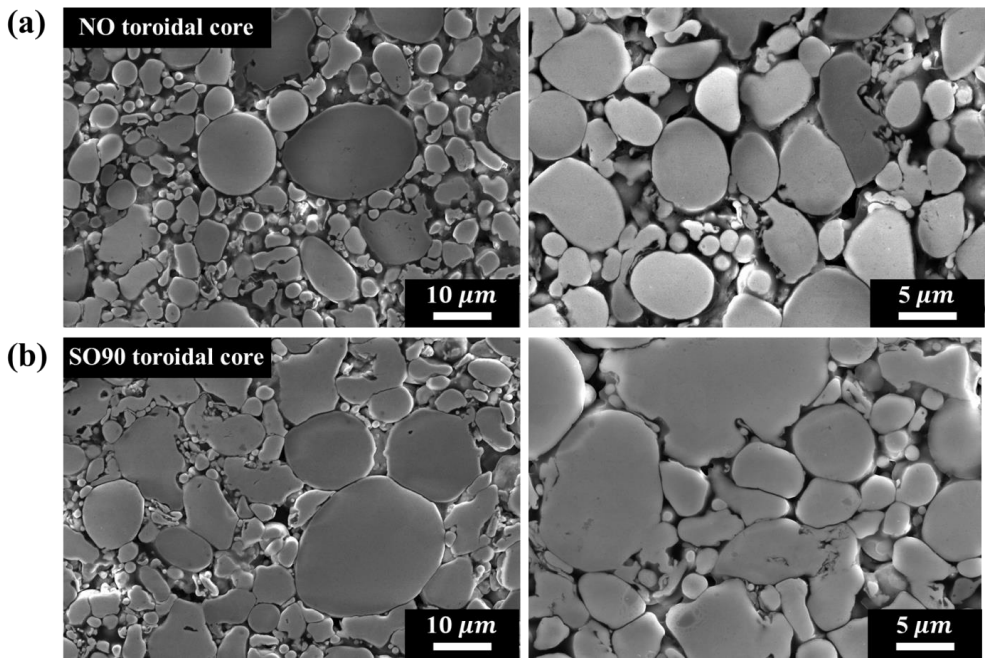

Figure 4.14. Cross-section microstructure of the (a) NO toroidal core and (b) SO90 toroidal core observed by the FE-SEM.

The figures on the left and right show the microstructures at low and high magnification, respectively. For fabricating the NO toroidal cores, the insulation coating layer was formed on the outer surface of the NO powder by the wet chemical method. Therefore, in the microstructure of the NO toroidal core (Figure 4.14(a)), there were spaces between the powders because of the insulating materials. The SO90 toroidal core (Figure 4.14(b)) possesses a higher packing density than the NO toroidal core because the SO90 powder was only mixed with the binder without any additional non-magnetic insulation coating materials.

EPMA analysis was performed to analyze the components of the cross section of the disk cores. Figure 4.15 and Figure 4.16 are Concentration mapping result of the NO disk core and SO90 disk core by EPMA in the cross-section respectively. In the case of the NO disk core (Figure 4.15) manufactured by applying the wet chemical process, it was confirmed that a non-uniform insulating layer was formed between powders. On the other hand, in the case of the SO 90 disk core (Figure 4.16), it was confirmed that a uniform and dense oxide layer was formed between powders.

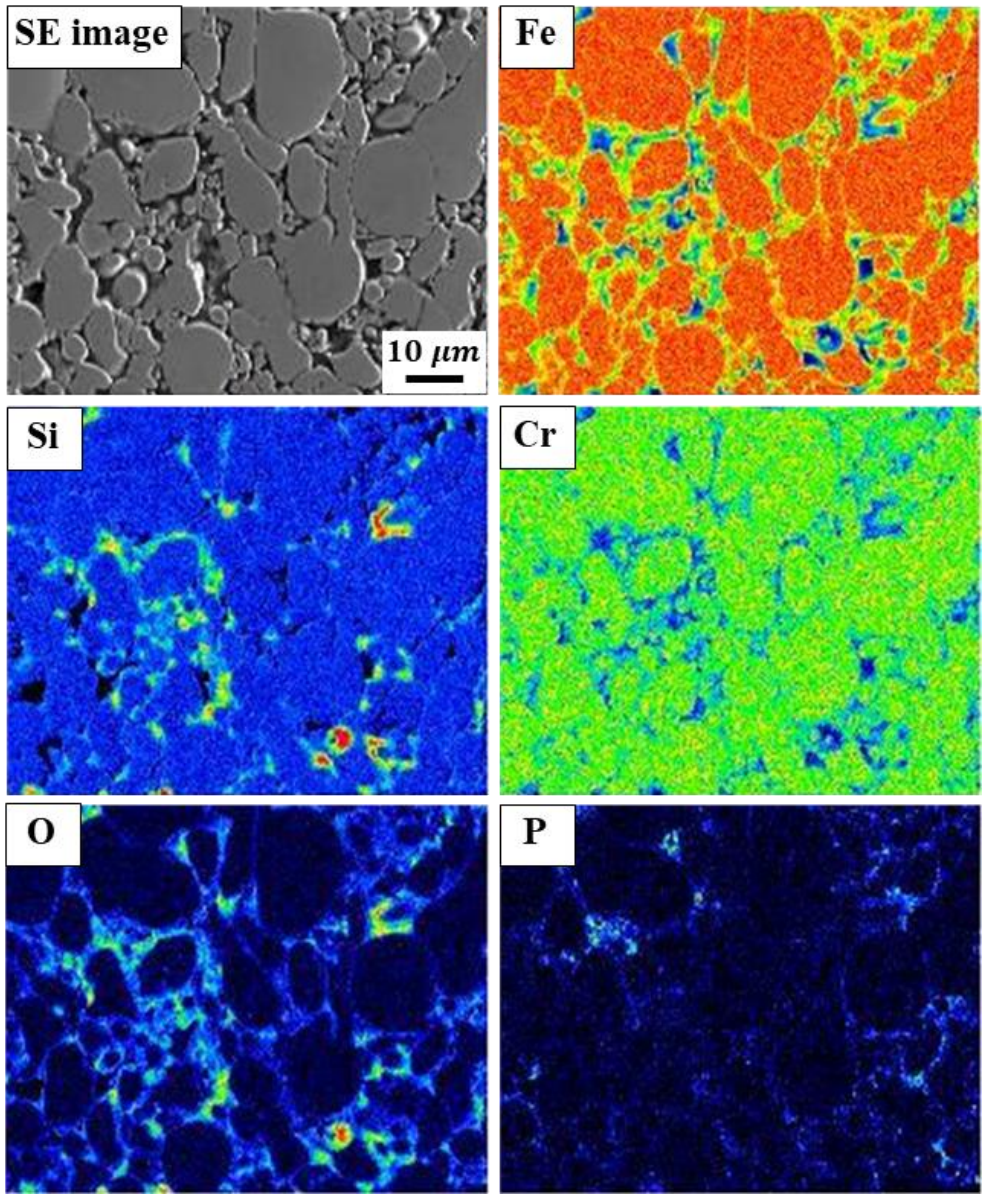

Figure 4.15. Concentration mapping result of the NO disk core by EPMA in the cross-section

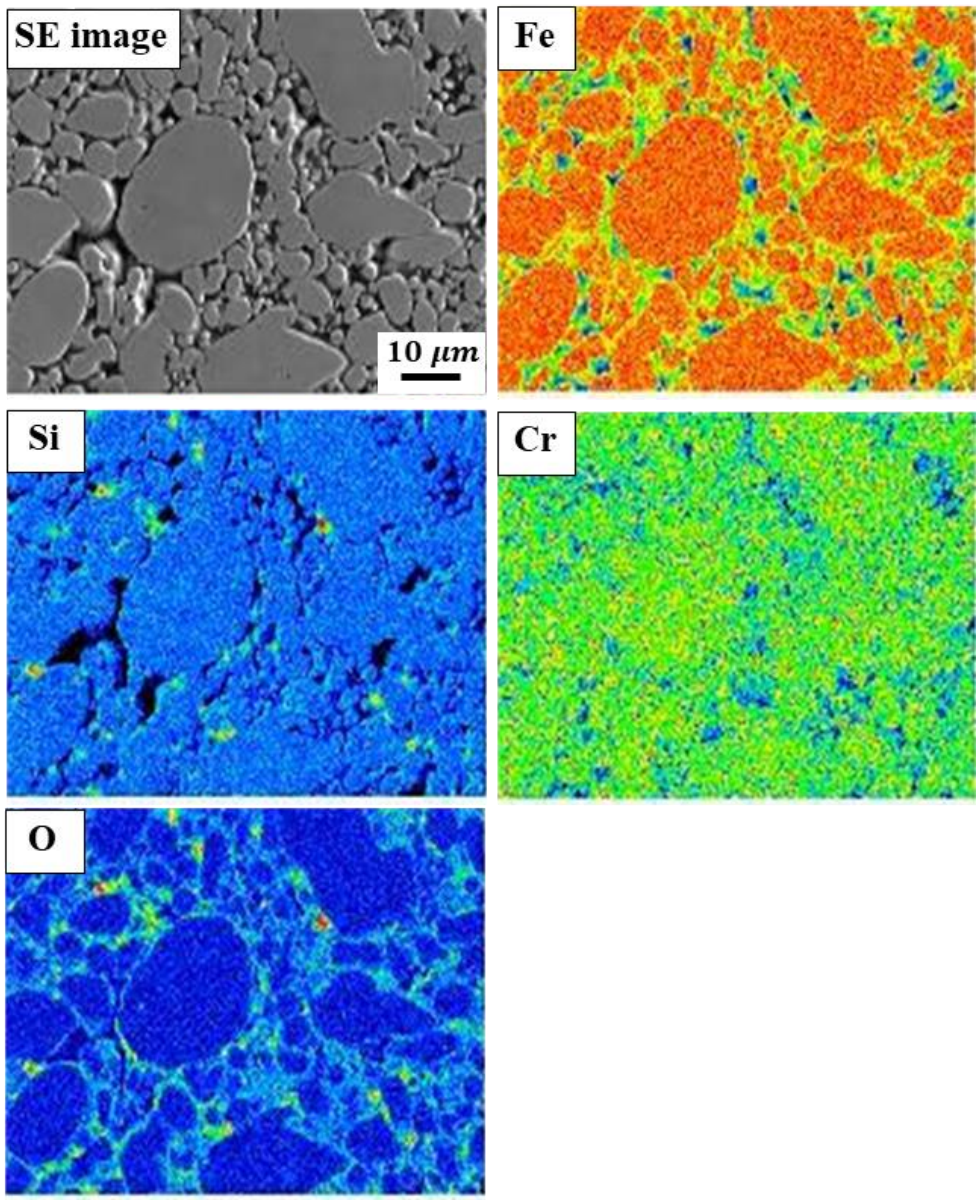

Figure 4.16. Concentration mapping result of the SO 90 disk core by EPMA in the cross-section

To confirm that the insulation property can be improved or not, the insulation properties of the disk samples were compared by withstanding voltage tests. The withstanding voltage is the voltage at which the insulation layer is destroyed when a voltage is applied [46]. High withstanding voltage means that the sample can maintain insulation up to a high voltage.

Figure 4.17 shows the withstanding voltages of the disk samples. When compare the relationship between the oxygen concentration of the powders (Figure 4.4) and the withstanding voltage of the samples, it is confirmed that as the oxygen concentration of the powder increased, the withstand voltage also showed a proportional tendency. The withstanding voltages of the NO, SO30, SO60, and SO90 disk samples were 495, 719, 918, and 1174 V, respectively. The withstanding voltage not only improved after SO (as compared to NO disk), but also increased along with increasing the selective oxidation time. Since the oxide insulation layer was thickened with the annealing time, the withstanding voltage gradually improved. The specific resistivity values of the NO, SO30, SO60, and SO90 disk samples were calculated from the bulk resistivity and they were 1.75×10^{8}, 3.80×10^{8}, 2.94×10^{9}, and 1.57×10^{10} $\Omega \cdot$ cm, respectively. As the selective oxidation annealing time increased, the specific resistivity was increased.

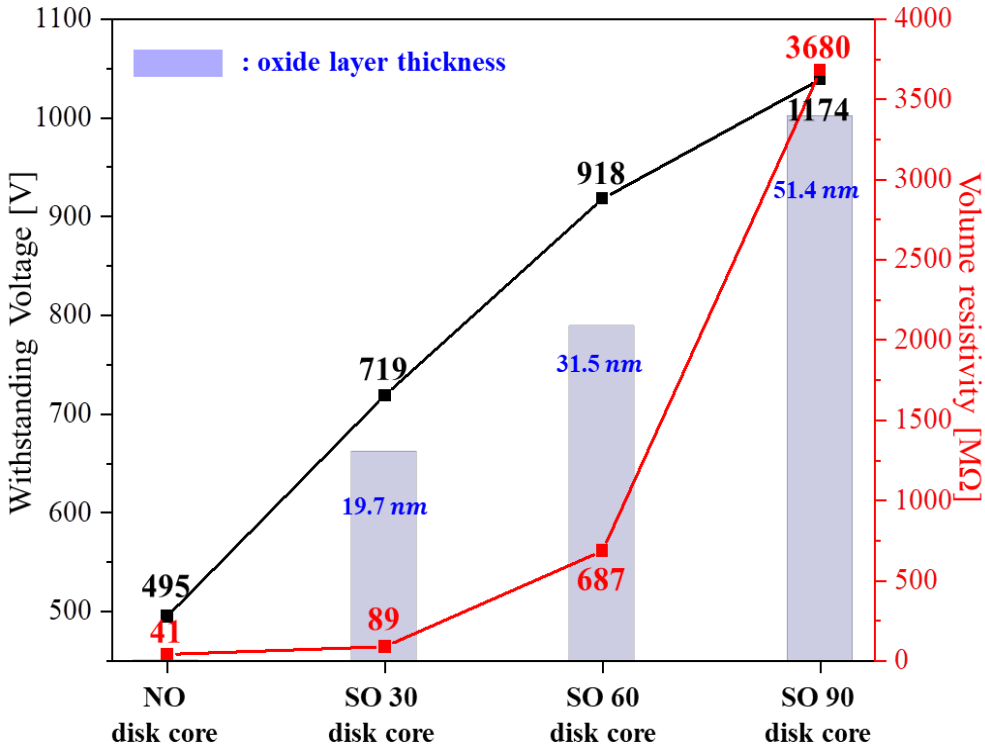

Figure 4.17. Withstanding voltage of the NO, SO30, SO60, and SO90 disk samples, which values are represented in black line. The oxide layer thickness of the powder samples were represented together in blue.

As shown in figure 4.14, although the powders had more contact in the SO disk sample than in the NO disk sample, the insulation property of the SO disk samples remained higher. Through this, it can be confirmed that the oxide layers were formed uniformly throughout the powder surface by the selective oxidation and had an excellent insulation property.

Hsiang et al. [47] reported that a Cr-rich insulating oxide layer could be formed on the 82.39Fe-13.08Si-4.52Cr (wt%) powder surface by the oxidation rate control in the annealing process using an yttrium nitrate. For the core fabrication, the powders were mixed with the yttrium nitrate and they were press molded by a uniaxial pressing. After that, toroidal cores were fabricated by annealing the press molding samples and the Cr-rich oxide layer was formed on the powders during the annealing. No binding material such as resin was used for fabricating the core, and when the Cr-rich oxide layer with the thickness of 40 nm was formed on the powder surface, the specific resistivity of the toroidal core was about 2.0×10^7 Ω · cm. In this study, the specific resistivity of the SO90 toroidal core was 1.57×10^{10} Ω · cm. After the selective oxidation annealing for 90 min, the SiO_2 and Cr_2O_3 double oxide layer with the thickness of 51.2 nm was formed on the powder surface. In addition, the phenolic resin, a kind of organic insulation coating material, was used for press molding. Therefore, it seems that the specific resistivity of the toroidal core samples prepared in this study was higher than that of previous study.

4.8 Magnetic property of SMC core: Inductance (L), Permeability (μ), Quality factor (Q)

An inductor is a component that converts an electrical energy into a magnetic energy and stores it in the form of a magnetic field. The performance of the inductor can be evaluated by the inductance (L) representing the efficiency for storing magnetic energy and by the quality factor (Q) corresponding to the ratio of stored energy over lost energy. These magnetic properties were assessed for the prepared toroidal core samples, in an attempt to evidence the excellent potential of the selective oxidation of SMCs to prepare superior materials for inductors.

The L values of the NO, SO30, SO60, and SO90 toroidal core samples were measured in the frequency range from 0.01 to 100 MHz using an impedance analyzer and the results are shown in Figure 4.18. In the all samples, the L values were kept constant up to 10 MHz. Comparing the L values at 1~3 MHz, which frequencies are mainly used for portable devices [48], L values of the NO, SO30, SO60, and SO90 toroidal core were 2.40, 2.48, 2.54, and 2.60 μH, respectively.

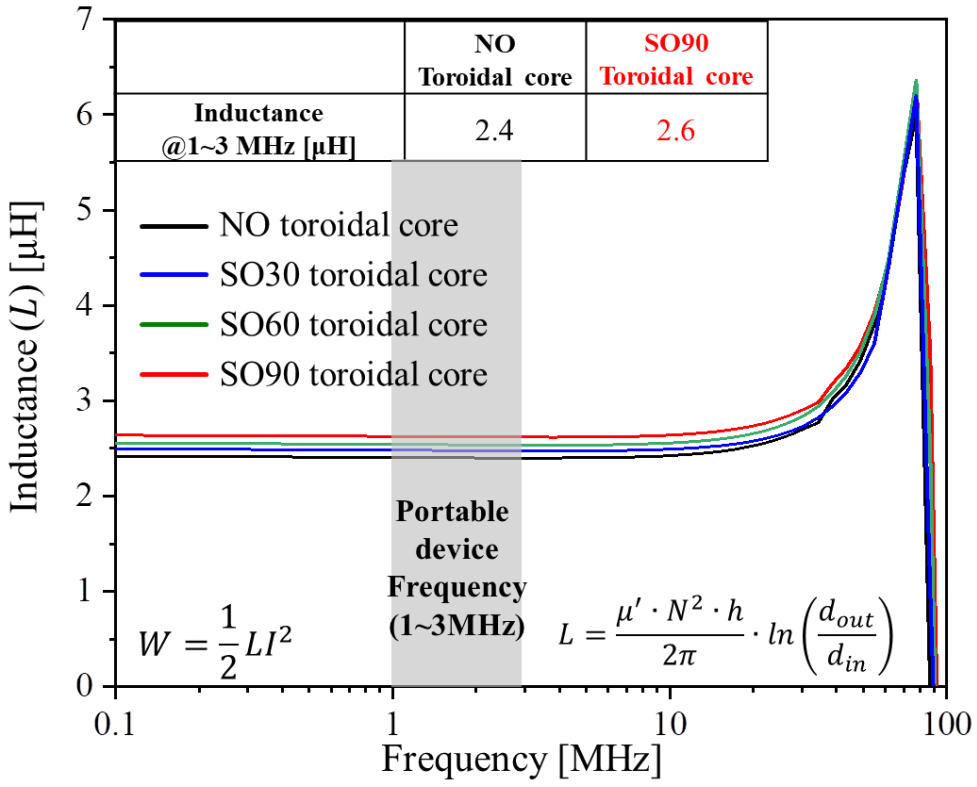

Figure 4.18. Inductance (*L*) values of the NO, SO30, SO60, and SO90 toroidal core samples.

Through these results, it was confirmed that the efficiency for storing magnetic energy of the core could be improved by the formation of the insulation layer on the powder surface by the selective oxidation annealing.

As soft magnetic materials are normally used in a high frequency alternating magnetic field, the phase delay phenomenon occurs: the magnetic phase induced in the material is delayed compared to the external magnetic field, which results in the energy loss. Due to this phase delay phenomenon, the magnetic permeability is divided into a real (μ') and an imaginary (μ'') permeability term as shown in Eq. (14) [49−51].

$$\mu = \mu' - i\mu'' \quad (14)$$

The μ' indicates the stored energy when applying the magnetic field and the μ'' indicates the amount of energy loss. The μ' value can be calculated from the L value using the following Eq. (15):

$$L = \frac{\mu' \cdot \mu_0 \cdot N^2 \cdot h}{2\pi} \cdot ln\left(\frac{d_{out}}{d_{in}}\right) \quad (15)$$

where L is the inductance of toroidal core, μ_0 is the permeability of vacuum ($4\pi \times 10^{-7}$ H/m), N is the winding turns of wire, h is the height of toroidal core, and d_{out} and d_{in} is the outer and inner diameter of toroidal core, respectively. The L, which represents the amount of the stored energy, improves with increasing the μ' and the N. However, when the N is increased, the amount of heat generated in the core is increased, so the development in the direction of increasing the μ' of the core is required.

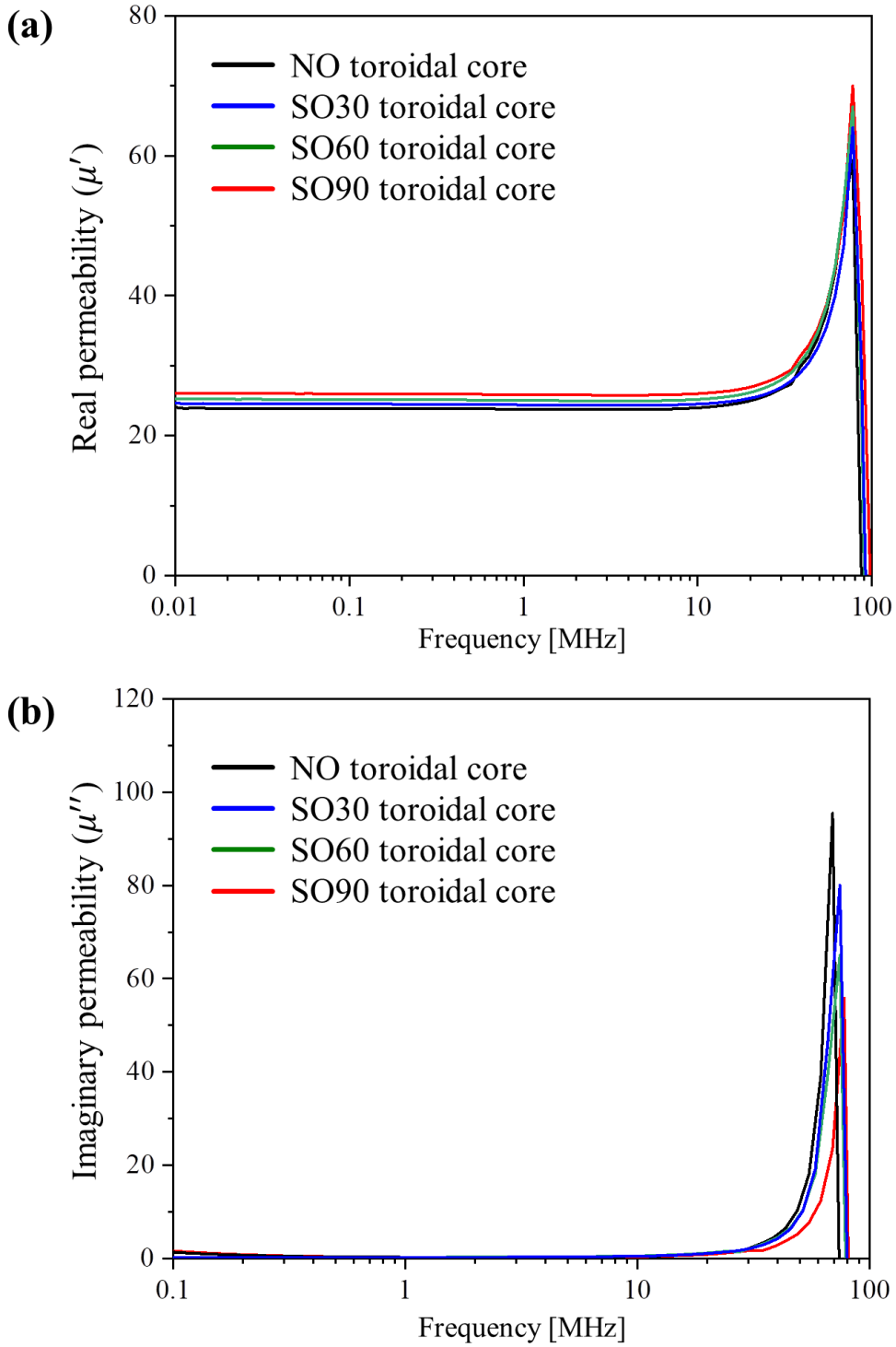

Figure 4.19.(a) Real and (b) imaginary permeability of the NO, SO30, SO60, and SO90 toroidal core samples.

Figure 4.19(a) represents the μ' of the NO, SO30, SO60, and SO90 toroidal core samples. The μ' of the all samples maintained a constant value up to a frequency of 10 MHz and the μ' values of the toroidal cores fabricated by the selectively oxidized powders were higher than that of the NO toroidal core. The μ' were increased with increasing the selective oxidation annealing time. The μ' values of the NO, SO30, SO60, and SO90 toroidal cores in the frequency range from 1 to 3 MHz were 23.8, 24.4, 25.0 and 25.9, respectively.

The μ' value of magnetic cores is affected by the Bs of magnetic powders, and it is increased with increasing the Bs value [47]. As shown in the XPS (Fig. 5) and VSM (Fig. 7) results, the Fe-based oxide layer was formed on the powder surface after the air atmosphere annealing, which resulted in the decrease of the Bs value. However, after the selective oxidation annealing, Fe with an excellent magnetic properties was reduced, and only Si and Cr were selectively oxidized, so that the B_s values of the selectively oxidized powders were rather improved than the initial powder. Therefore, by adopting the selective oxidation annealing, it is possible to improve the magnetic properties as well as the insulating properties of the core at the same time

Generally, to insulate individual powders in the SMC, the powders are coated by insulating materials such as phosphate, SiO_2, and Al_2O_3 through a wet chemical process. In this case, as the fraction of non-magnetic insulating materials increases, the μ' value decreases [52]. In the microstructure of the NO the toroidal core (Figure 4.14(a)), since the outer surface of the NO powder was coated by phosphate and SiO_2 for the insulation, a lot of space remained between the powders after press molding and curing. On the other hand, in the microstructure of the SO90 toroidal core (Figure 4.14(b)), since the powders were only mixed with the binder without the wet insulation coating, the packing density of the powders was relatively high, which resulted in the improvement of the μ' value.

Figure 4.19(b) shows the μ'' of the NO, SO30, SO60, and SO90 toroidal core samples. The resonance frequency is the frequency at which the imaginary permeability has a maximum value. The resonance frequencies of the NO, SO30, NO60, and SO90 toroidal cores were 69.0, 73.9, 74.4, and 77.6 MHz, respectively. The resonance frequency increases as the insulation property is improved, and has the same tendency with the specific resistivity [53]. By the selective oxidation annealing, the insulating oxide layer was formed on the powder surface and it is thickened with increasing the annealing time. Therefore, the resonance frequency was increased with increasing the selective oxidation annealing time.

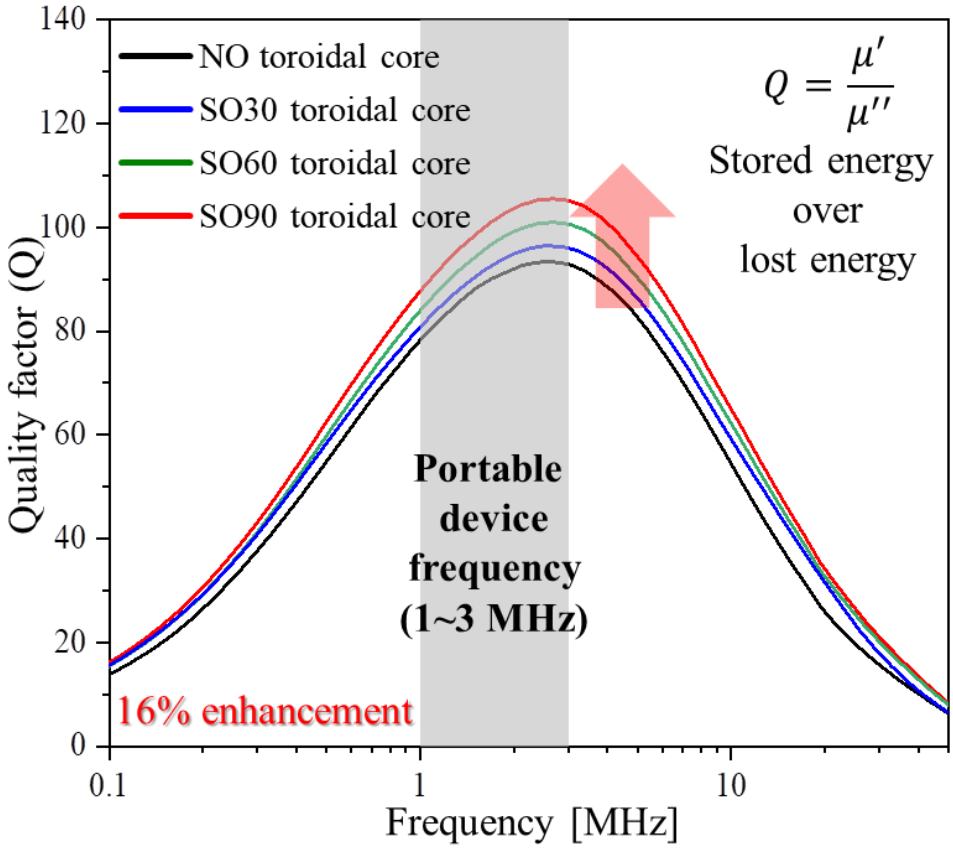

Figure 4.20. Quality factor (Q) values of the NO, SO30, SO60, and SO90 toroidal core samples.

The improvement of magnetic properties by the selective oxidation was also confirmed in the quality factor measurement result. Figure 4.20 represents Quality factor (Q) values of the NO, SO30, SO60, and SO90 toroidal core samples.

The Q, which indicates the amount of the stored energy relative to the lost energy, is expressed as the ratio of the μ' and the μ'' as following Eq. (16).

$$Q = \frac{\mu'}{\mu''} \quad (16)$$

The maximum Q values of the NO, SO30, SO60, and SO90 toroidal core samples were 94.0, 96.5, 101.0, and 105.5 respectively. Chen et al. [5] investigated magnetic properties of Fe−3.5Si−4.5Cr (in wt%) SMC coated with phosphate and sodium silicate, and they obtained the Q value of 93.4, which value is quite similar to the Q value of the NO toroidal core sample in this study. However, the Q values of cores insulated by the selective oxidation were higher than that of the NO core, notably for the SO90 core sample which yielded as high as 105.5 due to the Fe reduction and the formation of a dense insulating layer [54]. The Q value of the SO90 toroidal core was improved about 16% in the commercial frequency range compared to the NO toroidal core.

4.9 Core loss (W_t) separation calculated by variable separation method

The core loss (W_t) of magnetic components in an alternating magnetic field environment is composed of hysteresis, eddy current and anomalous loss [55−58]. Figure 4.21 is the result showing the core loss of NO, SO30, SO60 and SO90 toroidal core from 10 to 100 KHz at 50mT. And each loss can be calculated from the core loss data.

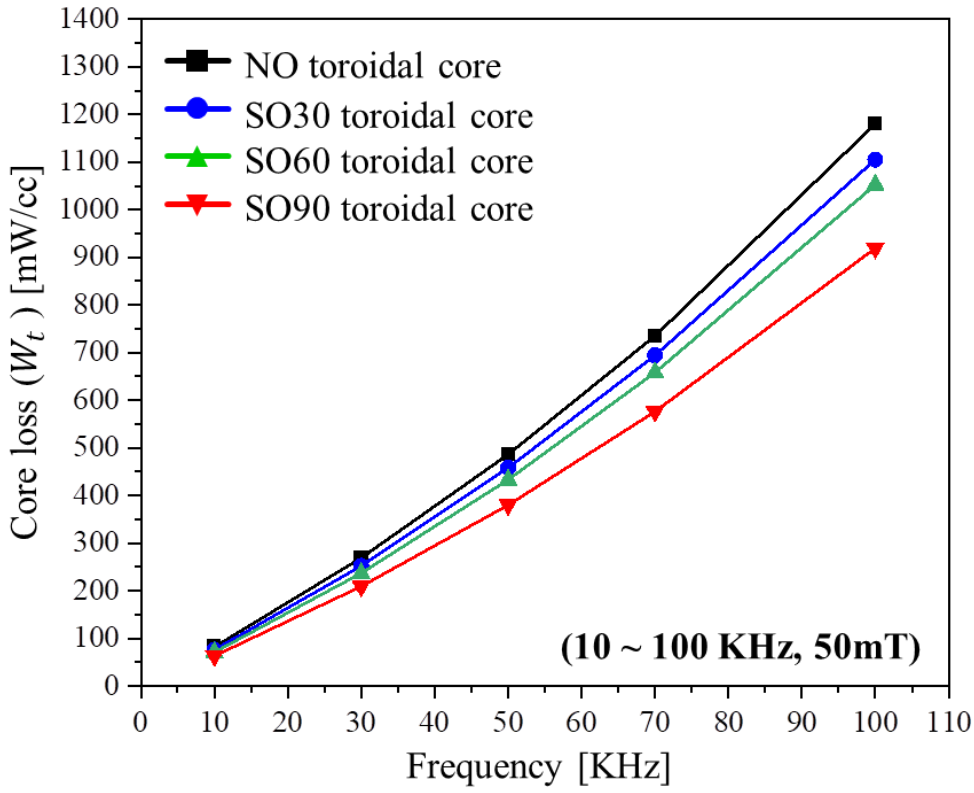

Figure 4.21. The core loss of NO, SO30, SO60 and SO90 toroidal core from 10 to 100 KHz at 50mT.

Compared with the NO toroidal core in the measured iron loss data, the SO toroidal core showed a tendency to decrease with respect to frequency. And as the selective oxidation heat treatment time increased, the core loss also showed a tendency to decrease. As mentioned above, the loss mechanisms acting on the SMC core under an alternating magnetic field environment are commonly separated to hysteresis, eddy current, and anomaly losses. It is possible to separate hysteresis loss, eddy current loss, and anomalous loss from the measured core loss data through the variable separation method. Core loss can be expressed in terms of frequency and can be expressed as follows [59-61]:

$$W_t = k_{\hat{h}} B_m^2 f + k_e B_m^2 f^2 + k_a B_m^{3/2} f^{3/2} \quad (17)$$

where W_t is the core loss of the toroidal cores, and $k_{\hat{h}}, k_e, k_a$ are the hysteresis loss coefficient, classical eddy-current loss coefficient and anomalous loss coefficient respectively. If both sides of the above equation are divided into frequencies, it can be arranged as follows.

$$W_t/f = k_{\hat{h}} B_m^2 + k_e B_m^2 f + k_a B_m^{3/2} f^{1/2} \quad (18)$$

Let, $W_t/f = y$, $f^{1/2} = x$, Eq. 18 can be rearranged as a quadratic expression for x as follows.

$$y = k_{\hat{h}} B_m^2 + k_e B_m^2 x^2 + k_a B_m^{3/2} x \quad (19)$$

The hysteresis loss can be calculated from the constant term of the quadratic expression, and the eddy current loss can be calculated from the coefficient of the highest order term of the quadratic expression.

Figure 4.22 represents the results expressed in a quadratic expression through the variable separation method from the core loss data of NO, SO30, SO60 and SO90 toroidal cores. From the quadratic equation calculated in Figure 4.22, hysteresis loss and eddy current loss can be calculated, respectively.

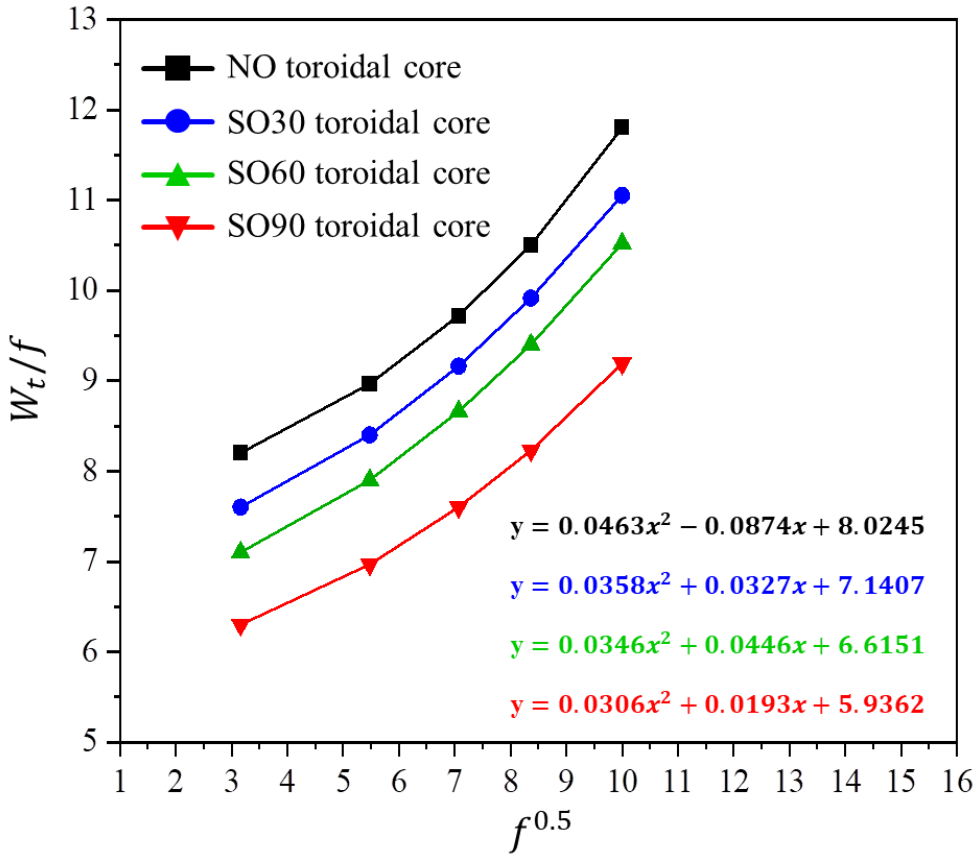

Figure 4.22. quadratic expressions through the variable separation method from the core loss data of NO, SO30, SO60 and SO90 toroidal cores.

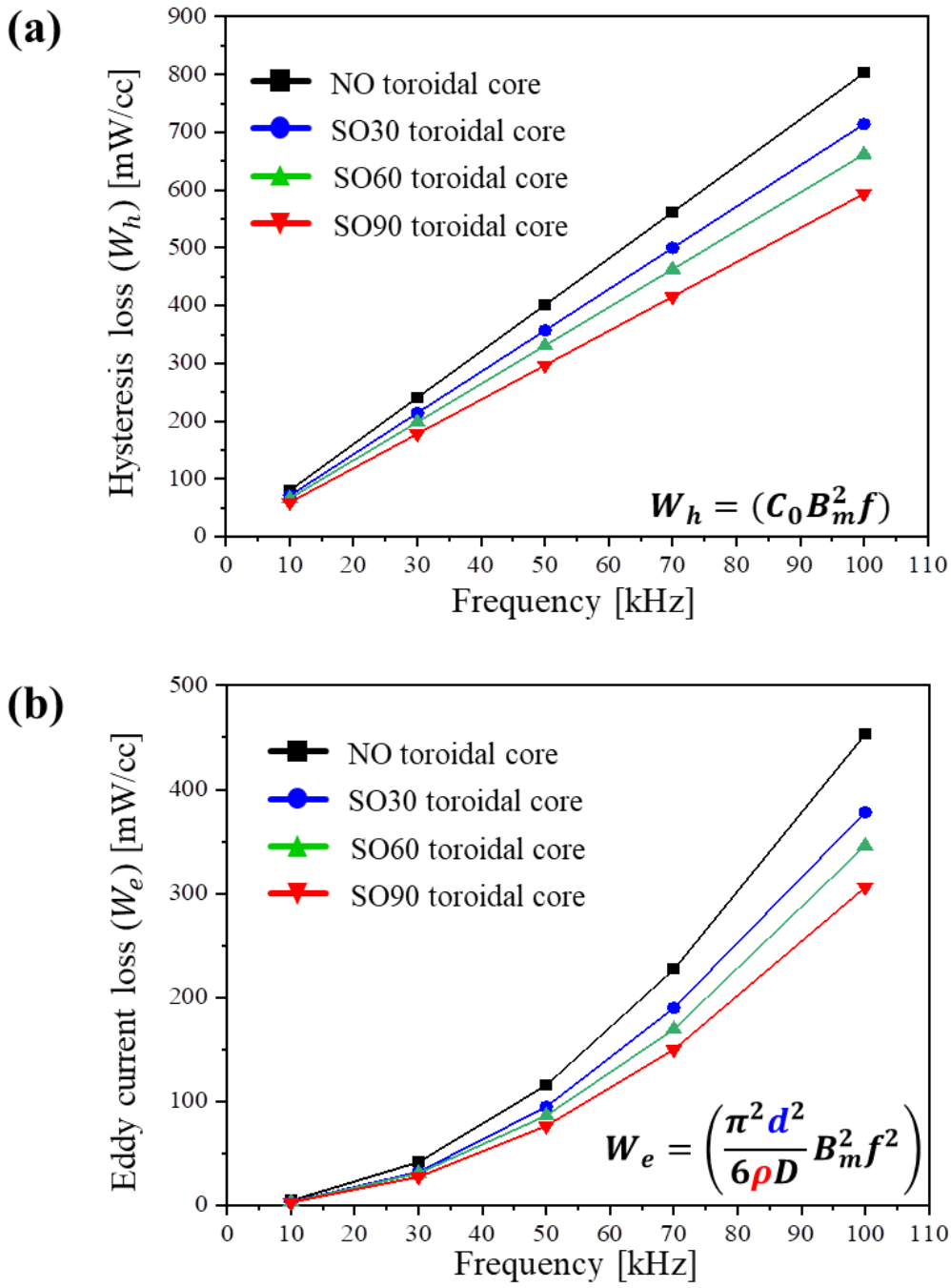

Figure 4.23. (a) Hysteresis loss calculated by variable separation method from core loss data and (b) eddy current loss calculated from core loss data

Figure 4.23(a), (b) is the result of separating hysteresis loss and eddy current loss from core loss data through variable separation method, respectively. The hysteresis loss (W_h) was calculated to have a linear shape proportional to the frequency, and the eddy current loss (W_e) was calculated as a graph that increased in proportion to the square of the frequency. Each losses showed a tendency to decrease as the selective oxidation heat treatment time increased. The reason for the decrease in hysteresis loss was that as the selective oxidation heat treatment time increases, the magnitude of the coercive force decreases and the area of the hysteresis curve decreases as shown in Figure 4.12 [62]. The reason that the eddy current loss decreased as the selective oxidation heat treatment time increased could be interpreted that the effective particle size of the powder decreased due to the formation of a uniform and dense insulating oxide layer on the surface of the powder [63]. This can be confirmed through the result of TEM analysis (Figure 4.9).

Since the eddy current loss occupies dominantly in the high frequency region [64], reducing the eddy current loss is effective to improve the overall energy efficiency. Eddy current loss is reduced with increasing the resistivity and decreasing the effective size of the powder [65, 66]. Since the resistivity is a factor determined by the composition of the powder, the insulation technology for reducing the effective powder size is very important for the inductor component. In this study, it was confirmed that a dense and uniform insulation oxide layer could be formed on the selectively oxidized powder surface. From this, the insulation property of the powders was improved, which would reduce the eddy current loss of the core. Accordingly, the L and Q values indicating the efficiency for storing magnetic energy was improved by adopting the selective oxidation annealing.

4.10. High temperature properties of SMC core: NO powder & SO90 powder

The mass-produced inductor core was manufactured with NO powder and SO90 powder. In the case of NO powder, an insulating layer was formed on the surface of the powder by applying the wet chemical process (phosphate + liquid sodium silicate). In consideration of the actual use environment of the inductor core, a high temperature property evaluation experiment was conducted in which the inductor core was exposed at a high temperature for 1000 hr. To form the experiment condition similar to the engine room of an electric vehicle, which is the actual operating environment of the inductor core, the furnace temperature was set to 105 ℃. And a DC current of 8.0A was applied to the surface of the inductor core, so the surface temperature was set at 180 ℃ for 1000 hours. The experiment was carried out by exposing it to an atmospheric environment. The quality factor (Q) of the inductor core before and after the 1000 hr high temperature evaluation test was compared. And based on this, the evaluation of high temperature characteristics of inductor cores manufactured with each powder was compared.

Figure 4.24(a) represents the difference in quality factor before and after high temperature thermal load evaluation of inductor core fabricated by NO powder. It was measured that when the inductor core fabricated by NO powder was exposed for 1000 hours at 180 ℃ atmospheric oxidation condition, the quality factor was deteriorated in all frequency range. This could be interpreted as the fact that the real part of permeability deteriorated due to atmospheric oxidation at high temperature through the powder surface where the insulating layer was not formed because a non-uniform insulating layer was formed on the surface of the powder.

Figure 4.24(b) represents the difference in quality factor before and after high temperature thermal load evaluation of inductor core fabricated by SO90 powder. When the inductor core made of SO90 powder was exposed for 1000 hours at 180 ℃ atmospheric oxidation condition, it was measured that the quality factor (Q) was maintained or the quality factor increased in the commercial frequency range of 1−3 MHz. This is because a uniform and dense SiO_2, Cr_2O_3 insulating layer was formed on the surface of the powder. Therefore, it is considered that applying the selective oxidation annealing process is more advantageous than applying the conventional wet chemical process considering the environment exposed to high temperature for a long time.

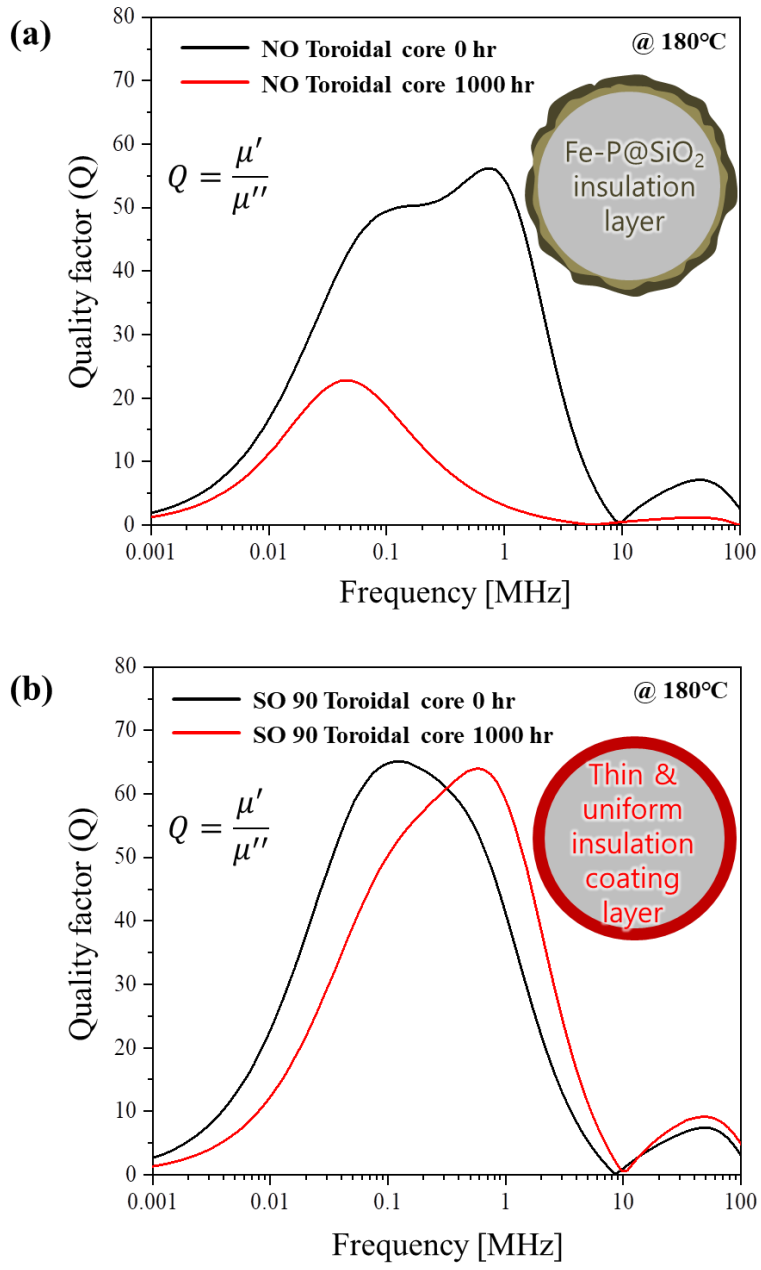

Figure 4.24.(a) represents the difference in quality factor before and after high temperature thermal load evaluation of inductor core fabricated by NO powder. (b) represents the difference in quality factor before and after high temperature thermal load evaluation of inductor core fabricated by SO90 powder.

Chapter 5. Surface modification of Fe-Si-Cr alloy by selective oxidation annealing and its corrosion properties

5.1. Introduction

Inductors, as one of the passive components, have been improved to accommodate the requirements of portable devices, home appliances, and so on. Especially, development of electric vehicles has boost innovation of these electric components in terms of high reliability, multi-functionality, and miniaturization [67-70]. Similar with capacitors which store electrical energy with a form of electric field, inductors store magnetic energy with a form of magnetic field.

Figure 5.1 is an AEC-Q200 document that defines evaluation items of inductor cores in consideration of the actual use environment by the Automotive Electronics Council. As seen in AEC-Q200 document, it is also essential to evaluate passive devices such as inductors in consideration of the actual environment. It is also important to examine the corrosion properties in an actual high-temperature, high-humidity environment, as in evaluating the quality factor of an inductor by applying a thermal load for 1000hr at high temperature.

TABLE 5 – TABLE OF METHODS REFERENCED MAGNETICS (INDUCTORS/TRANSFORMERS)			
Stress	**NO.**	**Reference**	**Additional Requirements**
Pre-and Post-Stress Electrical Test	1	User Spec.	Test is performed except as specified in the applicable stress reference and the additional requirements in Table 5.
High Temperature Exposure (Storage)	3	MIL-STD-202 Method 108	1000hrs. at rated operating temperature (e.g. 125℃ part can be stored for 1000hrs. @ 125℃. Same applies for 105℃ and 85℃. Unpowered. Measurement at 24±4 hours after test conclusion)
Biased Humidity	7	MIL-STD-202 Method 103	1000hours 85℃/85%RH. Unpowered. Measurement at 24±4 hours after test conclusions

Figure 5.1. AEC-Q200 document that defines evaluation items of inductor cores in consideration of the actual use environment by the Automotive Electronics Council.

Since SiO_2 and Cr_2O_3 insulating layers were formed on the surface of the powder by applying the selective oxidation annealing to the Fe-Si-Cr powder, an experiment was conducted to confirm the corrosion characteristics under the actual operating environment. It is known that SiO_2 or Cr_2O_3 layer could be a barrier layer against corrosion [71-73]. Passive components, especially for automotive industry require not only high performance but high reliability based on AEC-Q200 standard including moisture resistance and high temperature exposure [74, 75]. Thus, more careful manipulation on an insulation layer in terms of thickness has been made to achieve anti-corrosion performance.

In this study, selective oxidation heat treatment was applied as a new insulation coating method, where an insulating layer was manipulated in terms of thickness by varying the heat treatment time. Gaseous reaction would have benefits in forming oxide layer in terms of conformal and compacted characteristics so the oxide layer formed by the heat treatment could also function as barrier layer against corrosion. Therefore, corrosion properties were evaluated to find out the insulating oxide layer could exert protective characteristic against corrosion.

5.2. Preparation for electrochemical analysis (corrosion properties)

Water-atomized Fe-3Si-5.5Cr (in wt%) powder with the average size of 10.3 μm was used. Since the electrochemical tests for analyzing corrosion properties cannot perform in the powder state, the powder was melted to an ingot by arc melting method. After melting, the ingot was turned into solid plates with the size of 20 mm (length) × 12 mm (width) × 2 mm (thickness). The chemical composition of the initial powder and arc-melted ingot was observed by using a field emission-scanning electron microscope (FE-SEM) (QUANTA FEG 250, FEI) equipped with energy dispersive X-ray spectroscopy (EDS). The result was shown in Figure 5.2.

Wt %	Powder	Arc-melted ingot
Fe	91.62	91.56
Si	2.74	2.70
Cr	5.64	5.74

Figure 5.2. Chemical composition of initial powder and Arc-melted ingot

There was no significant chemical composition difference between the initial powder and the solid plate samples. Prior to selective oxidation heat treatment, the sample was grinded with up to #4000 with SiC abrasive paper. After that the sample was cleaned with ethanol and acetone, followed by ultrasonic cleaning in ethanol.

5.3. Experimental procedure

The thermodynamic equation for the selective oxidation annealing process design was calculated with reference to Sections 2.2 ~ 2.4. A heat treatment furnace equipped with a thermostat bath was used for selective oxidative heat treatment [46]. Partial pressure ratio of hydrogen gas and water vapor ($p_{H_2(g)}/p_{H_2O(g)}$) was controlled by flowing hydrogen gas into the thermostat bath containing deionized water (D.I water), where desired water vapor pressure was achieved by setting the bath ' s temperature. The water temperature of the thermostat bath was set to 20 ℃, and when calculating the $p_{H_2(g)}/p_{H_2O(g)}$ ratio, it was determined to 41.8.

The H_2−H_2O mixed gas was flowed into the furnace with the flow rate of 2 slm. Selective oxidation heat treatment was carried out at 650 ℃ for 30, 60, and 90 min. The oxidation and reduction reactions of metals become easier to control as the heat treatment temperature increases. However, the higher the reaction temperature, the faster the oxidation reaction rate becomes, making it difficult to control the thickness of the oxide layer. In previous studies of FeSiCr composition, oxidation proceeded rapidly at 700 ℃ heat treatment temperature condition [30].

Therefore, the heat treatment temperature in this study was set to 650 ℃. In this study, the initial plate sample without selective oxidation heat treatment is referred to as S.O.(selective oxidation) 0 min, and the plate samples subjected to selective oxidation heat treatment for 30, 60, and 90 min are referred to as S.O. 30 min, S.O. 60 min, and S.O. 90 min, respectively. In the heating and cooling stages, only dry hydrogen gas was injected 2 standard liter per minute (slm) into the furnace to prevent further oxidation.

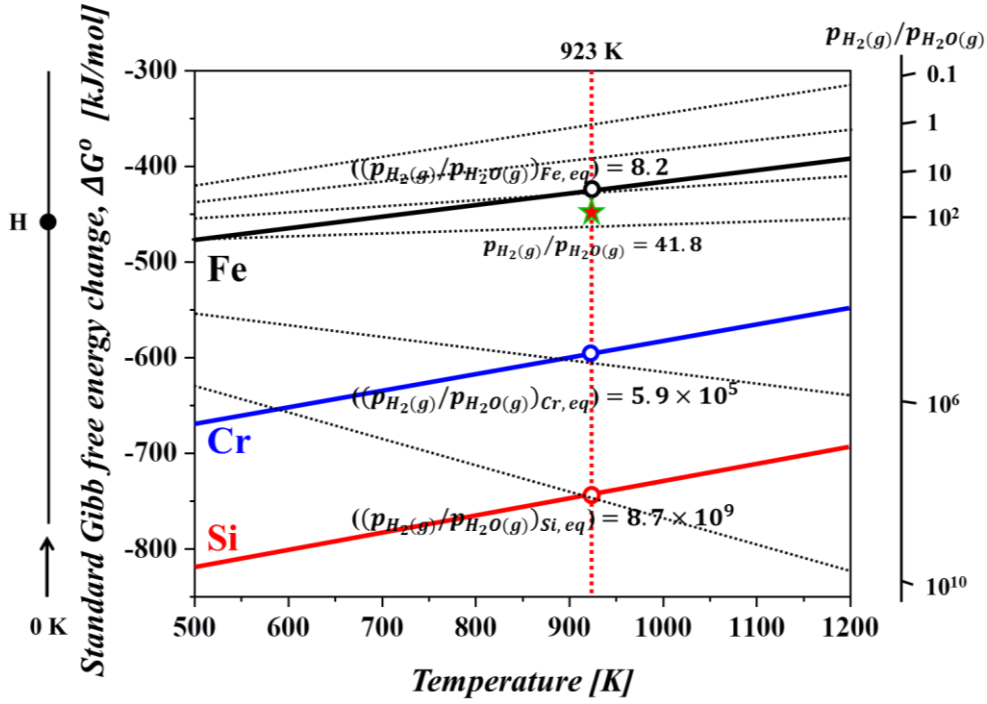

Figure 5.3. Ellingham diagram for oxidation of Fe, Cr, and Si represented with $p_{H_2(g)}/p_{H_2O(g)}$.at 650 ℃

The selective oxidation could be achieved by controlling $p_{H_2(g)}/p_{H_2O(g)}$ and temperature based on oxidation driving force of elements. To derive adequate conditions to only oxidize Cr and Si, oxidation driving forces of Fe, Si, and Cr were calculated by Thermo-Calc software, as shown in Figure 5.3, Among the elements in the Fe-Si-Cr alloy, Si showed the highest oxidation driving force, followed by Cr and Fe. By using the difference in the oxidation driving force of each element, the selective oxidation condition could be obtained by controlling $p_{H_2(g)}/p_{H_2O(g)}$.

When the $p_{H_2(g)}/p_{H_2O(g)}$ value is between the $\left(p_{H_2(g)}/p_{H_2O(g)}\right)_{eq}$ values of Fe and Cr at a given temperature, only oxidation of Cr and Si occurs, while Fe is reduced. The dotted lines on the Ellingham diagram represented the partial pressure ratio values ($p_{H_2(g)}/p_{H_2O(g)}$) denoting 0.1, 1, 10, 10^2, 10^6, 10^{10}. The ΔG^0 of each element were obtained from the Thermo-Calc software and their values for Fe, Si, and Cr at 650 ℃ were −426.2, −744.2, and −597.5 kJ/mol, respectively. From Eq. (8), $\left(p_{H_2(g)}/p_{H_2O(g)}\right)_{eq}$ values of Fe, Si, and Cr were calculated as 8.2, 8.7×10^9, and 5.9×10^5, respectively. Therefore, the $p_{H_2(g)}/p_{H_2O(g)}$ value should be controlled between 8.2 and 5.9×10^5 for the selective oxidation of Si and Cr.

5.3.1 Characterization

Conditions for selective oxidation heat treatment were calculated by Thermo-Calc software, using a condensed compound database of SSUB5. The surface of the samples was analyzed by X-ray photoelectron spectroscopy (XPS) (K-Alpha, ThermoFisher). The microstructure of the oxide layers on the powder surface was investigated by transmission electron microscope (TEM) (Titan G2 ChemiSTEM Cs Probe, FEI) equipped with energy dispersive X-ray spectrometry (EDS). The TEM specimens were prepared by a focused ion beam (FIB, Versa 3D, FEI). Electrochemical tests (Metrohm Autolab, Autolab PGSTAT302N) such as potentiodynamic polarization and electrochemical impedance spectroscopy (EIS) were conducted with three electrodes configuration cell, where Pt plate and Ag/AgCl electrodes were used as counter and reference electrodes. 3.5 wt % NaCl solution was used as an electrolyte. Polarization curves were obtained with a scan rate of 0.05 mV·s−1 in the range between −1.5 and +1.5 V from open circuit potential (OCP). EIS tests were performed at OCP with the AC amplitude of 10 mV over the frequency range from 10000 to 0.05Hz.

5.4. Surface modification of arc-melted samples by selective oxidation heat treatment

Evolutions of the oxide layer with the selective oxidation heat treatment were analyzed in terms of morphology and composition, as shown in Figure 5.4.

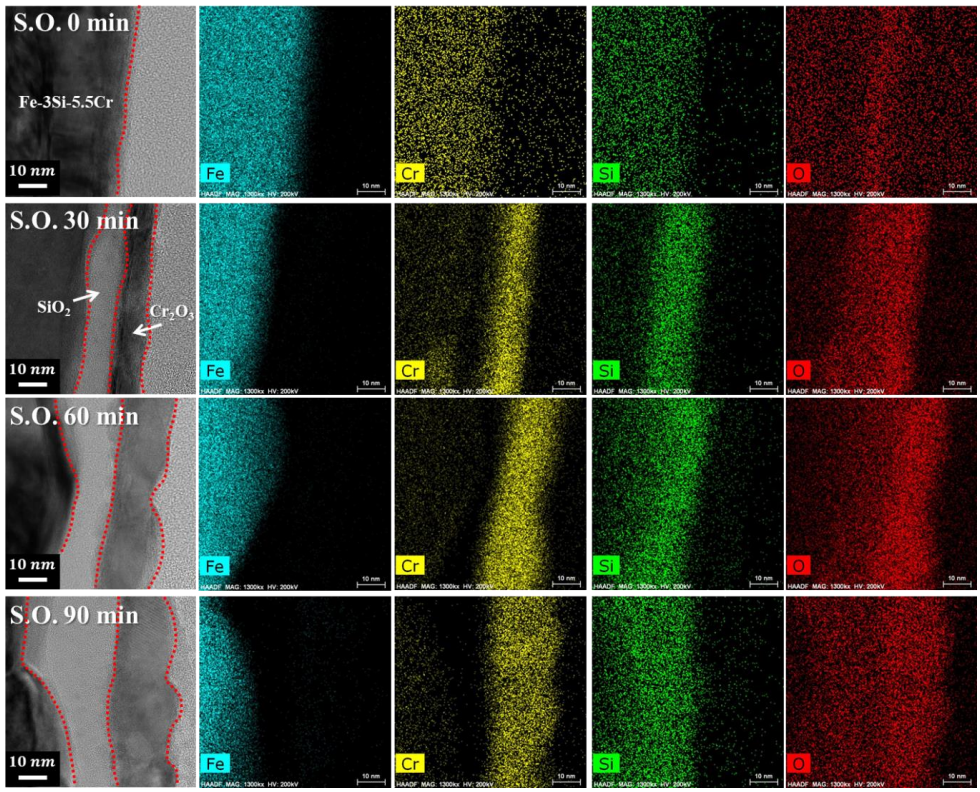

Figure 5.4. Morphology and composition mapping results of the S.O 0 min, S.O. 30 min, S.O. 60 min, and S.O. 90 min samples analyzed by TEM.

Interestingly, the selective oxidation heat treatment resulted in two-layered oxide layer. While no detectable oxide layer existed for the S.O. 0 min sample, the thickness of oxide layer increased with the heat treatment time and the resultants of thickness were 22.7, 33.8, 44.3 nm after selective oxidation heat treatment for 30, 60 and 90 min. Each layer seemed to equally contribute to the growth of the oxide layer. Compositional analysis revealed that the outer layer had a composition of 1Fe-39Cr-1Si-59O (in at%), and the inner layer was analyzed to have a composition of 34Si-66O (in at%), indicating that the outer and inner oxide layers were Cr_2O_3 and SiO_2, respectively.

In the previous study, Park et al.[46] reported the changes in the surface oxide layer of Fe–3Si–5.5Cr powders according to the oxidation potential. As same with this study, in the condition with the $p_{H_2(g)}/p_{H_2O(g)}$ the ratio of 41.8, Si and Cr were selectively oxidized, resulting in the formation of Si and Cr oxide layer on the surface. While, when the powders were annealed in the air atmosphere, all of Fe, Si, and Cr were oxidized, and the oxide layer mainly composed of Fe was formed on the surface. In the TEM results, Cr and Si oxide layers were formed on the surface of the samples after the selective oxidation. Therefore, it is judged that the selective oxidation condition was formed during the heat treatment process.

It was reported that a two-layered oxide structure was commonly formed when the Fe–Si–Cr ternary alloy was oxidized.[76, 77] The Cr has a higher diffusion coefficient than Si in Fe, Cr atoms first rapidly move to the surface to form an external Cr oxide layer during the oxidation [78]. Then, when the oxidation proceeds, the oxidation potential inside the Cr oxide layer is lowered. At this time, an atmosphere in which only Si with the highest oxidation driving force is oxidized is formed, and a Si oxide layer is formed therein, which results in the two-layered oxide structure [79].

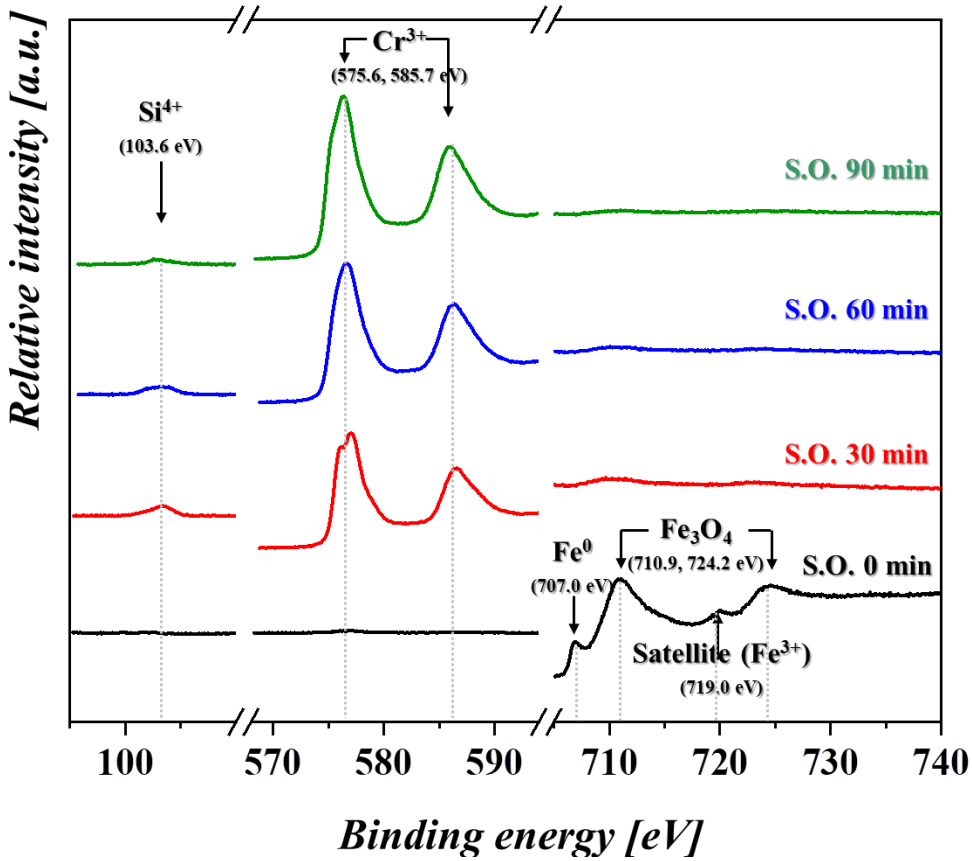

Figure 5.5. XPS spectra of the S.O. 0 min, S.O. 30 min, S.O. 60 min, and S.O. 90 min samples.

As shown in Figure 5.5, XPS results showed compositional change of the oxide layers with the selective oxidation heat treatment. In the XPS spectrum of the S.O. 0 min sample, there were only Fe^0 peak (metallic Fe) at 707.0 eV and Fe ion peaks at 710.9 eV and 724.2 eV, which corresponds to Fe 2p 3/2 and Fe 2p 1/2 [80]. Also, a satellite peak corresponding to Fe^{3+} was detected at 719.0 eV [81]. No peak is detected in Cr and Si region. These results indicate that the S.O. 0 min sample was just covered with thin Fe oxide.

On the other hand, after the selective oxidation heat treatment, Cr and Si peaks associated with the oxidation of Cr and Si appeared, while the Fe peaks were diminished and these trends became predominant with the heat treatment time. The peak in Si region was detected at 103.6 eV, which was attributed to Si^{4+} oxidation state (Si 2p3/2) [82]. In Cr region, peaks with binding energies of 575.6 eV and 585.7 eV, corresponding Cr^{3+} oxidation state (Cr 2p3/2 and Cr 2p1/2) [83], appeared after the selective oxidation heat treatment. From these results, it can be inferred that the Si and Cr oxide layers were successfully formed by the selective oxidation heat treatment. The heat treatment also caused the disappearance of the Fe^0 peak at 707.0 eV, which would be ascribed to the thickened oxide layer. Moreover, with increasing the heat treatment time, the peak intensity of Si^{4+} weakened due to the thickened Cr_2O_3 layer.

5.5. Corrosion properties: Potentiodynamic polarization curves test

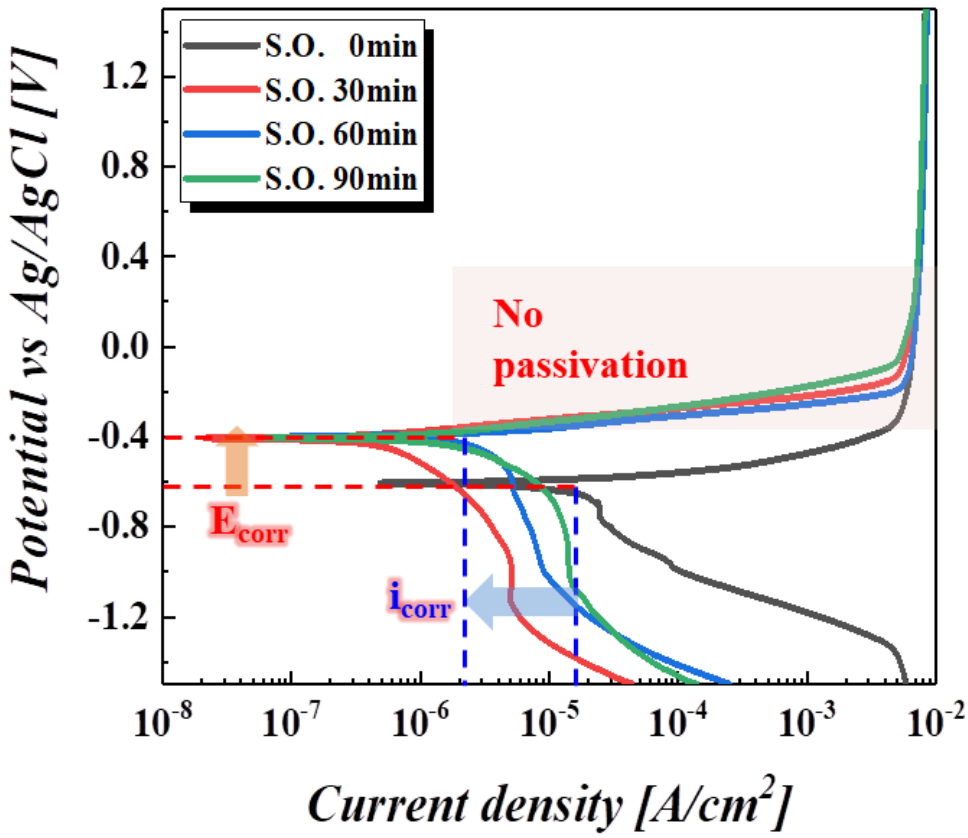

Figure 5.6. Polarization curves of the samples with and without selective oxidation heat treatment.

Materials' passivation is usually considered as an excellent tool for improving the corrosion resistance of materials. For example, stainless steels exhibit high corrosion resistant characteristics as a result of passivation which could be achieved by inherently formed chromium oxide (Cr_2O_3) film, with a few nanometers in thickness on surface of them. As shown in Figure 5.6, the modified surface by the selective oxidation resulted in cathodic shift of the corrosion potential as a result of the oxide layer formation. However, the time for the selective oxidation, which caused the increase in the thickness of the oxide layer provided little impact on the corrosion potential (E_{corr}), indicating that surface state was not changed by the heat treatment time. As denoted in Figure 5.4, the oxide layers such as SiO_2 and Cr_2O_3 were formed through the selective oxidation heat treatment, but no passivation characteristic was presented in the polarization curves. However, the pre-formed oxide layer resulted in the reduction of the corrosion current density (i_{corr}) by one order, indicating that the oxide layers formed by the selective oxidation functioned as a barrier layer to corrosion. Even though the presence of the inert layers on the Fe-Si-Cr powder could reduce i_{corr}, an additional reduction in i_{corr} did not occur with increasing the thickness of the oxide layers. Polarization parameters measured in the 3.5 wt% NaCl solution are summarized in Figure 5.7. No appearance of passivation characteristic with the oxide layer formation meant that the oxide layer was not electrochemically active, which was often observed for the low Cr content steels and some coated materials [84-88].

	S.O 0 min	S.O 30 min	S.O 60 min	S.O 90 min
E_{corr} [V]	-0.60	-0.40	-0.40	-0.40
I_{corr} [A/cm^2]	2.14×10^{-5}	9.10×10^{-7}	1.05×10^{-6}	0.94×10^{-6}

Figure 5.7. Polarization parameters measured in the 3.5 wt% NaCl solution.

5.5.1. Corrosion properties : EIS (Electrochemical Impedance spectroscopy) test

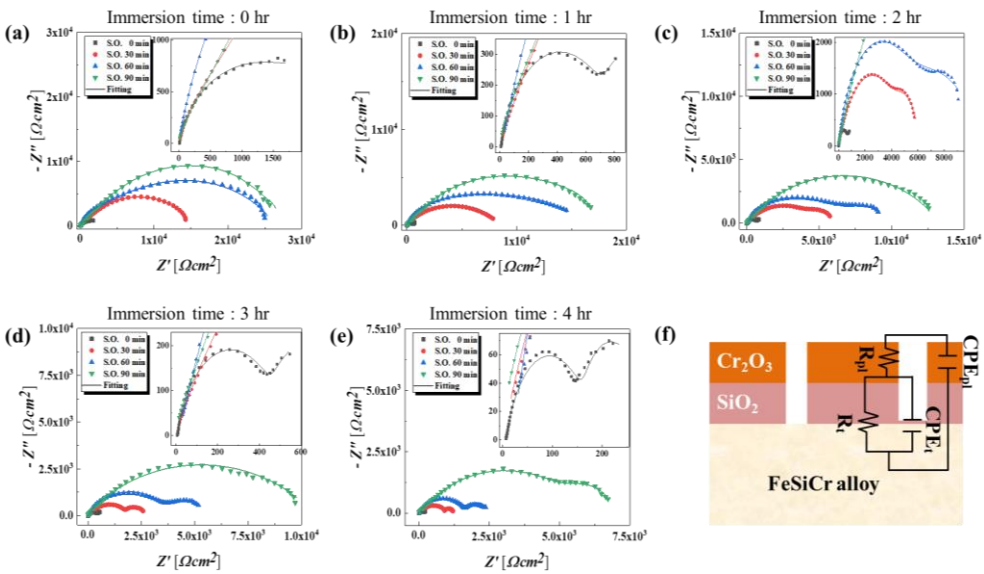

Figure 5.8. Nyquist plots of the samples immersed in the 3.5 wt% NaCl solution for (a) 0 hr,(b) 1hr, (c) 2 hr, (d) 3 hr, and (e) 4 hr. The inlets in figures are the enlarged parts Nyquist plots showing two time constants. Figure 5.8(f) shows a schematic illustrating damaged oxide layer during the immersion, where equivalent circuit used to interpret data is shown.

The barrier effect of the oxide layer was further investigated by EIS. As shown in Figure 5.8(a), the selectively oxidized samples showed the larger one loop than the untreated one and their diameter became larger with the selective oxidation time. As the diameter was directly related to corrosion resistance, it can be inferred that the selective oxidation could increase corrosion resistance of the Fe-Si-Cr alloy by forming the oxide layers. While the thickness of the oxide layers exerted little impact on the corrosion current density for the polarization test, and their contribution on the corrosion resistance was apparent; corrosion resistance became grown with the selective oxidation time as a result of the thickened thickness. However, the oxide layers such as SiO_2 and Cr_2O_3 seemed to be susceptible to the NaCl solution. With the immersion in the NaCl solution, the one loops turned into the resolved loops as well as the shrinkage in the loop diameter, which was ascribed to loss in the protective characteristic of the oxide layers [89, 90]. Titanium and titanium alloys showed the similar behavior when exposed to a highly reducing condition, where a TiO_2 layer lost its protective characteristic [91]. The appearance of the two semicircles first occurred for the S.O. 0 min sample, followed by the S.O. 30 min, S.O. 60 min, and S.O. 90 min samples, indicating that the thicker oxide layer showed more protective characteristic to corrosion. The S.O. 90 min sample having oxide layer with the thickness of 44.2 nm could withstand 3 hr immersion and showed the two semicircles after the 4 hr immersion.

As schematically shown in Figure 5.8(f), these phenomena would be ascribed to breakage of the oxide layer [92-96]. Therefore, the equivalent circuit representing porous layered structure was used to interpret the data and the fitted results were listed in Figure 5.9. R_{pl} and CPE_{pl} represented the porous oxide layer' s resistance and capacitance. R_t and CPE_t indicated charge transfer resistance and capacitance at the oxide layer/substrate interface. As well the reduction of R_{pl} related to the deterioration of the oxide layer, the decrease in R_t became dominant with the immersion time. Once the oxide layer was broken, unprotective surface started to be exposed, leading to the remarkable decrease in R_t.

		R_{pl} (Ωcm^2)	CPE_{pl} (Fcm^{-2})	R_t (Ωcm^2)	CPE_t (Fcm^{-2})
S.O. 0 min	0 hr	769.8	0.00040	1737.9	0.00325
	1 hr	442.6	0.00042	814.6	0.01643
	2 hr	378.5	0.00036	638.6	0.01447
	3 hr	280.5	0.00047	509.1	0.01971
	4 hr	104.8	0.00071	172.6	0.02564
S.O. 30 min	0 hr	1699.7	3.7×10^{-6}	13589	1.3×10^{-5}
	1 hr	1361.6	1.9×10^{-6}	8402.3	2.7×10^{-5}
	2 hr	1104.7	2.2×10^{-5}	5061.1	0.00065
	3 hr	734.2	2.0×10^{-5}	2005.9	0.00100
	4 hr	243.7	1.5×10^{-5}	995.4	0.00096
S.O. 60 min	0 hr	1820	7.4×10^{-7}	27975	1.0×10^{-5}
	1 hr	1693.1	1.1×10^{-6}	16321	2.2×10^{-5}
	2 hr	1512.4	4.1×10^{-6}	8369.9	0.00022
	3 hr	1711.6	6.2×10^{-6}	3837.7	0.00054
	4 hr	800.13	4.7×10^{-6}	1671.8	0.00087
S.O. 90 min	0 hr	1888.8	5.5×10^{-6}	25202	1.0×10^{-5}
	1 hr	1509.9	6.5×10^{-6}	16598	1.2×10^{-5}
	2 hr	984.6	6.8×10^{-6}	12320	1.4×10^{-5}
	3 hr	912.9	2.5×10^{-5}	11040	4.8×10^{-8}
	4 hr	926.2	9.7×10^{-6}	6965.2	1.0×10^{-5}

Figure 5.9. Fitted data with the equivalent circuit for resistances (R_{pl} and R_t) and capacitances (CPE_{pl} and CPE_t) of porous oxide layer and interface between oxide layer and substrate.

Chapter 6. Enhancement of the corrosion properties of selective laser melted Co-Cr-Mo alloys by selective oxidation annealing

6.1. Introduction

Cobalt-chromium-molybdenum (Co-Cr-Mo; CCM) alloy has high mechanical strength and wear resistance compared to titanium (Ti) alloys because of the precipitation of hard carbide phases [97-99]. These characteristics make it widely used as biomedical implants that take on large loads and require high abrasion resistance, like an artificial hip joint [100, 101]. However, the CCM alloy has low corrosion properties and biocompatibility compared to Ti alloys. In the CCM alloy, Co is eluted as an ion in a corrosive environment, and releasing a metal ion is toxic to cells and increases carcinogenesis risk [102-104].

Because the CCM alloy has low machinability due to its high hardness and hard carbide phases, fabricating parts using a conventional machining process is challenging [105–107]. By applying selective laser melting (SLM), a manufacturing process that selectively melts powders using a laser source, parts with complex internal structures and near–net shapes could be directly fabricated [108–111]. Therefore, research on manufacturing CCM alloy parts using the SLM process is being actively conducted.

In the SLM process, since the laser-formed melt pool rapidly cools, samples fabricated through such process have a refined microstructure and residual stress, resulting in higher mechanical properties than samples fabricated using the conventional casting method [112-115]. In addition, adopting the SLM process improves corrosion properties due to the formation of the uniform microstructure and the inhibition of the macro-segregation [116-118]. Indeed, Xin et al. [117] compared the corrosion properties of samples fabricated through SLM and the casting method and reported that the Co ion elution rate of the SLM sample was significantly lower than of the sample produced via the casting. Therefore, by applying the SLM process to the CCM alloy, there are advantages that not only the process can be simplified by direct fabrication of near-net-shape parts, but also the higher corrosion properties can be achieved.

Recently, studies on the surface treatment improving the corrosion resistance of the CCM alloy fabricated by the SLM have been conducted. Seo et al. [119] reported a study on plasma electrolytic polishing (PEP) to modify the surface properties of the selective laser melted CCM alloy. When the surface of the CCM alloy is polished through the PEP process, not only the roughness is effectively decreased, but also the corrosion resistance is improved by forming a dense Cr2O3 oxide layer on the alloy surface. In the CCM alloy, the Cr_2O_3 oxide layer acts as a barrier for dissolving Co and hinder the elution of Co ion from the alloy [102]. Therefore, the corrosion resistance can be improved if the PEP process is controlled to form a dense and thick Cr_2O_3 oxide layer on the alloy surface.

A selective oxidation annealing (SOA) technology has been developed to modify the surface oxide layer by selectively oxidizing a specific element in metallic alloys [46, 120-121]. Park et al. [121] studied changing the composition of the oxide layer of iron-silicon-chromium (Fe-Si-Cr) alloy using the difference in the oxidation driving force of Fe, Si, and Cr. In particular, the heat treatment was performed under an atmosphere in which Fe was reduced, Si and Cr were selectively oxidized, and the oxidation potential was controlled by the partial pressure ratio of hydrogen gas and water vapor. The experiments reported that SiO_2 and Cr_2O_3 oxide layers with excellent corrosion resistance were densely formed on the alloy surface, improving the corrosion resistance.

Among the elements constituting the CCM alloy, Cr has the highest oxidation driving force. If a dense and thick Cr_2O_3 oxide layer can be formed on the surface through the SOA, it is possible to improve the corrosion resistance of the CCM alloy by the simple heat treatment method. Therefore, this study thermodynamically analyzed the possibility of selective oxidation of Cr in the CCM alloy. In addition, the changes in the surface oxide layer and the corrosion properties by the SOA were examined.

6.2. Experimental procedure

The CCM alloy powders fabricated by a vacuum induction gas atomization method were used as the initial material for this study. These alloy powders had a spherical morphology; their d10, d50, and d90 values were 24.9, 39.1, and 60.8 μm, respectively. In addition, the chemical composition was examined by an inductively coupled plasma mass spectrometry (OPTIMA 7300 DV, Perkin-Elmer). The composition of the powders was 28.5Cr-6.2Mo-0.2C-0.14N, which met the composition criteria of ASTM F75 [122].

The CCM bulk samples were prepared through the SLM process using Merain Co. Ltd.' s DAVID 1.0 Metal 3D printer. The laser spot size and hatching spaces were 40 and 60 μm, respectively. The laser power and scan speed were set to 300 W and 800 mm/s, respectively, while the layer thickness was 32 μm. The SLM samples were fabricated as cube-shaped with a size of 20 × 20 × 20 mm^3. For the SOA and evaluation of the corrosion properties, they were machined to a size of 15 × 15 × 3 mm^3 by electric discharge machining. The samples' surfaces were polished with SiC paper and 3μm diamond suspension and cleaned through ethanol ultra-sonification.

Firstly, 100% H_2 gas with a flow rate of 1,000 sccm was injected into the thermostat water bath. After bubbling H_2 gas in the water, the H_2-H_2O mixed gas flowed into the heat treatment furnace. The water temperature in the thermostat bath was set to 20 ℃. From the above condition, the $p_{H_2(g)}/p_{H_2O(g)}$ ratio was calculated to 41.8.

For the SOA, the heat treatment furnace was first heated to 650 ℃, and the H_2-H_2O mixed gas flowed to the furnace for 1 hr. Then, the samples were charged into the furnace through a load lock chamber and they were annealed at 650 ℃ for 10, 20, and 30 min. Hereafter, the samples applying the SOA for 10, 20, and 30 min will be designated as SOA10, SOA20, and SOA30, respectively. The samples were loaded back into the load lock chamber after finishing the holding time, and 100% dry H_2 gas was supplied during the cooling process.

he samples' surface properties before and after the SOA were analyzed using an X-ray photoelectron spectroscopy (XPS) (K-Alpha, Thermo Fisher). The thickness and chemical composition of the surface oxide layers on the samples were examined using a transmission electron microscope (TEM) (Titan G2 ChemiSTEM Cs Probe, FEI) equipped with energy-dispersive X-ray spectroscopy (EDS). The TEM samples were prepared using a focused ion beam (FIB) (Versa 3D DualBeam, FEI).

All electrochemical tests to characterize corrosion properties were conducted with a three-electrode configuration cell, where platinum (Pt) and silver/silver chloride (Ag/AgCl) electrodes were used as counter and reference electrodes. After removing dissolved oxygen in 3.5 wt% sodium chloride (NaCl) solution by applying nitrogen (N_2) gas, open circuit potential (OCP), potentiodynamic polarization, and electrochemical impedance spectroscopy (EIS) were carried out. The polarization test was conducted with a scan rate of 0.05 mV/s from −1.5 V to 1.5 V, and the EIS test was conducted with an alternating current (AC) amplitude of 10 mV at 0.05 Hz to 10,000 Hz.

6.3. Ellingham diagram of CCM alloy system

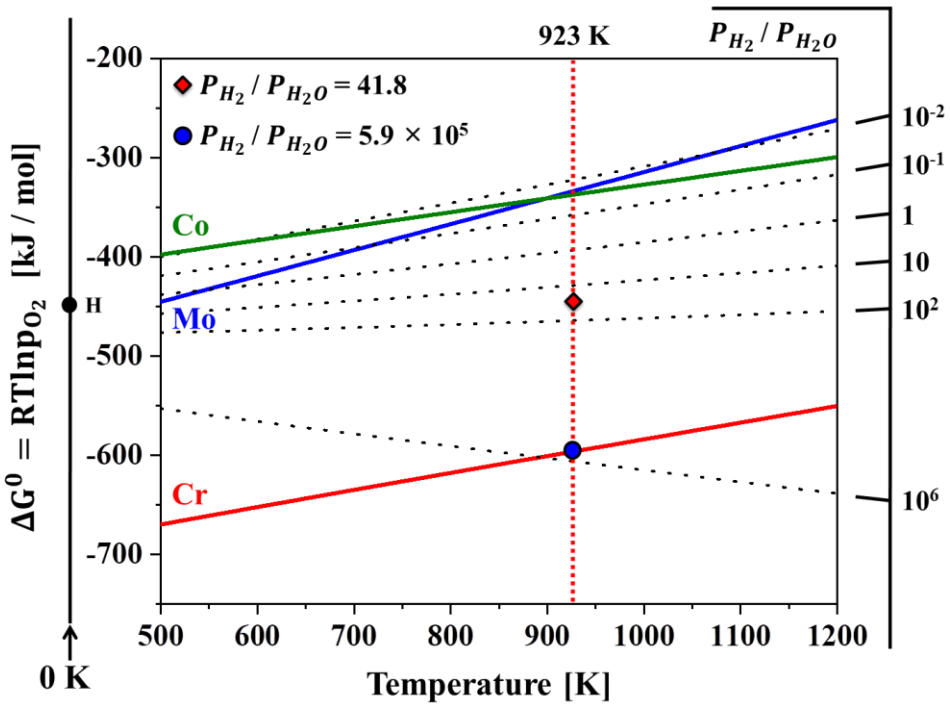

Figure 6.1. Ellingham diagram for the oxidation of Co, Cr, and Mo. The oxidation driving force according to the temperature was calculated by Thermo-Calc software using the condensed compound database of SSUB5. The $p_{H_2(g)}/p_{H_2O(g)}$ values according to temperature were represented by the dotted lines.

For the SOA, the oxidation driving force of the elements constituting the CCM alloy was calculated using Thermo-Calc software. Figure 6.1 represents the oxidation driving force of Co, Cr, and Mo. At 650 ℃, the temperature at which the heat treatment was performed in this study, Cr has the highest oxidation driving force, and Co and Mo have the similar oxidation driving force value. Because Cr has a higher oxidation driving force than other elements, it will be possible to selectively oxidize Cr by controlling the oxidation potential to form a Cr_2O_3 oxide layer on the surface. The ΔG^0 values were calculated using Thermo-Calc, and the ΔG^0 values of Co, Cr, and Mo for the oxidation at 650 ℃ were -338.2, -597.5, and -335.5 kJ/mol, respectively..

According to the thermodynamic calculation of section 2.2, the $(p_{O_2(g)})_{eq}$ values for Co, Cr, and Mo at 650 ℃ were calculated to 1.6×10^{-16}, 1.2×10^{-34}, and 3.0×10^{-15} atm, respectively. And according to the thermodynamic calculation of section 2.3, the $(p_{H_2(g)}/p_{H_2O(g)})_{eq}$ values of Co, Cr, and Mo at 650 ℃ were 4.19×10^{-1}, 5.93×10^{5}, and 5.55×10^{-1}, respectively. Therefore, if $p_{H_2(g)}/p_{H_2O(g)}$ is controlled between 4.19×10^{-1} and 5.93×10^{5} at 650 ℃, it is possible to form an atmosphere in which Cr and Mo are reduced, and only Cr is selectively oxidized. Therefore, the experiments were carried out under the condition of the $p_{H_2(g)}/p_{H_2O(g)}$ value of 41.8 because not only Cr can selectively oxide but also the thermostat' s temperature could maintain near room temperature.

6.4. Surface modification by selective oxidation

The samples' surfaces were analyzed through XPS to inspect the surface oxide layer changes by the SOA. Figure 6.2 shows the XPS results of the as-built SOA10, SOA20, and SOA30 samples. In the XPS spectrum of the as-built sample, peaks with high intensity were presented at 778.2 and 793.2 eV, corresponding to the metallic state of Co (Co^0), and peaks with low intensity were also observed at 780 and 795.2 eV, corresponding to Co^{2+} oxidation state (Co $2p_{1/2}$ and Co $2p_{3/2}$) [123]. In the Cr region, peaks attributed to the metallic state of Cr (Cr^0) were detected at 574.9 and 584.4 eV, and peaks attributed to the Cr^{3+} oxidation state (Cr $2p_{3/2}$ and Cr $2p_{1/2}$) were detected at 576.6 and 586.3 eV [124]. In the Mo region, only metallic state peaks of Mo (Mo^0) at 228.1 and 231.3 eV were presented [125]. The surface analysis result of the as-built sample showed that the metallic state peaks produced by bulk metal were stronger than the ion state peaks from the oxide. Only a native oxide film was formed on the surface in the as-built sample as no additional heat treatment was applied. Therefore, the metallic state peaks are mainly observed in the XPS spectrum due to the thinness of the native oxide layer.

In the XPS spectra of the samples after the SOA (SOA10, SOA20, and SOA30), no peaks were observed in Co and Mo regions. In the Cr region, Cr^0 peaks disappeared, and the intensity of Cr^{3+} peaks at 576.6 and 586.3 eV drastically increased. Also, a peak formed by the multiplet splitting of the Cr^{3+} ion state is observed at 575.4 eV, slightly to the left side of the Cr $2p_{3/2}$ peak (576.6 eV) [126]. These results confirmed that only Cr was selectively oxidized under the condition with the $p_{H_2(g)}/p_{H_2O(g)}$ of 41.8, as in the thermodynamic calculation results, resulting in the formation of the Cr oxide layer on the surface.

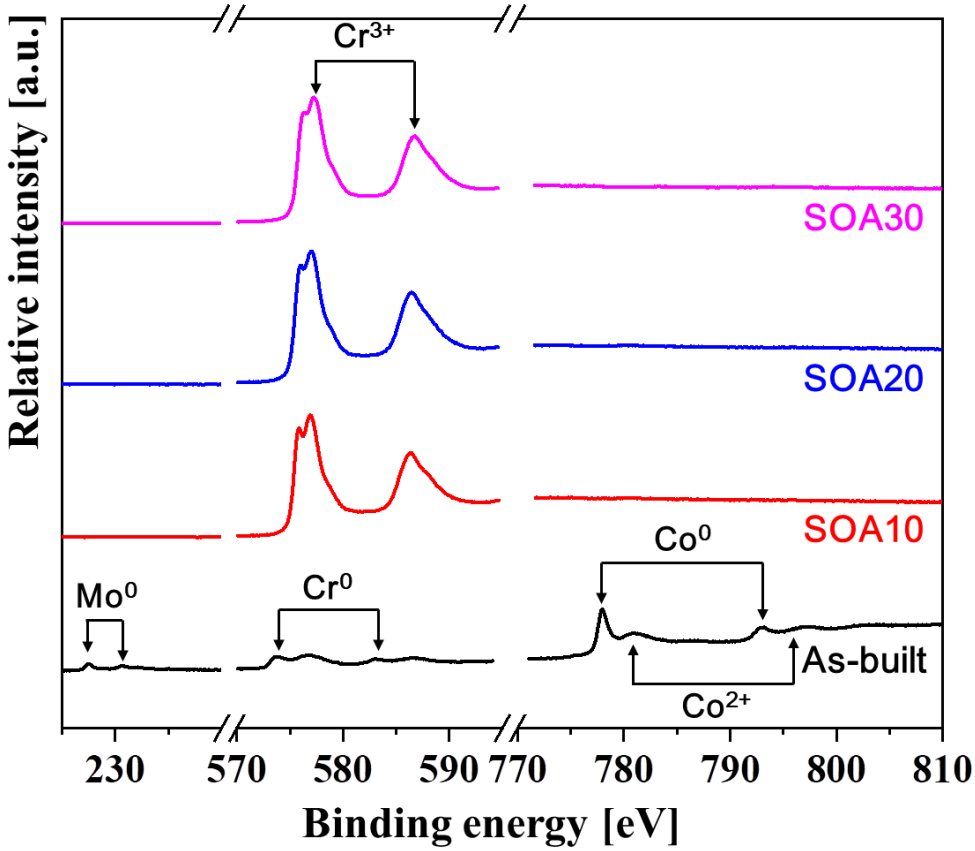

Figure 6.2. X-ray photoelectron spectroscopy (XPS) spectra of the as-built, SOA10, SOA20, and SOA30 samples.

Meanwhile, Figure 6.3 shows the morphology of the oxide layer on the samples' surfaces observed using TEM. Only a very thin native oxide film was observed on the surface of the as-built sample, which affected the formation of the metallic state peaks with high intensity in the XPS result. The surface oxide layer's thickness increased with the SOA time, and the oxide layer thicknesses of SOA10, SOA20, and SOA30 samples were 8.7, 20.3, and 39.5 nm, respectively.

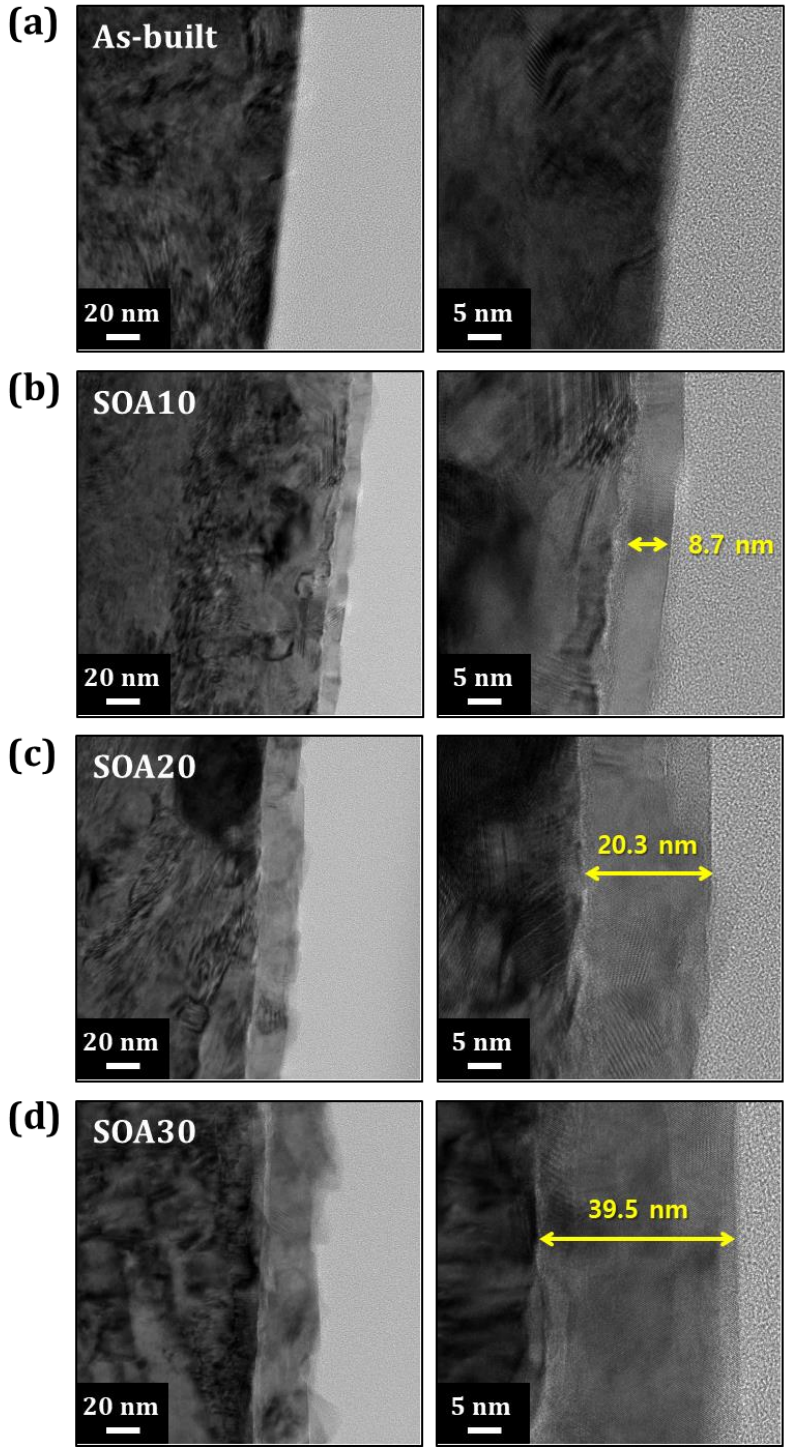

Figure 6.3. Morphology of oxide layer on the (a) as-built, (b) SOA10, (c) SOA20, and (d) SOA30 samples analyzed by TEM.

In addition, Figure 6.4 represents the composition mapping results of the samples analyzed by the TEM. The oxide layer on the as-built sample was so thin that the area with high oxygen concentration could not be observed on the surface. On the surface of the SOA10, SOA20, and SOA30 samples, oxide layers with high Cr concentrations were formed by the SOA. The compositions of the surface oxide layers of the three samples were analyzed by the EDS, and the oxide layers of the samples had a similar composition with the Cr_2O_3. These XPS and TEM results confirmed that the Cr_2O_3 oxide layer could be formed on the surface through the SOA in the CCM alloy, and a thicker oxide layer could be obtained by increasing the annealing time.

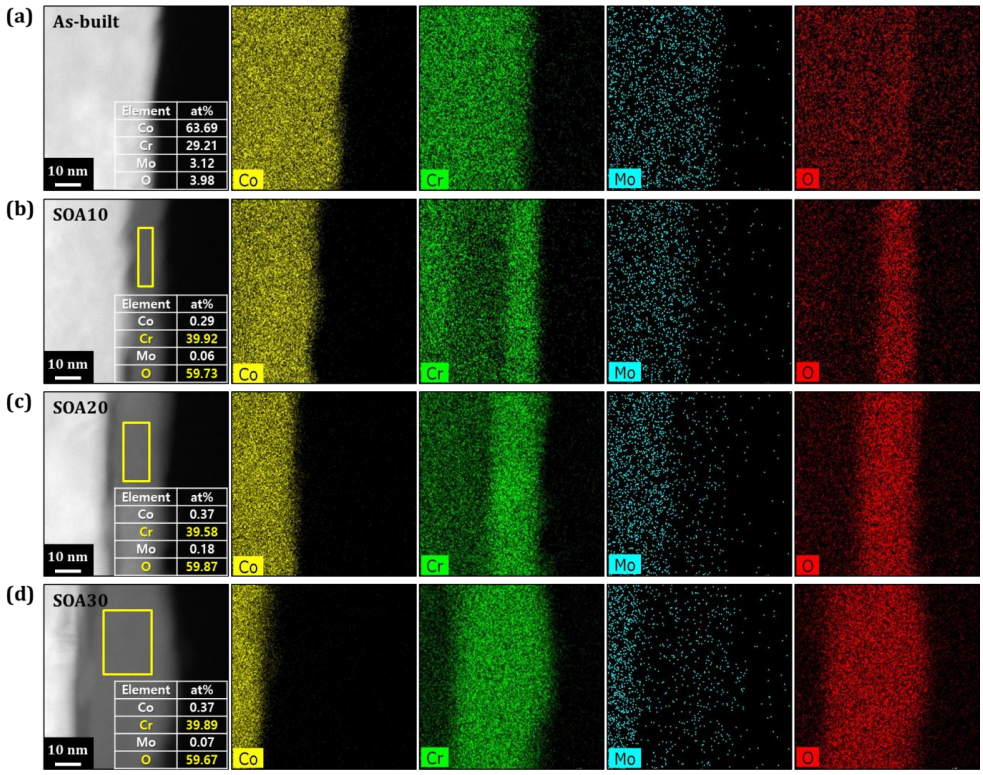

Figure 6.4. Composition mapping results of the (a) as-built, (b) SOA10, (c) SOA20, and (d) SOA30 samples analyzed by TEM. The yellow rectangles indicate the region where the composition analysis of the oxide layer was performed.

6.5. Enhancement of corrosion properties of CCM alloy: OCP & polarization curve test

Figure 6.5(a) and (b) represent OCP analysis results and polarization curves, respectively. The corrosion potential (E_{corr}) and corrosion current density (I_{corr}) derived from the polarization curves were summarized in Figure 6.6 The Cr_2O_3 oxide layer grown by the SOA altered the CCM alloy's corrosion properties. As shown in Figure 6.5(a), the OCP value shifted catholically after the SOA, but no additional shift occurred with the annealing time. The OCP fluctuation shown in the as-built sample seemed to be ascribed to the very thin Cr_2O_3 oxide layer, so the fluctuation weakened and/or disappeared after the SOA due to the thickened oxide layer. From the OCP positions, it is known that all samples were well passivated, as shown in Figure 6.5(b). However, because of the thickened oxide layer through the SOA, the corrosion current density remarkably decreased with the increase in corrosion potential. Further reduction in the corrosion current density occurred with the increase in the SOA time from 10 to 20 min. However, no additional reduction occurred when the annealing time increased from 20 to 30 min.

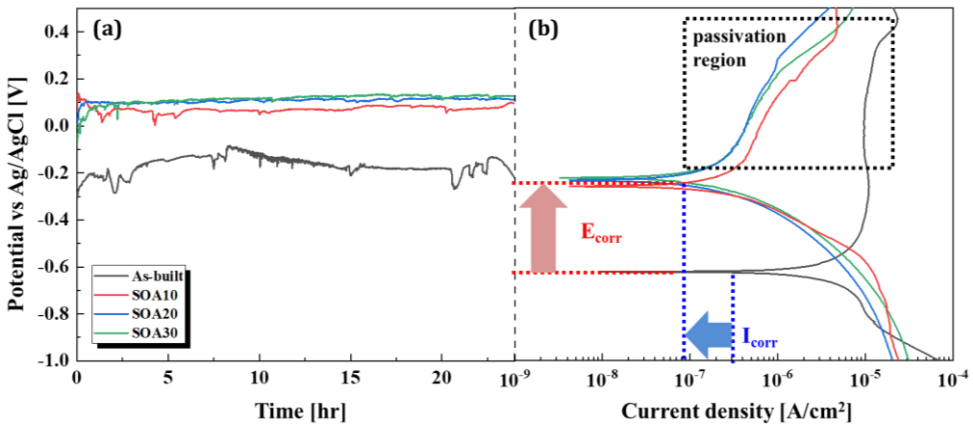

Figure 6.5.(a) OCP variations with time and (b) polarization curves of the as-built, SOA10, SOA20, and SOA30 samples in 3.5 wt% sodium chloride (NaCl) solution.

	As-built	SOA10	SOA20	SOA30
E_{corr} (V)	– 0.61	– 0.25	– 0.23	– 0.22
I_{corr} (A/cm^2)	5.34×10^{-6}	2.84×10^{-7}	1.58×10^{-7}	1.30×10^{-7}

Figure 6.6. Results of corrosion potential (E_{corr}) and corrosion current density (I_{corr}) were derived from the polarization curves of the as-built, SOA10, SOA20, and SOA30 samples

6.5.1 Enhancement of corrosion properties of CCM alloy: EIS test

The EIS results also showed similar behavior to the polarization ones. Figure 6.7 showed the evolutions of Nyquist plots with the SOA and its time, and the corresponding fitted data were listed in Figure 6.8. The equivalent circuit used to fit consisted of two resistor-capacitor (RC) cells connecting in the series, where R_{ct} and CPE_{dl} corresponded to a charge transfer resistance and double-layer capacitance at the oxide/electrolyte interface, and R_o and CPE_o were the resistance and capacitance of the oxide layer, respectively. Diameter of the semicircle denoting corrosion resistance was increased with the SOA as a result of the thickened oxide layer, but this increase stopped over the 20 min SOA. The main contribution to the increase in the corrosion resistance came from the resistance of the oxide layer (R_o), meaning that the increased oxide thickness played the main role in improving the corrosion resistance. For the oxide layer's resistance, the as-built sample had about 5×10^4 $\Omega \cdot cm^2$ and its value increased up to 1×10^6 $\Omega \cdot cm^2$ when the SOA over 20 min was applied.

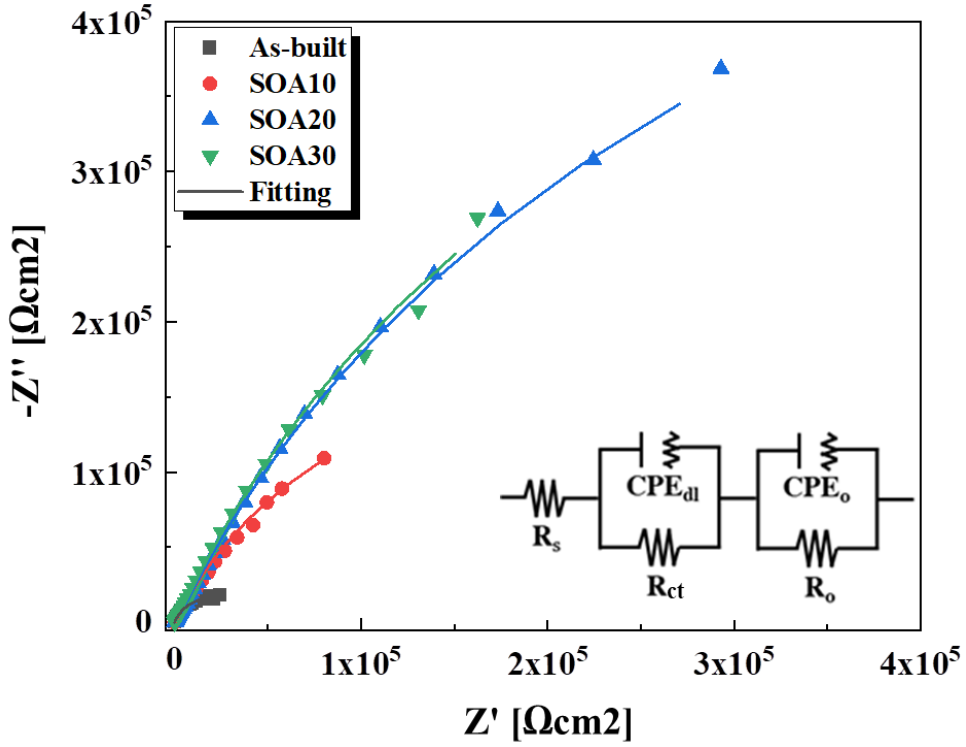

Figure 6.7. Nyquist plots of the as-built, SOA10, SOA20, and SOA30 samples were measured in 3.5 wt% sodium chloride (NaCl) solutions. The inlet is the equivalent circuit used to interpret the data.

Element	$R_s(\Omega \cdot cm^2)$	$R_0(\Omega \cdot cm^2)$	$CPE_0(F \cdot cm^{-2})$	$R_{ct}(\Omega \cdot cm^2)$	$CPE_{dl}(F \cdot cm^{-2})$
As-built	9.241	5.15×10^4	3.05×10^{-5}	1,011	9.25×10^{-5}
SOA10	9.774	4.50×10^5	1.63×10^{-5}	1,016	4.85×10^{-5}
SOA20	9.214	1.39×10^6	4.69×10^{-6}	1,021	4.58×10^{-6}
SOA30	9.415	1.32×10^6	7.81×10^{-6}	1,018	1.85×10^{-5}

Figure 6.8. Results of impedance parameters of the as-built, SOA10, SOA20, and SOA30 samples derived from the equivalent circuit analysis.

Chapter 7. Conclusions

Conclusions

The selective oxidation annealing is a method that selectively oxidizes certain elements by controlling the oxidation potential. When the oxidation driving force of the elements constituting the alloy is different, it is possible to form a dense oxide layer on the surface by selectively oxidizing specific elements. This annealing process is advantageous because it regulates the formation of an oxide layer by only modulating the oxidation potential during the annealing process. Through thermodynamic calculations, it is possible to control the selective oxidation annealing atmosphere that oxidizes only specific elements.

In this study, the selective oxidation annealing process can be implemented through the Ellingham diagram represented in terms of $p_{H_2(g)}/p_{H_2O(g)}$ rather than $p_{O_2(g)}$, and the process was performed based on Ellingham diagram. First, among the three heat treatment atmosphere conditions (air, $p_{H_2(g)}/p_{H_2O(g)}$=2.5, 41.8) with different oxidation potentials, the selective oxidation annealing was carried out to form the insulating oxide layer on the surface of the Fe-3Si-5.5Cr powders. When the powder was annealed under the condition where the $p_{H_2(g)}/p_{H_2O(g)}$=41.8, in which Fe is reduced and only Si and Cr are selectively oxidized, the Cr and Si complex oxide layer was formed on the powder surface. The withstanding voltage of the initial powder was improved after the selective oxidation annealing. The magnetic property of the powder applying the selective

oxidation annealing was also improved compared to initial powder and it was proved by VSM analysis.

Previously, it was confirmed that the selective oxidation annealing was successfully performed at the $p_{H_2(g)}/p_{H_2O(g)}$=41.8 condition and the surface was modified, so an experiment was conducted on the behavior of the oxide layer formation on the surface of the powder with respect to selective oxidation heat treatment time. As the selective oxidation annealing time increased, it was confirmed that a uniform and dense insulating layer was formed on the surface of the powder.

Powder metallurgy process was applied to powder formed with an oxide layer through selective oxidation annealing technology and a commonly used wet chemical process to form a phosphate and SiO_2 insulating layer, and SMC core was manufactured and insulation and magnetic properties were analyzed. Through EPMA analysis results and withstanding voltage analysis, it was confirmed that the insulation properties of the core fabricated by selectively oxidized powder were improved, and the magnetic properties were also improved by converting the permeability (μ') from the inductance (L).

In addition, the hysteresis loss (Wh) and the eddy current loss (We) were calculated from the core loss data through a variable separation method, and it was confirmed that both losses decreased as the selective oxidation heat treatment time increased. This is because, respectively, the area of the hysteresis curve decreased and the effective particle size of the powder decreased due to the formation of a dense insulating layer.

In consideration of the actual operating environment of the SMC core, high-temperature load evaluation and corrosion

characteristics were evaluated. It was confirmed that there was no deterioration in the quality factor in the core as it was manufactured as a powder that had undergone selective oxidation annealing. It was confirmed that the corrosion properties improved as the selective oxidation heat treatment time increased through the polarization curve and EIS test.

As mentioned above, selective oxidation annealing is a general-purpose heat treatment technology that uses different oxidation potential of the elements constituting the alloy, so the alloy surface was modified by applying selective oxidation annealing to the CoCrMo alloy, which is a representative composition of the bio-alloy system,

Bibliography

[1] H. Shokrollahi, K. Janghorban, J. Mater. Process. Tech. 189 (2007) 1.

[2] H. A. Im, J. Y. Jeong, S. B. An, K. Y. Sohn, W. W. Park, Korean J. Met. Mater. 58 (2020) 633.

[3] D. S. Shin, J. W. Oh, I. D. Jung, H. J. Kim, M. W. Lee, G. W. Noh, W. S. Yang, S. J. Park, Met. Mater. Int. 26 (2020) 94.

[4] Y. Yoshizawa, Scr. Mater. 44 (2001) 1321.

[5] S. F. Chen, H. Y. Chang, S. J. Wang, S. H. Chen, C. C. Chen, J. Alloy. Compd. 637 (2015) 30.

[6] H. K. Park, M. S. Han, C. H. Chang, J. T. Park, C. S. Park, H. D. Joo, Met. Mater. Int. 26 (2020) 321.

[7] S. Mori, T. Mitsuoka, K. Sugimura, R. Hirayama, M. Sonehara, T. Sato, N. Matsushita, Adv. Powder Technol. 29 (2018) 1481.

[8] C. Ragusa, H. Zhao, C. Appino, M. Khan, O. de la Barriere, F. Fiorillo, IEEE Magn. Lett. 7 (2016) 5106105.

[9] H. K. Park, J. H. Kang, C. S. Park, C. H. Han, N. M. Hwang, Mater. Sci. Eng. A. 528 (2011) 3228.

[10] H. Han, D. Pan, D. Li, Mater. Res. Express. 6 (2019) 026104.

[11] H. I. Hsiang, L. F. Fan, K. T. Ho, IEEE Trans. Magn. 54 (2018) 1.

[12] H. Fujimori, H. Yoshimoto, T. Masumoto, J. Appl. Phys. 52 (1981) 1893.

[13] T. Saito, H. Tsuruta, A. Watanabe, T. Ishimine, T. Ueno, AIP Adv. 8 (2018) 047708.

[14] M. Yaghtin, A. H. Taghvaei, B. Hashemi, K. Janghorban, J. Alloy. Compd. 581 (2013) 293.

[15] J. Wang, X. Liu, C. Lei, X. Mao, D. Liu, Z. Luo, F. Luo, J. Magn. Magn. Mater. 502 (2020) 166553.

[16] K. D. Choi, S. H. Kim, P. W. Jang, W. Y. Yoon, J. Y. Byun, J. Alloy. Compd. 854 (2021) 157241.

[17] M. Anhalt, J. Magn. Magn. Mater. 320 (2008) e366.

[18] Y. Yang, Y. Wang, S. Wu, C. Liu, L. Chen, AIP Adv. 11 (2021) 015140.

[19] W. Li, W. Wang, J. Lv, Y. Ying, J. Zheng, L. Qiao, S. Che, J. Magn. Magn. Mater. 456 (2018) 333.

[20] X. Wu, C. Chen, J. Hao, T. Zhao, H. Ma, Y. Lu, Z. Ren, J. Supercond. Novel Magn. 33 (2020) 1889.

[21] D. Xie, K. Lin, S. Lin, J. Magn. Magn. Mater. 353 (2014) 34.

[22] L. S. Karenina, G. S. Korzunin, R. B. Puzhevich, Phys. Met. Metallogr (2011) 111 21.

[23] H. Hsiang, S. Wang, C. Chen, J. Magn. Magn. Mater. 514 (2020) 167151.

[24] K. Kim, T. Kang, B. Koo, J. Vac. Sci. Technol. A. 19 (2001) 998.

[25] K. Yanagihara, S. Yamazaki, Oxid. Met. 57 (2002) 281.

[26] S. K. Lee, J. S. Kim, J. W. Choi, N. Kang, K. M. Cho, Met. Mater. Int. 17 (2011) 251.

[27] M. Pourmajidian, J. R. McDermid, Metall. Mater. Trans. A 49 (2018) 1795.

[28] E. Essuman, G. H. Meier, J. Zurek, M. Hansel, W. J. Quadakkers, Oxid. Met. 69 (2008) 143.

[29] J. K. Choe, D. H. Kim, B. L. Jo, S. H. Hong, J. Y. Park, S. J. Park, Korean J. Met. Mater. 58 (2020) 125.

[30] H. I. Hsiang, L. F. Fan, K. T. Ho, IEEE Trans. Magn. 54 (2018) 2000407.

[31] S. Mori, T. Mitsuoka, M. Sonehara, T. Sato, N. Matsushita, AIP Adv. 7 (2017) 056657.

[32] J. Y. Park, K. Park, J. W. Kang, H. G. Kim, N. M. Hwang, H. K. Park, Mater. Today Commun. 25 (2020) 101488.

[33] G. Zhao, C. Wu, M. Yan, J. Alloy. Compd. 710 (2017) 138.

[34] P. Ghods, O. B. Isgor, J. R. Brown, F. Bensebaa, D. Kingston, Appl. Surf. Sci. 257 (2011) 4669.

[35] T. V. Larina, L. S. Dovlitova, V. V. Kaichev, V. V. Malakhov, T. S. Glazneva, E. A. Paukshtis, B. S. Bal'zhinimaev, RSC Adv. 5 (2015) 79898.

[36] H. M. Yadav, T. V. Kolekar, A. S. Barge, N. D. Thorat, S. D. Delekar, B. M. Kim, B. J. Kim, J. S. Kim, J. Mater. Sci.−Mater. Electron. 27 (2016) 526.

[37] F. Magalhaes, M. C. Pereira, S. E. C. Botrel, J. D. Fabris, W. A. Macedo, R. Mendonça, R. M. Lago, L. C. A. Oliveira, Appl. Catal. AGen. 332 (2007) 115.

[38] A. R. Pratt, N. S. McIntyre, Surf. Interface Anal. 24 (1996) 529.

[39] A. M. Huntz, V. Bague, G. Beaupl´e, C. Haut, C. S´ev´erac, P. Lecour, X. Longaygue, F. Ropital, Appl. Surf. Sci. 207 (2003) 255.

[40] M. Hao, B. Sun, H. Wang, Materials, Materials. 13 (2020) 509.

[41] G. H. Meier, K. Jung, N. Mu, N. M. Yanar, F. S. Pettit, J. Piron Abellan, T. Olszewski, L. N. Hierro, W. J. Quadakkers, G. R. Holcomb, Oxid. Met. 74 (2010) 319.

[42] S. Swaminathan, M. Spiegel, Appl. Surf. Sci. 253 (2007) 4607.

[43] M. Auinger, E. -M. Müller-Lorenz, M. Rohwerder, Corrosion Sci. 90 (2015) 503.

[44] S. Mori, T. Mitsuoka, M. Sonehara, T. Sato, N. Matsushita, AIP Adv. 7 (2017) 056657.

[45] T. S. N. Sankara Narayanan, Rev. Adv. Mater. Sci. 9 (2005) 130.

[46] J. Y. Park, K. Park, B. Seo, J. O. Fadonougbo, T. W. Na, K. B. Park, H. T. Im, N. M. Hwang, H. K. Park, Met. Mater. -Int. 28 (7) (2022) 1778.

[47] H. I. Hsiang, L. F. Fan, K. T. Ho, J. Magn. Magn. Mater. 444 (2017) 1.

[48] Y. J. Choi, J. H. Ahn, S. W. Kim, Y. R. Kim, B. W. Lee, MRS Commun. 11 (2021) 457.

[49] J. Wang, S. Song, H. Sun, G. Hang, Z. Xue, C. Wang, W. Chen, D. Chen, J. Magn. Magn. Mater. 519 (2021) 167496.

[50] N. J. Tang, W. Zhong, X. L. Wu, H. Y. Jiang, W. Liu, Y. W. Du, Mater. Lett. 59 (2005) 1723.

[51] Z. H. Khan, M. M. Rahman, S. S. Sikder, M. A. Hakim, D. K. Saha, J. Alloy. Compd. 548 (2013) 208.

[52] S. Wu, A. Sun, W. Xu, Q. Zhang, F. Zhai, P. Logan, A. Volinsky, J. Magn. Magn. Mater. 324 (2012) 3899.

[53] A. H. Taghvaei, H. Shokrollahi, K. Janghorban, J. Magn. Magn. Mater.

321 (2009) 3926.

[54] B. Zhou, Y. Dong, L. Liu, L. Chang, F. Bi, X. Wang, J. Magn. Magn. Mater. 474 (2019) 1.

[55] T. Saito, S. Takemoto, Journal of the Magnetics Society of Japan, (2013) 1302R012.

[56] R. Parsons, B. Zang, K. Onodera, H. Kishimoto, T. Shoji, A. Kato, K. Suzuki, J. Magn. Magn. Mater. 476 (2019) 142.

[57] J. Wang, Q. Ren, Y. Luo, L. Zhang, J. Magn. Magn. Mater. 451 (2018) 454.

[58] Y. Ushigami, M. Mizokami, M. Fujikura, T. Kubota, H. Fujii, K. Murakami, J. Magn. Magn. Mater. 254 (2003) 307.

[59] G. Bertotti, F. Fiorillo, G. P. Soardo, IEEE Trans. On Mag. 12 (1988) 621.

[60] K. J. Overshoot, IEEE Trans. On Mag. 12 (1976) 840.

[61] M. Gong, Y. Dong, J. Huang, L. Chang, Y. Pan, F. Wang, A. He, J. Li, X. Liu, X. Wang, J. Mater. Sci.-Mater. Electron. 32 (2021) 8829.

[62] H. I. Hsiang, C. H. Chen, C. C Chen, J. Mater. Sci.-Mater. Electron. 32 (2021) 14584.

[63] A. H. Taghvaei, H. Shokrollahi, K. Janghorban, H. Abiri, Mater. Des. 30 (2009) 3989.

[64] B. Li, T. Zhang, C. Jiang, J. Gu, J. Magn. Magn. Mater. 508 (2020) 166869.

[65] Y. Wu, M. Han, Z. Tang, L. Deng, J. Appl. Phys. 115 (2014) 163902.

[66] J. Huang, L. Jiao, Y. Yang, Y. Dong, Y. Zhang, L. Chang, M. Gong, J. Li,

A. He, X. Wang, metals 10 (2020) 1699.

[67] T. Saito, H. Tsuruta, A. Watanabe, T. Ishimine, T. Ueno, AIP Adv. 8 (2017) 047708.

[68] H. I. Hsiang, J. Mater, Sci. Mater. Electron. 31 (2020) 16089.

[69] 3 L. Svensson, K. Frogner, P. Jeppsson, T. Cedell, M. Andersson, J. Magn. Magn. Mater. 324 (2012) 2717.

[70] H. Yu, S. Zhou, G. Zhang, B. Dong, L. Meng, Z. Li, Y. Dong, X. Cao, J. Magn. Magn. Mater. 552 (2022) 168741.

[71] M. Li, X. Chen, J. Guan, X. Wang, J. Wang, C. T. Williams, C. Liang, J. Mater. Chem. 22 (2012) 609.

[72] F. Shao, K. Yang, H. Zhao, C. Liu, L. Wang, S. Tao, Surf. Coat. Technol. 276 (2015) 8.

[73] H. Y. Jiang, W. Zhong, X. L. Wu, N. J. Tang, W. Liu, Y. W. Du, J. Alloys Compd. 384 (2004) 264.

[74] R. W. Kuehl, Microelectron. Reliab. 54 (2014) 1316.

[75] A. E. Council, Tech. Rep. AEC-Q101-Rev-D1 (2013).

[76] A. M. Huntz, V. Bague, G. Beauplé, C. Haut, C. Sévérac, P. Lecour, X. Longaygue, F. Ropital, Appl. Surf. Sci. 207 (2003) 255.

[77] M. Hao, B. Sun, H. Wang, Materials 13 (2020) 509.

[78] M. Auinger, E. -M. Müller-Lorenz, M. Rohwerder, Corros. Sci. 90 (2015) 503.

[79] G. H. Meier, K. Jung, N. Mu, N. M. Yanar, F. S. Pettit, J. Pirón Abellán, T. Olszewski, L. N. Hierro, W. J. Quadakkers, G. R. Holcomb, Oxid. Met. 74 (2010) 319.

[80] P. Ghods, O. B. Isgor, J. R. Brown, F. Bensebaa, D. Kingston, Appl. Surf. Sci. 2011, 257, 4669.

[81] G. Zhao, C. Wu, M. Yan, J. Alloys Compd. 2017, 710, 138.

[82] T. V. Larina, L. S. Dovlitova, V. V. Kaichev, V. V. Malakhov, T. S. Glazneva, E. A. Paukshtis, B. S. Bal'zhinimaev, RSC Adv. 2015, 5, 79898.

[83] H. M. Yadav, T. V. Kolekar, A. S. Barge, N. D. Thorat, S. D. Delekar, B. M. Kim, B. J. Kim, J. S. Kim, J. Mater, Sci. Mater. Electron. 2016, 27, 526.

[84] C. M. Chang, C. C. Hsieh, C. M. Lin, J. H. Chen, C. M. Fan, W. Wu, Mater. Chem. Phys. 123 (2010) 241.

[85] S. Ningshen, M. Sakairi, K. Suzuki, S. Ukai, Corrosion 69 (2013) 863.

[86] S. Jiang, F. Chai, H. Su, C. Yang, Corros. Sci. 123 (2017) 217.

[87] J. O. Iroh, W. Su, Electrochim. Acta 46 (2000) 15.

[88] Z. Mirzakhanzadeh, A. Kosari, M. H. Moayed, R. Naderi, P. Taheri, J. M. C. Mol, Corros. Sci. 138 (2018) 372.

[89] L. Jianguo, G. Gaoping, Y. Chuanwei, Electrochim. Acta 50 (2005) 3320.

[90] H. Zhang, Y. L. Zhao, Z. D. Jiang, Mater. Lett. 59 (2005) 3370.

[91] Z. B. Wang, H. X. Hu, C. B. Liu, Y. G. Zheng, Electrochim. Acta 135 (2014) 526.

[92] F. Mansfeld, Electrochim. Acta 35 (1990) 1533.

[93] P. L. Bonora, F. Deflorian, L. Fedrizzi, Electrochim. Acta 41 (1996) 1073.

[94] L. Pezzato, R. Babbolin, P. Cerchier, M. Marigo, P. Dolcet, M. Dabalà,

K. Brunelli, Corros. Sci. 173 (2020) 108741.

[95] C. Ding, Y. Tai, D. Wang, L. Tan, J. Fu, Chem. Eng. J. 357 (2019) 518.

[96] T. Zhang, W. Liu, L. Chen, B. Dong, W. Yang, Y. Fan, Y. Zhao, Corros. Sci. 192 (2021) 109851.

[97] H. T. Im, H. S. Kang, H. G. Kang, H. Y. Kim, J. Choi, K. B. Park, T. W. Lee, C. B. Mo, H. K. Park, Rapid Prototyping J. 28 (2022) 404.

[98] X. P. Tan, P. Wang, Y. Kok, W. Q. Toh, Z. Sun, S. M. L. Nai, M.Descoins, D. Mangelinck, E. Liu, S. B. Tor, Scr. Mater. 143 (2018) 117.

[99] A. Takaichi, Y. Kajima, N, Kittikundecha, H. L. Htat, H. H. W. Cho, T. Hanawa, T. Yoneyama, N. Wakabayashi, J Mech. Behav. Biomed. Mater. 102 (2020) 103496.

[100] B. Qiana, K. Saeidi, L. Kvetková, F. Lofaj, C. Xiao, Z. Shen. Aginagalde, Dent. Mater. 31 (2015) 1435.

[101] S. H. Sun, Y. Koizumi, S. Kurosu, Y. P. Li, H. Matsumoto, A. Chiba, Acta Mater. 64 (2014) 154.

[102] J. H. Hong, F. Y. Yeoh, Mater. Today: Proc. 29 (2020) 196.

[103] X. Z. Xin, N. Xiang, J. Chen, B. Wei, Mater. Lett. 88 (2012) 101.

[104] T. Aldhohrah, J. Yang, J. Guo, H. Zhang, Y. Wang, J. Prosthet. Dent. 13 (2021).

[105] H. T. Im, D. H. Kim, Y. D. Kim, J. O. Fadonougbo, C. B. Mo, J. Y. Park, K. B. Park, J. W. Kang, H. S. Kang, H. K. Park, Mater. Charact. 186 (2022) 111767.

[106] L. H. M. Antunes, J. J. Hoyos, E. B. Fonseca, M. Béreš, P. F. da Silva Farina, E. S. N. Lopes, A. L. Jardini, R. Maciel Filho, Mater. Sci. & Eng. A

764 (2019) 138262.

[107] S. H. Sun, Y. Koizumi, S. Kurosu, Y. P. Li, A. Chiba, Acta. Mater. 86 (2015) 305.

[108] T. W. Na, W. R. Kim, S. M. Yang, O. h. Kwon, J. M. Park, G. H. Kim, K. H. Jung, C. W. Lee, H. K. Park, H. G. Kim, Mater. Charact. 143 (2018) 110.

[109] W. H. Lee, T. W. Na, K. W. Yi, S. M. Yang, J. W. Kang, H. G. Kim, H. K. Park, Rapid Prototyp. J. 26 (2020) 1401.

[110] H. K. Park, Y. K. Ahn, B. S. Lee, K. H. Jung, C. W. Lee, H. G. Kim, Mater. Lett. 187 (2017) 98.

[111] H. K. Park, T. W. Na, S. M. Yang, G. H. Kim, B. S. Lee, H. G. Kim, Mater. Lett. 236 (2019) 106.

[112] D. Wei, A. Anniyaer, Y. Koizumi, K. Aoyagi, M. Nagasako, H. Kato, A. Chiba, Addit. Manuf. 28 (2019) 215.

[113] Y. Liu, Y. Yang, D. Wang, Int. J. Adv. Manuf. Technol. 87 (2016) 647.

[114] Y. Lu, S. Wu, Y. Gan, T. Huang, C. Yang, L. Junjie, J. Lin, Opt. Laser. Technol. 75 (2015) 197.

[115] C. Cai, X. Wu, W. Liu, W. Zhu, H. Chen, J. C. D. Qiu, C.N. Sun, J. Liu, Q. Wei, Y. Shi, J. Mater. Sci. Technol. 57 (2020) 51.

[116] S. Sun, Q. Teng, Y. Xie, T. Liu, R. Ma, J. Bai, C. Cai, Q. Wei, Addit. Manuf. 46 (2021) 102168.

[117] X. Xin, J. Chen, N. Xiang, B. Wei, Cell Biochem. Biophys. 67 (2013) 983.

[118] Y. Kajima, A. Takaichi, N. Kittikundecha, H. L. Htat, H. H. W. Cho, Y. Tsutsumi, T. Hanawa, N. Wakabayashi, T. Yoneyam, Dent. Mater. 37 (2021) e98.

[119] B. S. Seo, H. K. Park, H. G. Kim, W. R. Kim, K. S. Park, Surf. Coat. Technol. 406 (2021) 126640.

[120] J. Y. Park, K. S. Park, J. O. Fadonougbo, K. R. Jang, S. D. Park, C. S. Park, C. B. Mo, N. M. Hwang, H. K. Park, J. Magn. Magn. Mater. 561 (2022) 169697.

[121] J. Y. Park, N. M. Hwang, B. S. Seo, H. T. Im, K. B. Park, C. S. Park, C. B. Mo, H. K. Park, K. S. Park, Steel Res. Int. (2022) 2200236.

[122] T. J. Fleming, A. Kavanagh, G. Duggan, J. Mater. Res. Technol. 9 (2020) 9479.

[123] E. A. A. Aboelazm, G. A. M. Ali, K. F. Chong, Chem. Adv. Mater. 3 (2018) 67.

[124] Z. Wang, L, Xi, Y. Yang, Y. Li, X. Han, Y. Zuo, J. Wang, Nano−Micro Lett. 6 (4) (2014) 365.

[125] E. Vernickaitė, M. Lelis, N. Tsyntsaru, V. Pakštas, H. Cesiulis, Chemija 31 (2020) 203.

[126] B. P. Payne, M. C. Biesinger, N. S. McIntyre, J. Electron Spectrosc. Relat. Phenom. 184 (2011) 29.

국문 초록

선택적 산화 열처리 기술을 바탕으로 접근한 합금의 표면 산화층 개질에 대한 연구

Fe-Si-Cr 계는 에너지 변환장치인 인덕터 코어에 주로 사용되는 합금계이며 복잡한 형상제조와 등방의 자기적 특성을 가지는 장점이 있는 분말을 사용하여 분말 야금 공정을 통해 인덕터 코어로 제조하게된다. 코어의 사용환경과 에너지 저장량을 고려할 때, 분말간의 절연층을 치밀하고 균일하게 형성하는 것이 필수적이다. 하지만 기존의 인덕터 코어 제조 공정에서 절연층을 형성하는 방식은 습식공정을 적용하여 주로 제조되었다. 따라서 분말 표면에 불균일한 절연층이 형성되게 되고 이에 따라 자성특성 및 절연특성의 저하가 지속적으로 발생하는 문제가 발생하고 있는 상황이다. 따라서 기상 방식으로 선택적으로 절연특성이 우수한 원소만을 산화시키게 된다면 분말 표면에 치밀하고 우수한 절연특성을 가지는 절연층을 형성할 수 있게 된다. 이러한 열처리 기술을 선택적 산화 열처리 기술이라고 한다.

선택적 산화 열처리 기술은 합금을 구성하는 원소의 산화 구동력이 다름을 이용하여 열처리 시 산화포텐셜을 제어하여 특정 원소만을 산화시키는 것을 가능하게 하는 열처리 기술이다. 본 연구에서 산화 환원 반응에서의 열역학계산을 통해 선택적 산화 열처리 공정을 설계하였다. 그리고 이를 Fe-Si-Cr 연자성 분말 합금계와 Co-Cr-Mo 생체 합금계에 적용하여 합금 표면의 산화층을 개질하고 자성 및 부식 특성을 향상시켰다.

우선 Fe-Si-Cr 분말에 다양한 산화포텐셜을 가지는 분위기로 열처리를 실시하여 $p_{H_2(g)}/p_{H_2O(g)}$=41.8 조건에서 Si 과 Cr 위주의 산화층으로 개질 되는 것을 확인하였다. 분말의 자성특성과 절연특성을 측정한

결과 자성특성이 초기 분말보다 $p_{H_2(g)}/p_{H_2O(g)}$=41.8 조건에서 향상되었음을 확인하였고 내전압 시험을 통해 절연특성을 분석한 결과 초기분말과 비교했을 때 2배 이상 향상된 값을 가지는 것을 확인하였다.

분말 단위에서 열역학 계산을 통해 설계한 선택적 산화 열처리 공정을 적용하게 되면 분말 표면이 선택적으로 Si 과 Cr 만을 산화시키는 조건임을 확인하였으므로 선택적 산화 열처리 시간을 증가시켜 산화층 형성 거동을 확인하는 실험을 진행하였다. 그리고 이에 더해 실제로 분말 야금 공정을 적용하여 연자성 분말 디스크 및 토로이드 코어를 제조하여 자성 및 절연 특성을 부품단위 수준에서 진행하였다. 선택적 산화 열처리를 거친 분말로 제조된 코어는 기존의 습식공정을 적용해 제조된 코어와 내전압 시험 및 인덕턴스 측정 시험을 통해 비교 분석하였다. 코어의 품질을 종합적으로 평가하는 품질계수 값이 기존의 습식공정으로 제조된 인덕터 코어보다 선택적 산화 열처리를 적용한 분말로 제조된 코어에서 약 16% 향상되었음을 확인할 수 있었다.

그리고 실제 인덕터의 사용 환경을 고려하여 고온 부하를 1000시간 동안 부여하는 고온 부하 특성 시험과 부식 특성을 알아 보기 위해 추가적으로 전기화학 실험을 진행하였다. 균일하고 치밀한 절연층이 형성되어 있기 때문에 고온 부하 특성 실험 후에도 품질 계수가 선택적 산화 열처리를 적용하여 제조된 코어에서 감소하지 않는 것을 확인할 수 있었다.

전기화학 실험 결과 선택적 산화 열처리를 통해 Fe-Si-Cr 합금 표면에 형성된 절연층이 부식 저항성을 가지게 되는 것을 확인할 수 있었다. 절연층 내부엔 SiO_2 가 형성되었고 절연층 외부엔 Cr_2O_3 절연층이 형성되어 있었음을 XPS 분석과 TEM 분석을 통해 확인하였으며 선택적 산화 열처리 시간이 증가할수록 절연층의 두께가 증가하는 경향을 나타내었다. 선택적 산화 열처리에 의해 형성된 절연층은 분극 실험 결과 부식전위의 향상을 야기시키는 것을 확인하였으며 이를 통해 부식특성이 향상되었다고 미루어 볼 수 있었다. 여기에 더해 3.5wt% NaCl 용액에서의 EIS 실험을 통해 선택적 산화 열처리 시간이 증가함에 따라 임피던스 반원이 크게 측정되었고 절연층 파괴시간이 지연되는 것을 확인할

수 있었는데 이를 통해 선택적 산화 열처리 시간이 증가할수록 부식특성이 향상되는 것을 확인하였다.

Co-Cr-Mo 생체 합금계에서도 신체 내부에 삽입되었을 때 Co 이온이 용출되는 것을 막기 위해 부식특성 향상이 필수적인데 열처리 시 $p_{H_2(g)}/p_{H_2O(g)}$=41.8 조건에서 Co 와 Mo 는 산화시키지 않고 부식특성이 우수한 Cr 원소만을 선택적으로 산화시키는 조건임을 확인하였다. 그리고 앞서 수행한 전기화학 실험 결과 부식특성이 향상되는 것을 확인할 수 있었다.

이처럼 선택적 산화 열처리 기술은 다양한 합금계에 적용 가능하며 기상방식으로 절연층을 형성하기 때문에 크기가 작은 분말에도 적용이 가능할 것으로 예상되는 차세대 절연 기술이다.

감사의 글

흘러흘러 학위논문의 가장 마지막, 감사의 글을 쓰게 되었습니다. 학위를 진행하면서 늘 계획하고 생각하며 살았지만 늘 생각치 못한 부분이 생기기 마련이었고 기대 이상보다 기대 이하였던 적이 많았습니다. 하지만 그럴 때마다 따뜻하게, 때론 따끔하게 충고해주신 주위의 많은 사람들이 있었기에 부족한 생각을 고쳐 조금이라도 더 움직이려고 노력할 수 있었던 원동력이 되었던 것 같습니다. 저에게 가장 중요한 시기에 옆에 계셔주셨던 분들께 약소하게나마 감사의 글을 드립니다.

우선, 부족한 저를 지도해주시고 가장 많은 노력을 쏟아주신 박형기 박사님께 감사의 말씀을 먼저 드립니다. 기대에 많이 못미칠 때도 많았지만 그럴수록 진심으로 조언해주시고 행동해주신 덕분에 무사히 졸업절차를 끝낼 수 있었던 것 같습니다. 그리고 늘 진심으로 마음 써주시고 귀기울여주신 강장원 박사님께도 정말 감사하다는 말씀 드리고 싶습니다. 그리고 늘 모르는 부분에 대해서 조언 아끼지 않고 도와주신 박광석, 박창수, 나태욱 박사님께도 정말 감사의 말씀을 드립니다. 학위를 진행하며 같이 동고동락했던 현태형, 그리고 친구이자 룸메이트인 기범이가 옆에 있어서 힘들때나 기쁠때나 슬플때나 웃을 수 있었습니다. 많이 부족하지만 잘 따라주었던 규병, 종인, 홍기 다혜 륜호한테도 고맙다는 말, 이 자리를 빌어 모두 전합니다. 아무 연고도 없었던 강릉이란 곳에서, 인생에서 가장 중요한 시기에 가장 소중한 인연들을 만나 졸업의 결실을 맺을 수 있었던 것은 정말 제 인생에서 큰 행운이라고 생각합니다.

그리고 학교에서 도움주시고 지도해주신 황농문 교수님을 비롯한 TFML 실험실 분들께도 감사를 드립니다. 먼저 사회에 진출하셔서 많은 도움을 주셨던 선배님들, 끝까지 같이 고생하면서 학위 마무리하는 찬규 선미 민교 용권이 성천이에게도 고맙다는 말 전합니다.

마지막으로 언제나 걱정해주시고 무한한 사랑으로 보살펴주신 나의 가족, 인자하신 아버지, 지혜로우신 어머니, 힘이 되어준 동생 지영이에게도 늘 말해도 모자란 감사와 사랑한다는 말씀 전합니다.

그리고 기도해주시고 응원해주신 모든 분들께도 감사의 말씀을 전합니다.

이렇게 많은 사람들의 응원과 도움을 받으며 부족한 제가 학위를 진행했단 사실에 다시 한번 모두에게 진심으로 고개숙여 감사의 말씀을 올립니다. 이제 학생 신분에서 벗어나 사회에 나가 책임을 져야 합니다. 아직 막연하지만 그럴 때마다 저에게 도움을 주셨던 분들의 말씀과 충고를 등대삼아 멋지게 헤쳐나가도록 하겠습니다. 모두 감사하고 사랑합니다.

2022년 12월 22일,

눈이 희끗희끗 몰아치는 새벽,

조용한 사무실에서,

모두에게 감사하며 글을 마무리합니다.